Wet Bioadhesion in Tree Frogs

Dissertation

zur Erlangung des Grades
"Doktor der Naturwissenschaften"
im Promotionsfach Physik

Fachbereich Physik, Mathematik und Informatik
der Johannes Gutenberg-Universität
in Mainz

Farzaneh Kaveh
geboren in Teheran, Iran

Mainz, September 2014

Die vorliegende Arbeit wurde in der Zeit von 2011 bis 2014 unter der Betreuung von [In der elektronischen Fassung aus Datenschutzgründen entfernt] und [In der elektronischen Fassung aus Datenschutzgründen entfernt] am Max-Planck-Institut für Polymerforschung in Mainz angefertigt.

Tag der mündlichen Prüfung: 18. 09. 2014
1. Berichterstatter: [In der elektronischen Fassung aus Datenschutzgründen entfernt]
2. Berichterstatter: [In der elektronischen Fassung aus Datenschutzgründen entfernt]
Dissertation an der Universität Mainz (D77)

"I was born not knowing and have had only a little time to change that here and there."

Richard P. Feynman

Zusammenfassung

Viele Tiere wie etwa Geckos oder Laubfrösche können mittels ihrer Haftscheiben an Oberflächen kleben. Diese Haftscheiben ermöglichen es den Tieren, sich während ihrer Fortbewegung an Oberflächen anzuheften und wieder zu lösen unabhängig von den vorherrschenden Umweltbedingungen. Frösche besitzen mikro- und nanostrukturierte sowie charakteristisch geformte Haftscheiben an Finger- und Zehenenden. Ihre besondere evolutionäre Errungenschaft, sich stark und zugleich reversibel in sowohl trockenen als auch feuchten Umgebungen anzuhaften, hat die Wissenschaft zur Nachahmung und Untersuchung dieser Strukturen inspiriert. Zum besseren Verständnis der Mechanismen von Anhaftung und Loslösung bei Laubfröschen wurden weiche, elastische und mikrostrukturierte Oberflächen hergestellt, indem PDMS (Polydimethylsiloxan) auf einer Siliziummaske mit Hexagonstruktur aufgetragen und vernetzt wurde. Dadurch wurden Anordnungen von hexagonalen Mikrosäulen mit spezifischen geometrischen Eigenschaften und unterschiedlichen Kontaktgeometrien (normale, flache Form, T-Form und konkave Form der Säulenenden) erhalten. Um den Einfluss der van-der-Waals, hydrodynamischen, Kapillar-und Adhäsionskräfte zu verstehen, wurden verschiedene experimentelle Ansätze verfolgt: Die auf eine einzelne Säule wirkenden Adhäsionskräfte wurden mittels Rasterkraftmikroskopie gemessen. Dazu wurden speziell hergestellte kolloidale Sensoren verwendet. Diese Experimente wurden sowohl mit als auch ohne Flüssigkeitsfilm auf der Säule durchgeführt. Die Ergebnisse zeigten den Beitrag von Kapillarkraft und direkten Kontaktkräften zur Adhäsionskraft bei Vorliegen eines Flüssigkeitsfilms. Die Adhäsion fiel umso größer aus, je weniger Flüssigkeit zwischen Sensor und Säule vorhanden war. Im Falle einer trockenen Adhäsion zeigte die Säule mit T-Form die höchste Adhäsion. Da die Haftscheiben der Laubfrösche weich sind, können sie dynamisch ihre Form ändern, was zu einer Änderung der hydrodynamischen Kraft zwischen Scheibe und Oberfläche führt. Der Einfluss der Oberflächenverformbarkeit auf die hydrodynamische Kraft wurde daher am Modellsystem einer Kugel untersucht, welche sich einer weichen und ebenen Oberfläche annähert. Dieses System wurde sowohl theoretisch über die Simulation finiter Elemente als auch experimentell über die Messung mit kolloidalen Sonden untersucht. Sowohl experimentelle Ergebnisse als auch die Simulationen ergaben eine Abnahme der hydrodynamischen Kraft bei Annäherung des kolloidalen Sensors an eine weiche und elastische Oberfläche. Beim Entfernen der Sensors von der Oberfläche verstärkte sich die hydrodynamische Anziehungskraft. Die Kraft, die zur Trennung eines Partikels von

einer Oberfläche in Flüssigkeit notwendig ist, ist für weiche und elastischen Oberflächen größer als für harte Oberflächen. In Bezug zur Bioadhäsion bei Laubfröschen konnte festgestellt somit festgestellt werden, dass sich der hydrodynamische Anteil zur feuchten Bioadhäsion aufgrund der weichen Oberfläche erhöht. Weiterhin wurde der Einfluss des Aspektverhältnisses der Säulen auf die Reibungskraft mittels eines kolloidalen Sensors untersucht. Gestreckte Säulen zeigten dabei eine höhere Reibung im Vergleich zu. Säulen mit einem gestreckten Hexagon als Querschnitt.

Abstract

Many animals like geckos and tree frogs attach to surfaces by using their special adhesive pads. The pads allow the animal to attach and detach effectively from surfaces under different environmental conditions during locomotion. Particularly, frogs have micro and nano-structured toe pads with specific geometries. Their significant achievement of strong but reversible adhesion in dry and wet habitats has inspired us to mimic and study those structures. In order to understand the attachment and detachment mechanism in tree frogs, soft, elastic micro-patterned surfaces were fabricated by applying certain amount of cross linked PDMS (Polydimethylsiloxane) on a hexagonally patterned silicon mask. Arrays of hexagonal micro-pillars with specific geometrical parameters and different contact geometry (Normal shape, T-shape and, concave cups tips) are obtained. To understand the contributions of van der Waals, hydrodynamic, and capillary forces to adhesion force different experimental approaches have been pursued:
Adhesion force on single pillar is measured by atomic force microscopy using specially designed colloidal probes. Experiments are carried out in presence (wet) and absence (dry) of an intervening liquid layer. The results revealed the contribution of capillary force and direct contact forces to the adhesion in the presence of liquid layer and the adhesion shows the higher value when the less amount of liquid is on the probe. In the case of dry adhesion, the T-shape structure shows the highest adhesion.
Since the toe pads of the frogs are soft, they may easily deform dynamically, which in turn may alter the hydrodynamic force between the pads and a surface. To investigate the influence of surface deformability on hydrodynamic force, we studied the model system of a sphere approaching a soft, planar surface. This system was studied both theoretically by finite element simulations as well as experimentally by colloidal probe measurements. Both experimental and simulation results proved that an elastic, soft surface has the effect of decreasing the hydrodynamic force as a colloidal probe approaches the surface. Hydrodynamic attraction is enhanced when the probe is pulled away. The force required to separate a particle from a soft, elastic substrates in liquid is higher than that for a hard substrate. In the context of bioadhesion, the hydrodynamic contribution to wet bioadhesion increases due to soft adhering surfaces.
In addition, the role of aspect ratio of the pillar on friction force is investigated using colloidal probe. Elongated pillars show the higher friction compared to hexagonal pillars. The friction force is higher at the edge of the elongated pillars.

Acknowledgements

[In der elektronischen Fassung aus Datenschutzgründen entfernt]

Dedicated to *all my teachers in life and science.*

Contents

1 Introduction

1.1 Background and Motivation

Scientific understanding of biological systems requires deep insights from chemical, ecological and even neurological perspective. Although all these perspectives have been useful to unveil the secrets behind several biological systems, the mechanical attachment phenomena has only recently begun to be understood and studied, requiring a deep insight of the surface forces that arise at micro and nano scales. Improvement of available methods as well as the interest in biological systems have helped scientists to learn from nature (biomimetics).

In nature, adhesion helps animals to maintain their position on surfaces, move under different environmental conditions, and attach to surfaces such as plants or other animals temporarily [1]. The dynamic mechanisms of reversible adhesion used by large diversity of animals such as insects, lizards and geckos [2, 3] has become an interesting research area in the last decades. These animals have special attachment pads which allow them to stick to and release effectively from dry surfaces while they are climbing or walking even upside down [4, 5]. These adhesive pads posse special surface design which allow certain animals to have greater contact to surfaces. Beetle, flies, spiders and geckos have particular fibers on their adhesive pads. These fibers become finer as the body weight of the animal increases [6]. Beetles have flat, micron-size adhesive hair whereas geckos have a hierarchical-hairy structure (Figure 1.1). According to the contact splitting theory, splitting up a large contact area into n sub contact areas, leads to enhancement of the pull-off force of hemispherical contacts by a factor of $\sqrt{n}$ [6].

The gecko is one of the well known animals among those which adhere to the dry surfaces. The gecko's adhesion mechanism has been studied very well during the last decade. Its pad consists of dense arrays of hairs with a special contact point (spatula). The tip diameter of the spatula is about 200-300 nm [7]. Using specially designed-hairy pads, geckos are able to attach to surfaces without using intervening fluid such as mucus. They adhere to the surfaces relying on van der Waals forces [8–14]. Over the last decades the contribution of split contact surfaces [6] and spatula tips [15] in the adhesion mechanism of geckos have been well studied. One approach to study such systems is by designing model surfaces which mimic, for instance, a gecko's toe pad or frog's toe pad.

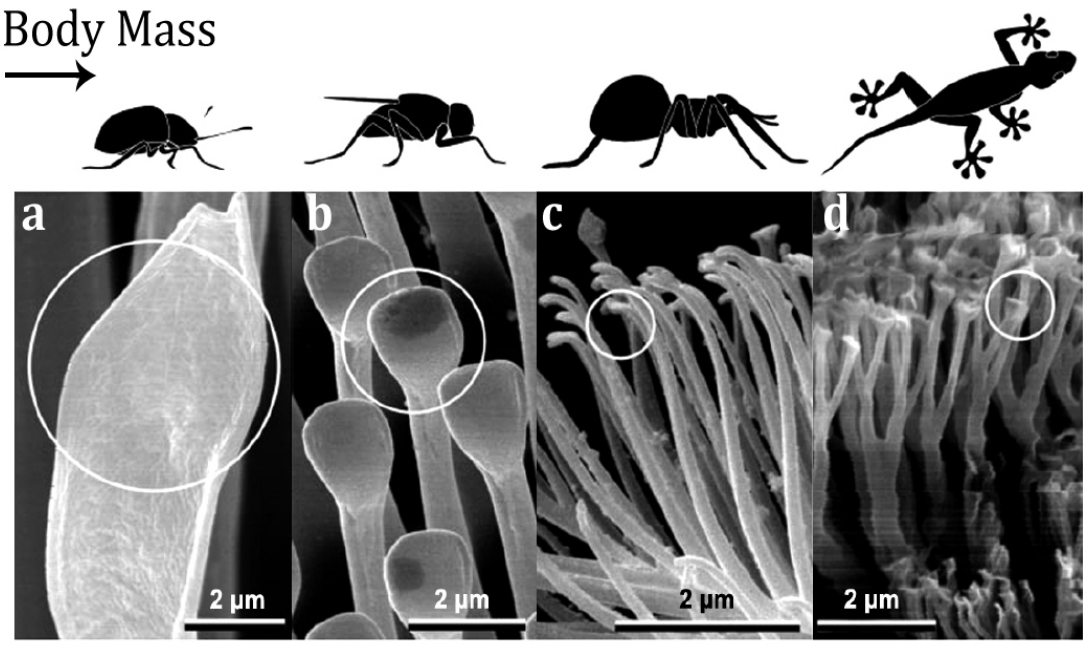

Figure 1.1: SEM images of hairy adhesive pads of different animals, showing finer structures with increasing body weight. The diameters of their spatula-like terminal elements have been measured to spanning ranges 0.2 to 5 µm. (a) beetle, (b) fly, (c) spider, and (d) gecko [6].

Such biomimic surfaces help researchers understand how topographical changes during attachment influence switching between adhesive and non-adhesive states [16–18].

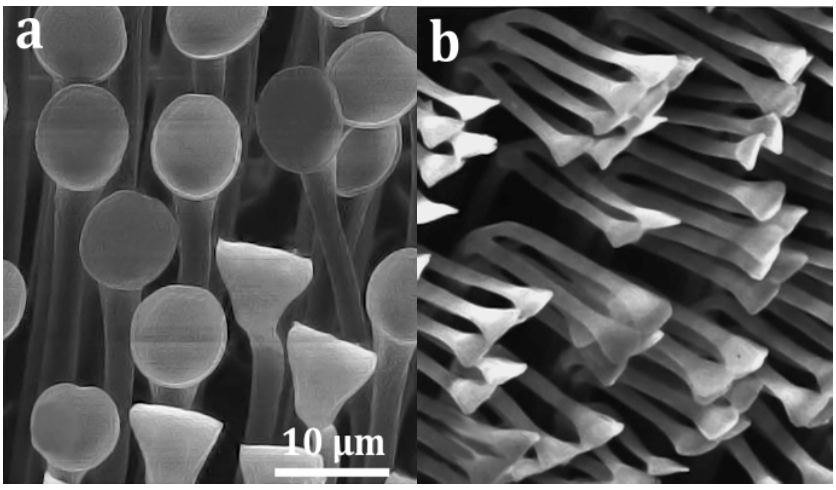

Figure 1.2: SEM image of (a) mushroom-shaped [19] and (b) fibrilar setaes [20].

Compared to the geckos's hierarchical toe pad surface structure, some beetles attach to the surfaces with a different pad design. They use mushroom-shaped tips (Figure 1.2)

to adhere strongly to smooth surfaces and use spatula-shaped fibrils for locomotion, adhesion and as a defense mechanism [19–21].
Another group of animals that are able to cling and walk on wet and flooded surfaces are tree and torrent frogs. The surface of the adhesive pads of tree frogs consists of soft protrusions [22–25]. These protrusions are hexagonal with ca. 10 µm diameter and separated by 1 µm wide channels [22–30]. The top part of the micro-pillars are subdivided into an array of 300-400 nm diameter nano-pillars [22–24]. These nano-pillars are terminated in concave shape [22, 31].

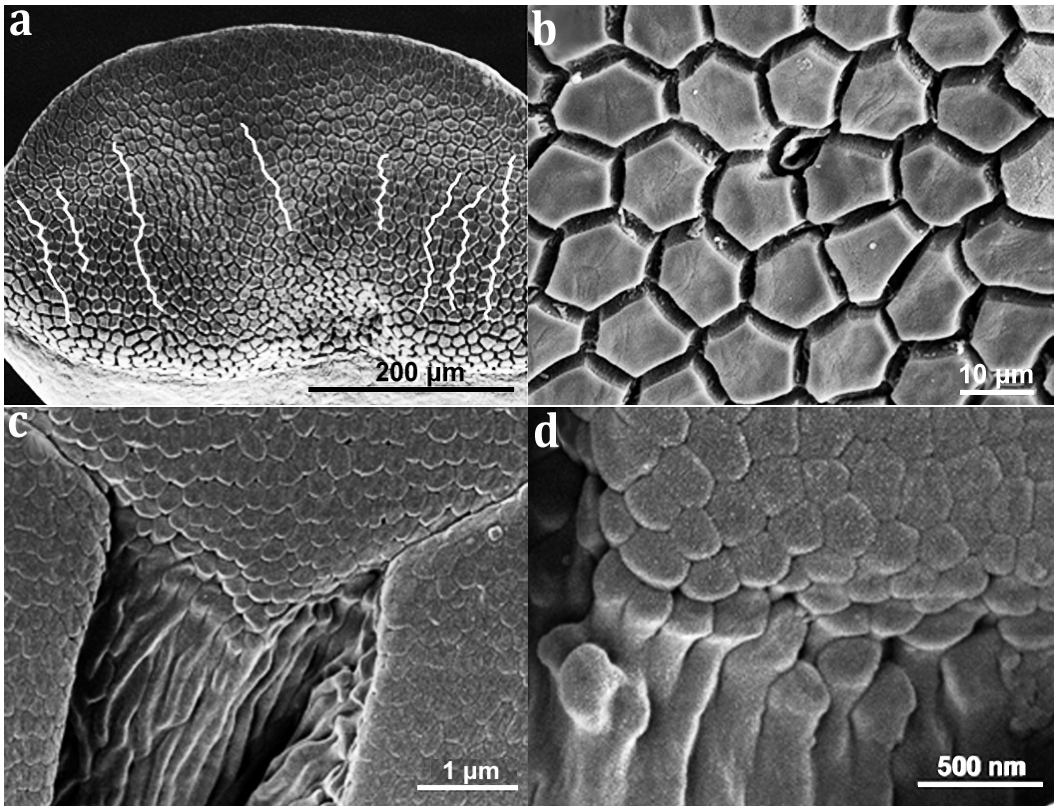

Figure 1.3: Morphology of tree frog's toe pad. (a) A whole toe pad. White lines show relatively straight channels crossing the pad. (b) Polygonal epithelial cells (mainly hexagonal in shape) surrounded by deep channels with a single mucous pore (centre). (c) Edge of a epithelial cell showing intercellular channel and a dense array of nano-pillars covering the pad surface. (d) High magnification view of nano-pillars [32].

Though some research groups have studied the effect of nano-pillars on adhesion forces, the specific role of these features is not clear yet. Some studies have claimed that these features may help tree frogs drain the water out of the contact area [33, 34]. This allows an intimate contact to surfaces [35] and an enhancement of adhesion by suction forces [36] and capillary forces [37–40]. Thereby the adhesive and frictional forces are enhanced while locomotion on wet surfaces. The adhesive pads of tree frogs are wet by mucus that

is squeezed out from the channels between the hexagonal pillars [30].
Effective elastic modulus measurements of the toe pad of the tree frogs using atomic force microscopy based nano-indentation have reported values ranging between 5-15 MPa for the outer, keratinised layer of tree frog toe pads [22]. Elastic modulus measurements on the whole toe pad including the inner structure of the toe pad reveals that the toe pad of the tree frogs are soft [25, 31]. Indentation measurement using a 1.5 mm sphere on the toe pad of the tree frogs revealed an elastic modulus of 4-40 kPa when applying an indentation depth of 350 microns [25, 31].
Hydrodynamic and capillary forces play an important role in adhesion when a fluid is present, whereas they are completely absent in dry adhesion. In wet conditions, a capillary bridge can form on top of single pillar or span over several pillars (Figure 1.4). Theoretical studies showed an increase in adhesion when a single capillary bridge splits into several small bridges over single pillars [40].

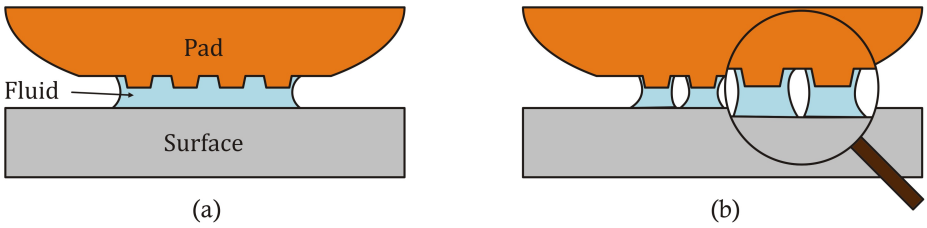

Figure 1.4: Schematic illustration of different amounts of liquid present between pad and substrate: (a) Capillary bridge over several pillars and (b) Capillary bridges on top of several single pillars.

In biological systems, e.g. the bodies, foot pads, or feet of animals such as tree frogs that use wet adhesion to stick to surfaces, the attaching organs (e.g. toe pad) are soft and deform as they are pressed against or pulled away from the substrate to which they stick. Since the toe pad of tree frogs are soft [25, 31], it is essential to study the effect of the softness of the toe pad on capillary and hydrodynamic forces. Recent reports have shown that adhesion forces increase with softer substrates [41, 42].
Under flooded conditions, however, capillary forces are expected to vanish due to the absence of capillary bridge between toe pad and the surface, while hydrodynamic forces continue to be present. The mechanism behind tree frog adhesion and locomotion under flooded conditions, has been subject of speculation. It has been reported that tree frogs can climb and grip in flooded conditions by draining the excess fluid through their toe-pad channels, reducing thus hydrodynamic forces [34, 43, 44].
The mechanisms behind tree frog adhesion are not fully understood yet. However experimental reports on living tree frogs [27, 33, 38, 45] and few theoretical studies [2, 34, 41] have suggested several contributions such as: capillary forces [37, 39, 41, 46], hydrody-

namic forces [33, 38, 44, 45], which are completely absent in dry adhesion for instance in case of gecko [47], and friction forces [33, 34, 48].
Torrent frogs are able to adhere to the surfaces even in flooded environments, where high amounts of liquid are present and the whole frog immersed in the liquid. The toe pad structure in family of torrent frogs consist of elongated pillars. These elongated pillars may be an adaption of the frogs to an environment with higher amounts of liquid compared to tree frogs. It is possible that this pillar shape effectively increases the drainage of the liquid out of the contact surface [49].
Friction is another force that may contribute to the wet adhesion in tree frogs. Friction forces on single toe pad have been studied under dry and wet condition [33].
In wet conditions, the channels between the pillars on the toe pad of the tree frogs might drain the liquid layer out of the contact area and make a dry contact which leads to friction forces [48].
In insects, frictional forces under wet condition have been studied as well as the role of the liquid layer in the attachment mechanism [50].
It has been shown that the presence of the liquid layer enhances the adhesive force on rough surfaces. The contact area increases by filling the gaps with liquid between the surface asperities and the insect's toe pad.
Although the attachment mechanisms of animal adhesive pads are well studied, the mechanism of *control* of adhesion, i.e. the quick change from attachment to detachment remains unknown.
Toe pad of the tree frogs mainly consist of hexagonal cells, whereas torrent frogs have elongated hexagons on their toe pad. Torrent frogs live mostly close to the waterfalls and need to attach to surfaces in presence of thick layer of water. The different topographical structures in tree and torrent frogs are shown in Figure 1.5.

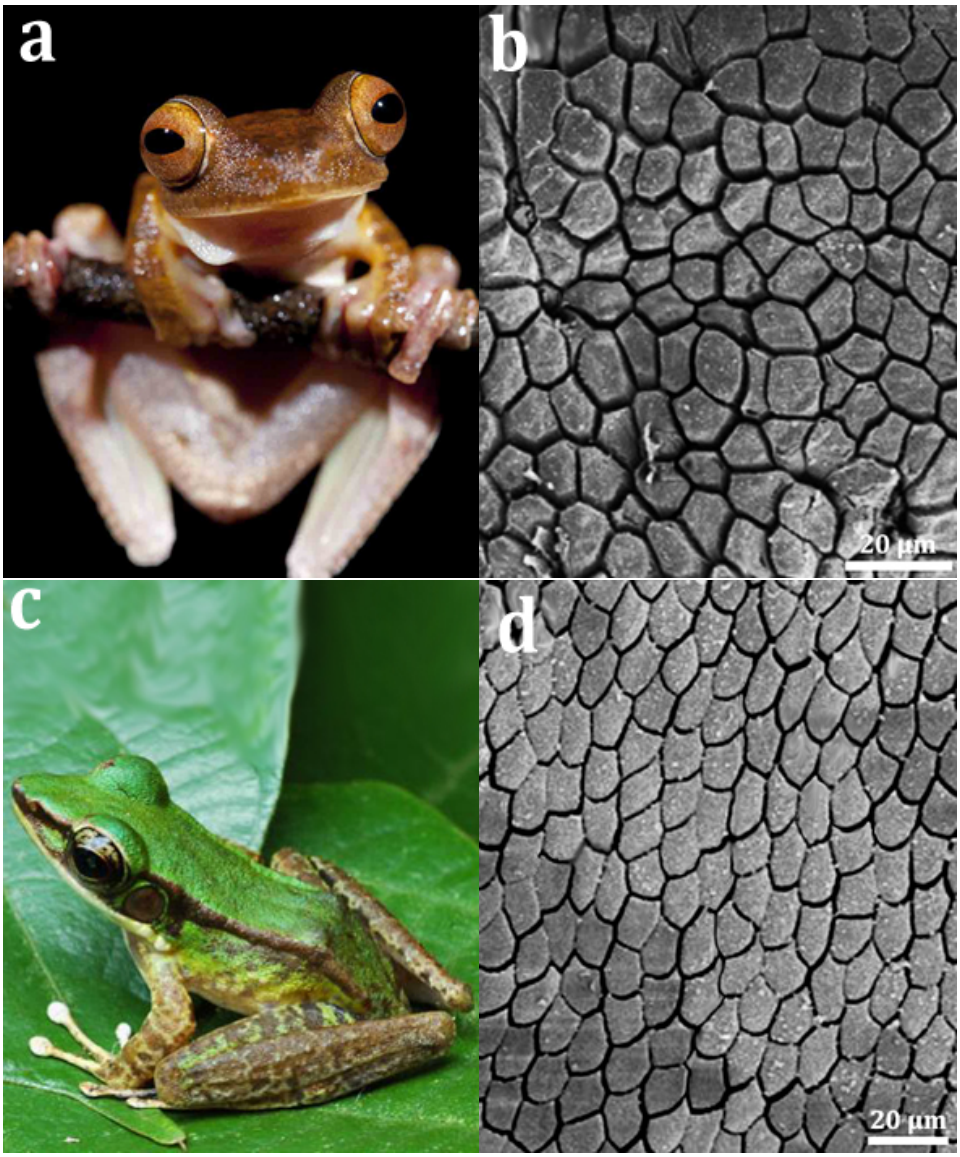

Figure 1.5: (a) Tree frog (Rhacophorus pardalis), (b) SEM image of the tree frog toe pad topography, (c) torrent frog (Odorrana hosii) [51] and (d) SEM image of the torrent frog toe pad topography [52].

The directional dependence of the adhesion and friction forces on tree frogs toe pad [53] as well as the influence of liquid layer on adhesion and friction forces have been studied [48].

Directionality of the adhesive structure, and the direction-dependent forces they generate, seem to be crucial in the locomotion control of adhesive animals [54]. For instance, in case of hairy pads (individual contact points), the individual hair angled tips that provide non sticky states. When the pad is shortly pulled, the tip aligns with the substrate for attachment, whereas a push detaches the hair [9, 55–58].

In smooth pads (almost continuous adhesive surface), internal fibers may act in similar ways to hairy pad directing the fibers at an angle towards the surface [59, 60]. Such directionality has been found in a wide variety of animals such as flies [61], bush crickets [62], ants [63, 64], cockroaches [65], geckos [9, 66] and tree frogs [38].
Endlein *et al.* have shown that tree frogs use friction forces in order to generate high adhesive forces, which might help prevent the peeling of their pads [54]. Friction measurements under wet condition have been performed on flat and micro-structured surfaces. Micro-structured surfaces have shown higher friction than flat surfaces in presence of liquid. Endlein et al. claimed that the increased friction in micro-structured surface is caused by the drainage of liquid through the channels of the contact surface, leading to a dry contact between the surface and top of the pillars [48].
The direction-dependence of adhesion and friction properties of smooth pads have been studied before [53]. When the toe pad pushed away from the body, a significant decrease in adhesion and friction forces was observed. This notable direction dependence could be caused by the peeling of the whole toe pad. The observed directional dependence leads to the control of the attachment and the detachment. This process allows the animal to switch between adhesive and nonadhesive states quickly.
Up to now, man has not been able to reproduce, or biomimic, surfaces which have strong and reversible adhesion in dry, wet (in presence of order of nm liquid layer) and flooded (whole frog immersed in liquid) conditions as the case of tree frogs in the nature. Understanding the reversible adhesion mechanism in tree frogs could open a new window for us to investigate and design artificial analogues. By mimicking the reversible adhesion in tree frogs we could benefit in our daily life by using reversible plasters, non slippery shoes or pavement and strong adhesive tapes.

1.2 Aim of the Thesis

Tree frog adhesion has two seemingly opposing requirements: on one hand tree frogs have to be able to adhere to a surface firmly while, on the other hand they must maintain their maneuverability by detaching quickly. The rising questions are which mechanism(s) tree frogs utilize during attachment? and what kind of forces contribute? Since the adhesion mechanism in tree frogs is not fully understood, this thesis aims at clarifying adhesion in tree frogs by first understanding the adhesion mechanism of the smallest part of the toe pad which is the epidermal cell (single pillar). Studying the smallest-simplest part of a complex system might help to understand the whole system. In order to mimic the structural features and properties of a tree frog's toe pad, an hexagonal patterned array of soft, elastic pillars is prepared. Pillar structures with different terminal shapes and hydrophilic or hydrophobic surface will also be considered in this work. In this

thesis, adhesion forces for single pillars are measured by atomic force microscope (AFM) using specially designed colloidal probes. To separate the different contributions of van der Waals, hydrodynamic, and capillary forces, experiments should be carried out in presence and absence of an intervening liquid layer, using different surfaces, in order to clarify the role of the liquid layer during wet adhesion. To understand how tree frogs walk and climb surfaces, speed dependent experiments are carried out. To compare experimental measurements with theory, numerical simulations of the system are performed yielding valuable information over the relevant forces at play throughout the wet adhesion experiments. Furthermore, to investigate the contribution of friction force in wet adhesion experimental measurement are carried out on pillar arrays. To understand the directional dependence of friction in torrent frogs, which have elongated pillar structures on their toe pads, friction force measurements are performed using the colloidal probe technique.

1.3 Overview

The structure of this thesis is: In ***Chapter 2***, the basics of contact mechanics, including fundamentals of surface forces, like van der Waals, capillary forces, hydrodynamic forces, electrostatic forces, frictions and adhesion forces, as well as the concept of surface energy are introduced. In addition, the well-known contact theories such as Hertz, Johnson-Kendall-Robert (JKR) and DMT model are discussed.
Chapter 3, shows the materials and methods used for the measurements. The substrate preparations are described as well as Scanning Probe Microscopy (SPM) techniques, including imaging and force spectroscopy. Furthermore, the colloidal probe technique is introduced as well as the thermal noise method used for cantilever calibration. In this chapter the sample preparation for hydrodynamic measurements, capillary force measurements, and friction measurements as well as the respective measurement set-up are presented
In ***Chapter 4***, the hydrodynamic force between a sphere and a soft, elastic surface is studied. Moreover, the numerical analysis and finite element simulation of the hydrodynamic force on hard and soft substrates are employed. In the end, experimental and numerical results are compared.
Chapter 5, discusses about the capillary forces that arise between a soft single pillar and a planar surface. The adhesion measurements on soft, structured pillars are performed under dry and wet conditions by specially designed colloidal probes. Furthermore, results from experiments simulated by *Surface Evolver* are shown and discussed.
Chapter 6, presents friction measurements on elongated and hexagonal pillars performed under dry conditions. At the end, in ***Chapter 7*** the results of this thesis are summarized and a conclusion and future outlook are given.

2 Fundamentals

In this thesis, mainly the interfacial forces between different surfaces, such as a micro-particle and a planar surface and planar-planar surfaces are studied experimentally. In order to understand the interaction between those surfaces, it is inevitable to consider the elastic properties of the surfaces as well as surface forces acting between them. Thus, this chapter covers fundamentals of forces acting between interfaces (solid-solid, solid-liquid and liquid-gas), surface energy and contact mechanics.[1]

2.1 Surface Forces

Surface forces are the forces that act between the surfaces of two solid bodies. The interaction between solid bodies is strongly influenced by surface forces. It is important to study surface forces, since in many applications of the research controlling the forces between particles, between particles and surfaces or between two surfaces is required. Surface forces not only could explain the behaviour of dispersions, emulsions and foams, but also some phenomena like wetting, adhesion and adsorption.
The term "surface force" includes forces between solids in a fluid medium as well as all different kinds of interfaces. An interface is the area that separates two phases. For instance, if the solid, liquid, and gas phases were considered, three combination of interfaces are possible: the solid-liquid, the solid-gas, and the liquid-gas interfaces.
Different kinds of attractive and repulsive surface forces do exist. They strongly depend on the surfaces and the enclosing medium which are involved. For instance, van der Waals forces which act between any molecules, capillary forces which exist between surfaces in presence of liquid meniscus or hydrodynamic forces which are present when two surfaces move relative to each other in a fluid.
In this work, some of the aforesaid surface forces are studied. First of all, the adhesion force between a planar particle and soft-elastic solid surfaces in air and in presence of fluid, then the hydrodynamic forces between a specially designed colloidal probe and soft-elastic surface and finally the friction forces between a particle and soft-elastic surface.

[1] This chapter is mainly based on [67] and [68].

2.1.1 Adhesion Force

The adhesion force is an attractive force. When two surfaces are in contact, the maximum force needed to overcome the attractive interaction and separate the surfaces is equal to adhesion force [67]. The adhesion force depends on how strong the attractive force between two surfaces are, the minimum distance between them and the established contact area.
Many forces may contribute to the adhesion like van der Waals forces, electrostatic forces, chemical forces, capillary forces, hydrodynamic forces and some other forces. The adhesion force between two surfaces is the sum of all possible relevant attractive interactions.

$$F_{adh} = F_{vdW} + F_{electrostatic} + F_{chemichal} + F_{capillary} + F_{hydrodynamic} + ... \tag{2.1}$$

2.1.2 Electrostatic Forces

Slow-moving or stationary electrical charges on objects lead to an electrostatic force. Depending on the polarity of the objects, the bodies can have a surface charge which leads to attraction or repulsion.
The electrostatic force between two non-conductive spheres with radii of R_1 and R_2, in a medium with the permittivity of ε_r (Figure 2.1) is determined by

$$F_{el} = \frac{\pi}{\varepsilon_0 \varepsilon_r} \cdot \frac{Q_1 Q_2 R_P^2}{\left(1 + \frac{D}{2R_P}\right)^2} \tag{2.2}$$

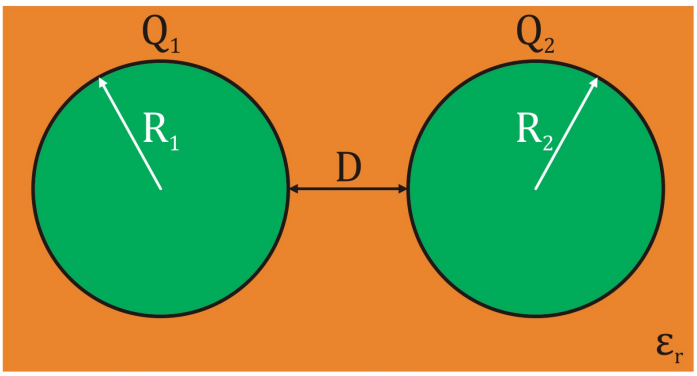

Figure 2.1: Schematic illustration of the electrostatic force between two spheres in a medium with the permittivity of ε_r.

where Q_1 and Q_2 are the surface charges of the spheres, $R_1 = R_2 = R_P$ the sphere radius, D the distance between the spheres and $\varepsilon_0, \varepsilon_r$ the permittivity of vacuum and the surrounding medium, respectively. For antipolar charged spheres, Equation 2.2 leads to an attractive force and for unipolar charged spheres, the force is repulsive.

2.1.3 Van der Waals Forces

Van der Waals force is one of the main contributions to the adhesion force between two solid bodies. Van der Waals force is a type of intermolecular force, which exists between all sort of atoms and molecules, even apolar ones such as helium.
Intermolecular forces are feeble; but without them, life would be impossible. For instance, water would not condense from vapor into liquid if its molecules did not attract each other.
Intermolecular forces are responsible for many properties of molecular compounds, including crystal structures (e.g. the shapes of snowflakes) and surface tension. Intermolecular forces pin gigantic molecules like enzymes, proteins, and DNA into the shapes required for biological activity. Van der Waals forces include all dipolar intermolecular forces that act between electrically neutral molecules and they may arise from three different sources.

1. **Keesom interaction**: explains the interaction between two permanent dipoles (Figure 2.2). The most prominent example of dipole interaction are water molecules. Oxygen is more negatively charged compared to more positively charged hydrogen. The interaction of two water molecules can be described as the interaction of two dipoles. They both influence their mutual orientation. The dipoles prefer to orient with their opposite charges facing each other. At the same time, the thermal motion leads to an orientational fluctuation pushing them away from the preferential orientation. The dipole-dipole interaction for freely rotating dipoles with their dipole moments μ_1 and μ_2 is given by:

$$V(D) = -\frac{C_K}{D^6} = -\frac{\mu_1^2 \mu_2^2}{3(4\pi\varepsilon_0)^2 k_B T D^6} \tag{2.3}$$

   The tendency of such permanent dipoles to align with each other results in a net attractive force. The force between two permanent dipoles is called Keesom force and it depends on the thermal energy ($k_B T$), the distance between the dipoles D, the dipole moments μ_1 and μ_2 and the vacuum permittivity ε_0.

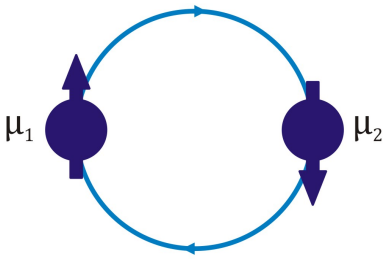

Figure 2.2: Schematic illustration of the van der Waals interaction between two dipoles (Keesom interaction).

2. **Debye interaction**: explains interaction between a permanent dipole which is free to rotate and a corresponding induced dipole. Dipoles are not always permanent. They could be also induced by an external field (Figure 2.3). The permanent dipole moment μ of one molecule, induces a dipole moment $\mu_{ind} = \alpha \cdot E$ in the second molecule with the polarizability α. Here E is the electric field strength created by presence of the permanent dipole. This leads to Debye force which is described by:

$$V(D) = -\frac{C_D}{D^6} = -\frac{\mu^2 \alpha}{(4\pi\varepsilon_0)^2 D^6} \tag{2.4}$$

Equation 2.4 also describes the interaction between two identical polarizable molecules with permanent dipole moments μ and polarizabilty α due to mutually induced dipole moments that lead to a Debye interaction in addition to the Keesom interaction.

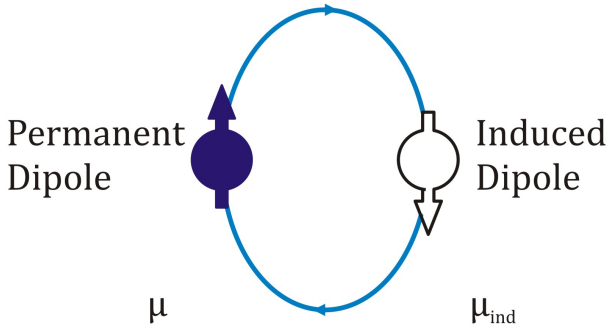

Figure 2.3: Schematic illustration of the van der Waals interaction between a permanent dipole and an induced one (Debye interaction).

3. **London interaction**: explains interaction between two instantaneously induced dipoles (Figure 2.4). In classical electrodynamics we would not expect any interac-

tion for non polar molecules however the quantum mechanics could nicely describe it. London dispersion interaction originates from the fluctuation of the charge distribution from protons and electrons in atoms. The polarity changes very fast, but this nevertheless results in a fluctuating dipole. London dispersion interactions are also known as dispersion forces. It is calculated as the following:

$$V(D) = -\frac{C_L}{D^6} = -\frac{3\alpha_1\alpha_2}{2(4\pi\varepsilon_0)^2 D^6}\frac{h\nu_1\nu_2}{(\nu_1+\nu_2)} \tag{2.5}$$

α_1 and α_2 are the polarizabilities of the molecules and $h\nu_1$ and $h\nu_2$ are their ion-

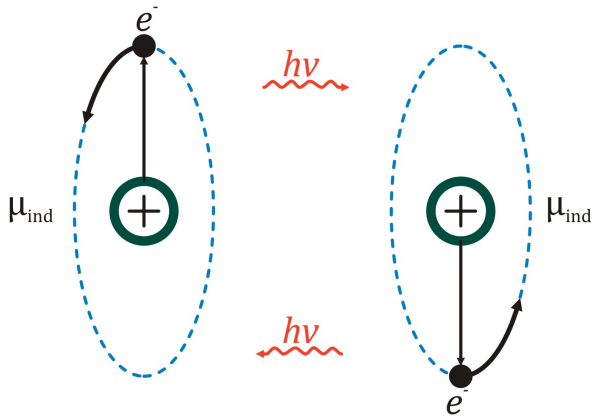

Figure 2.4: Schematic illustration of the van der Waals interaction between two induced dipole (London interaction)

ization energies.
The attraction between two nonpolar molecules can be explained by the London dispersion interaction using quantum mechanics and not classical physics. However, also polar molecules interact via dispersion forces, and not only via Keedom and Debye forces.

$$V_{vdW}(D) = -\frac{C_{vdW}}{D^6} \quad \text{with} \quad C_{vdW} = C_{Keesom} + C_{Debye} + C_{London} \tag{2.6}$$

The attractive van der Waals force is the sum of the Keesom, the Debye and the London dispersion interaction, it means all the terms that consider dipole interactions. All three terms contain the same distance dependence ($\propto -1/D^6$).
The total intermolecular pair potential is summation of the attractive and repulsive potentials. Intermolecular forces have two contributions: the van der Waals force which is an long-range attractive term ($\propto -1/D^6$) and the repulsive term ($\propto -1/D^{12}$) describing

the Pauli repulsion at short ranges due to overlapping electron orbitals.
There are two approaches to calculate the van der Waals force between macroscopic solids: the microscopic and the macroscopic approach [69].

Van der Waals Interaction-Microscopic Approach

The microscopic approach was developed by Hamaker [70]. In this approach, the interaction energy between two macroscopic solids is calculated by pair-wise addition of all single potential energies between a molecule in solid A and every molecule in solid B, neglecting the influence of the neighboring molecules on this interaction (Figure 2.5).

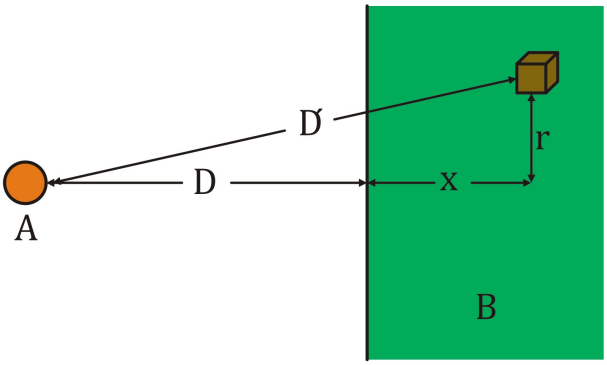

Figure 2.5: Schematic illustration of the van der Waals energy between a molecule A and an infinitely extended solid of molecules B with planar surface.

The potential energy between two molecules A and B is simply described before with Equation 2.6. By integration of the molecular density (ρ_B) over the entire volume of the solid the interaction energy will be calculated:

$$\begin{aligned} V_{molculeA/planeB} &= -C_{AB} \iiint_V \frac{\rho_B}{D'^6} dV \\ &= -C_{AB}\rho_B \int_0^\infty \int_0^\infty \frac{2\pi r}{((D+x)^2+r^2)^3}\, dr\, dx \\ &= -\frac{\pi \rho_B C_{AB}}{6D^3} \end{aligned} \tag{2.7}$$

The minus sign arises because of the attraction. C_{AB} is a positive term. This potential is longer range ($1/D^3$) compared to the potential of the single molecules ($1/D^6$) because

this interaction is determined by the closest surface molecules and the molecules in the bulk.
To calculate the van der Waals energy between two infinitely extended solids A and B which are separated by a parallel gap of the thickness D Equation 2.7 has to be integrated over all the molecules in the solid A, which results into the van der Waals energy per unit area:

$$\begin{aligned} w = \frac{V_{planeA/planeB}}{A} &= -\frac{\pi \rho_A \rho_B C_{AB}}{6} \int_0^\infty \frac{1}{(D+x)^3}\, dx \\ &= -\frac{A_H}{12\pi D^2} \end{aligned} \tag{2.8}$$

ρ_A and ρ_B are the molecular densities in solids A and B, respectively. A_H is the Hamaker constant which is defined as:

$$A_H = \pi^2 C_{AB} \rho_A \rho_B \tag{2.9}$$

The Hamaker constant depends only on the material characteristics.
The force per unit area is given by the negative derivative of the energy per area w:

$$f = -\frac{A_H}{6\pi D^3} \tag{2.10}$$

In a similar way, it is possible to calculate the van der Waals energy between solids with different geometries. Important geometries for many applications are the van der Waals interaction between spheres or a sphere and a planar surface.
In sphere-sphere van der Waals interaction (Figure 2.6), we assume that the radii R_1 and R_2 are significantly larger than the distance between them (D). The potential energy is:

$$V(D) = -\frac{A_H}{6D} \cdot \frac{R_1 R_2}{R_1 + R_2} \quad \text{for} \quad D \ll R_1, R_2 \tag{2.11}$$

and the van der Waals force

$$F_{vdW} = -\frac{dV(D)}{dD} = -\frac{A_H}{6D^2} \cdot \frac{R_1 R_2}{R_1 + R_2} \qquad \text{(sphere-sphere)} \tag{2.12}$$

By letting R_2 approaching infinity, one obtains the case of a sphere-plane interaction (Figure 2.7) and Equation 2.12 simplifies to

$$F_{vdW} = -\frac{A_H}{6D^2} \cdot R \qquad \text{(sphere-plane)} \tag{2.13}$$

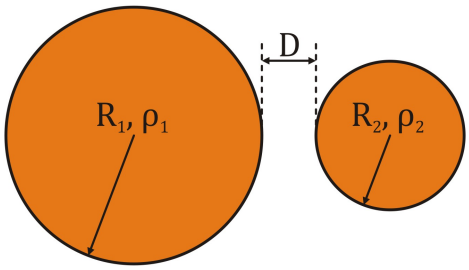

Figure 2.6: Schematic illustration of the van der Waals interaction between two spheres.

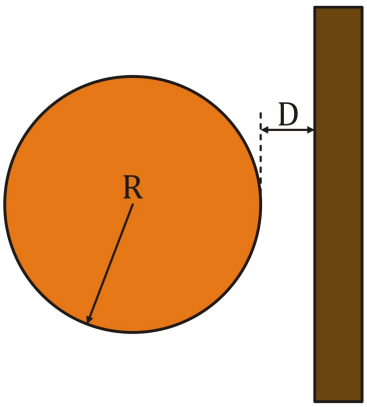

Figure 2.7: Schematic illustration of the van der Waals interaction between a sphere and a planar surface [67].

As it is evident from Hamaker calculations, the distance dependence of van der Waals force between macroscopic solids follows a different scaling law compared to the distance dependence for single molecules (D^{-6}).

Van der Waals Interaction-Macroscopic Approach

In the microscopic approach of van der Waals interaction, additivity of the single molecular potentials is assumed. However, this is not a correct assumption, since the van der Waals energy between two molecules in the presence of a third molecule will change. In the macroscopic approach, Lifshitz developed a theory which is based on neglecting the atomic structure and treating the solids as continuous media with certain optical properties like permittivity and refractive index.
It turned out that the Lifshitz theory predicts the same, the distance dependency, which

was derived by Hamaker, but the way the Hamaker constant is calculated is different. Lifshitz calculated the Hamaker constant between two dielectric half-spaces parallel planes of materials 1 and 2, separated by a distance D in vacuum [71]. This theory was extended together by Dzyaloshinskii and Pitaevskii [72] by including the effect of a third dielectric medium filling the gap between the plates (Figure 2.8).
In Lifshitz configuration, material 1 and 2 interact by exchanging the virtual photons. This exchange will be influence by the third medium, in between the gap with refractive index larger than 1. The intervening medium increases the optical path of photons and it causes a reduced interaction.
The Hamaker constant for material 1 interacting with material 2 across medium 3 is

$$A_H = \frac{3}{4} k_B T \cdot \left(\frac{\varepsilon_1 - \varepsilon_3}{\varepsilon_1 + \varepsilon_3}\right) \cdot \left(\frac{\varepsilon_2 - \varepsilon_3}{\varepsilon_2 + \varepsilon_3}\right) + \frac{3h}{4\pi} \int_{\nu 1}^{\infty} \left(\frac{\varepsilon_1(i\nu) - \varepsilon_3(i\nu)}{\varepsilon_1(i\nu) + \varepsilon_3(i\nu)}\right) \cdot \left(\frac{\varepsilon_2(i\nu) - \varepsilon_3(i\nu)}{\varepsilon_2(i\nu) + \varepsilon_3(i\nu)}\right) d\nu \tag{2.14}$$

Where h is the Planck constant, ε_1, ε_2 , ε_3 are the static dielectric permittivities of the

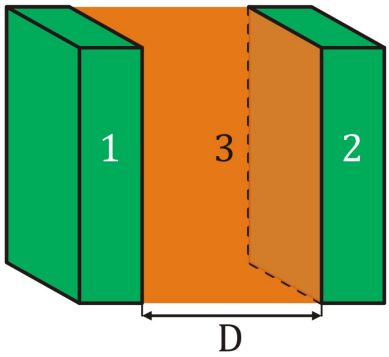

Figure 2.8: Schematic illustration of two parallel half-spaces made from the materials 1 and 2, respectively. The distance between the two parallel half-spaces, D, is filled with the material 3 [67].

three media, which are the values of the dielectric function at zero frequency, and the permittivities $\varepsilon_1(i\nu)$, $\varepsilon_2(i\nu)$, $\varepsilon_3(i\nu)$ at imaginary frequencies $i\nu$. In Equation 2.14, the first term, represents the Keesom and Debye energy.
The permittivity for a nonconductive material can be approximated by

$$\varepsilon(i\nu) = 1 + \frac{n^2 - 1}{1 + \nu^2/\nu_e^2} \tag{2.15}$$

with the refractive index n and the mean ionization frequency ν_e of the material, which is normally in the order of $3 \cdot 10^{15}$ Hz. By assuming that the ionization frequencies of the three materials are the same, the following approximation will be obtained:

$$A_H \approx \frac{3}{4} k_B T \cdot \left(\frac{\varepsilon_1 - \varepsilon_3}{\varepsilon_1 + \varepsilon_3}\right) \cdot \left(\frac{\varepsilon_2 - \varepsilon_3}{\varepsilon_2 + \varepsilon_3}\right) + \frac{3h\nu_e}{8\sqrt{2}} \cdot \frac{(n_1^2 - n_3^2) \cdot (n_2^2 - n_3^2)}{\sqrt{n_1^2 + n_3^2} \cdot \sqrt{n_2^2 + n_3^2} \cdot \left(\sqrt{n_1^2 + n_3^2} + \sqrt{n_2^2 + n_3^2}\right)} \tag{2.16}$$

where n_1, n_2, n_3 are the refractive indices of the three materials.
The Hamaker constant can be either positive or negative. If A_H is positive, it corresponds to an attractive force and when A_H has a negative value, it corresponds to a repulsive force. Thus, in contrast to van der Waals forces between single molecules, that are always attractive, van der Waals interactions between macroscopic solids could be either attractive or repulsive. Using Equation 2.16 it is possible to determine the sign of A_H and therefore the nature of the force. For instance, van der Waals forces between similar materials ($\varepsilon_1 = \varepsilon_2$, $n_1 = n_2$) and between different materials in vacuum or gases ($\varepsilon_3 = n_3 = 1$) are always attractive, whereas forces in a condensed phase, between different materials can also be repulsive.
To estimate the Hamaker constant, Equation 2.16 is a good approximation. More precise values can be obtained from spectroscopic data taking all frequencies into account. This sort of calculation leads to more precise values. For nonconducting materials, Hamaker constant are usually in the order of $10^{-21} - 10^{-20}$J and in case of metals they are about one order of magnitude larger; typically in the range of 10^{-19}J.

2.1.4 Capillary Force

Presence of even trace amounts of vapor in the atmosphere influences the adhesive and mechanical properties of many substrates. For instance, the swelling of certain polymers into gels and the adhesion of powders and sand are distinctly dependent on the relative humidity in the atmosphere. Condensable vapors in the surrounding atmosphere can have a profound effect on adhesion strength.
Capillary condensation happens when liquids, that wet or have a small contact angle on surfaces, spontaneously condense from vapor into the cracks and gaps between surfaces (Figure 2.9). This condensation forms a liquid meniscus in the contact area and therefore leads to an attractive force between two bodies [73]. Capillary forces play an important role in the adhesion between surfaces and particles to surfaces [74].
In order to understand capillary forces, the basic concepts and equations that describe liquid surfaces are presented in the following section.

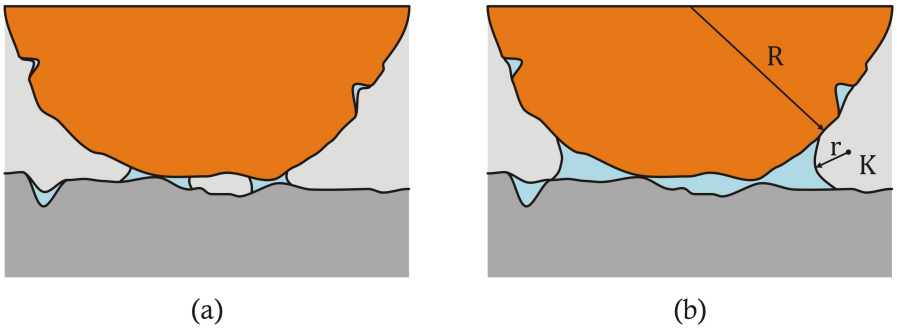

Figure 2.9: Capillary condensation of liquids at (a) contact junctions and (b) in pores and cracks.

Surface Tension

The surface tension of a liquid is one of the basic quantities behind capillary forces. By considering a liquid-vapor interface on the microscopic scale, we can describe the concept of surface tension.
All molecules in the bulk, which are fully surrounded by adjacent molecules, attract each other by forces such as van der Waals forces or hydrogen bonds. However, the liquid molecules at the interface are only partially surrounded by adjacent molecules (Figure 2.10).

This is energetically unfavorable, therefore to bring a molecule from the bulk to the

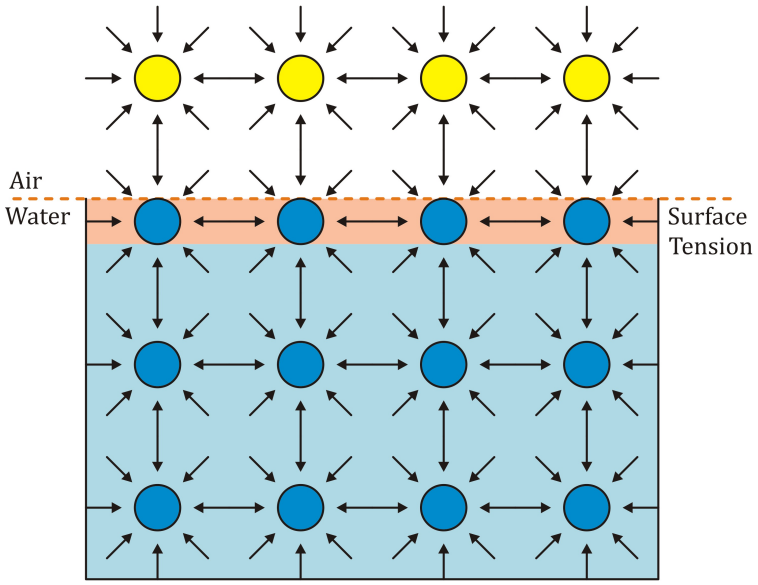

Figure 2.10: Schematic illustration of liquid surface tension.

interface and increase the surface area of the liquid by dA the work dW has to be done:

$$dW = \gamma_L \cdot dA \tag{2.17}$$

The constant γ_L is called the surface tension of the liquid. It depends on the composition of the liquid and vapor, temperature and pressure. By increasing the number of molecules N at the interface, the surface area of a liquid increases. Thus, surface tension is a measure of the interaction strength between the liquid molecules. It has the unit of (N/m) or (J/m^2).

Young-Laplace Equation

In equilibrium, when the curvature of the meniscus is concave or convex, there is a pressure difference between the two phases. The Young-Laplace Equation [75, 76] describes the relation between pressure difference and the curvature of the meniscus.

$$\Delta P = \gamma_L \cdot \left(\frac{1}{R_1} + \frac{1}{R_2} \right) \tag{2.18}$$

where R_1 and R_2 are the principal radii of curvature. This can be explained by the following example: Consider a tube that is closed at one end with a piece of stretched rubber (Figure 2.11). As long as the pressures on both sides of the rubber membrane are equal, it will stay planar. In general, the surface tension tries to minimize the surface area. If the pressure inside the tube is different from the pressure outside it, a curved surface forms. Pressure difference makes the membrane bulge in or out of the tube depending on the direction of the pressure gradient.

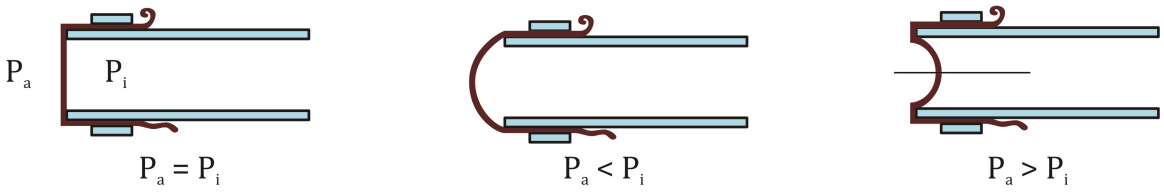

Figure 2.11: Scheme illustrating the Laplace pressure: The end of a tube is closed with a stretched rubber membrane. In order to curve the surface, the inner pressure P_i has to be different from the outside pressure P_a.

The pressure difference, ΔP, is called the Laplace pressure. If we consider a droplet in its vapor or a bubble in a liquid, the two principal radii are identical $R_1 = R_2 = R$. This leads to a Laplace pressure of $\Delta\ P\ =\ 2\ \gamma_L / R$.
The Young-Laplace equation has some fundamental implications:

- If we know the shape of a liquid surface, we know its curvature and therefore the pressure difference (ΔP) across the interface.
- The equilibrium shape of a liquid surface can be calculated with the help of the Young-Laplace equation. If the pressure difference and some boundary conditions, such as the volume of the liquid and its contact line, are known then the geometry of the liquid surface cab be inferred.

Contact Angle

The wetting of a surface by a liquid can be quantitatively described by Young's equation. When a liquid drop is placed on a solid surface, depending on its surface energy, the liquid has two possibilities: either spreads completely on the surface (contact angle $\Theta = 0$) or the edge of the drop forms a finite contact angle Θ between the tangent of the drop at the point of contact and the surface (Figure 2.12).

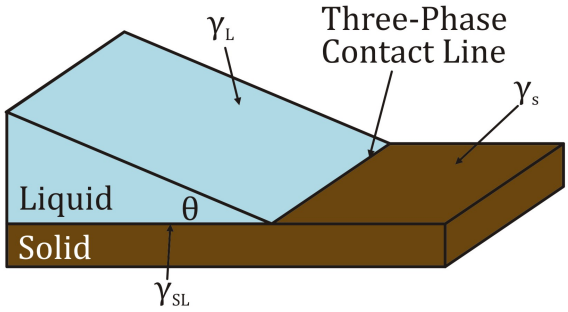

Figure 2.12: Schematic illustration of a liquid drop on a flat solid surface with a contact angle Θ.

This contact point defines a three-phase (solid-liquid-vapor) contact line around the drop, or bubble. *Young's equation* relates the contact angle to the interfacial surface tensions, γ_S, γ_L and γ_{SL}, by:

$$\gamma_{SL} + \gamma_L \cos\Theta = \gamma_S \tag{2.19}$$

The contact angle gives information about a liquid ability to spread over a certain solid surface and is an inverse measure of wetting. A contact angle of $\Theta = 0$ corresponds to full wetting, which indicates that the surface is hydrophilic. The terms hydrophilicity and hydrophobicity of surfaces can be defined by the contact angle of a water droplet sitting on the surface: if a liquid forms a contact angle smaller than or equal to 90 °, $\Theta \leqslant 90°$ the surface is called hydrophilic, and if it forms a contact angle larger than 90 °,

$\Theta > 90°$ it is called hydrophobic.
The common method to measure liquid contact angles and surface tension is the *sessile drop method*.

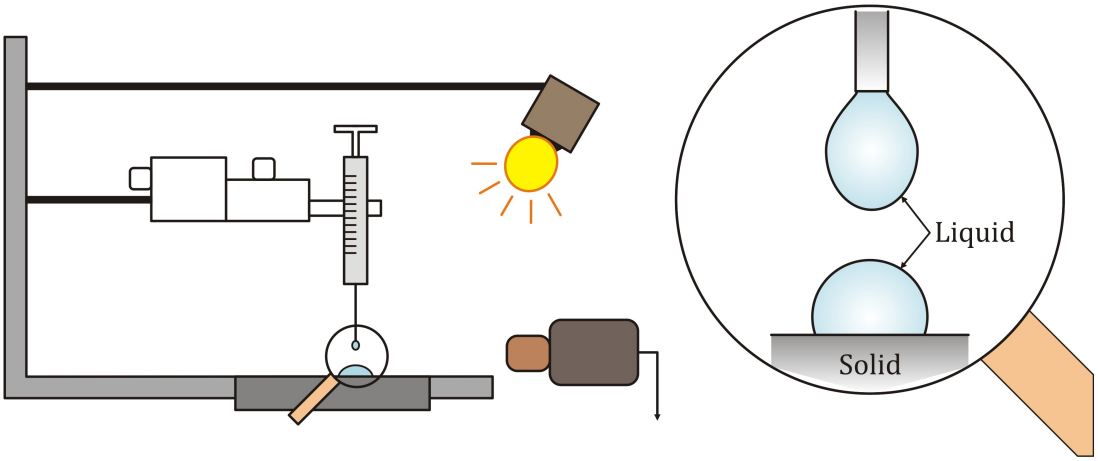

Figure 2.13: Schematic illustration of a sessile drop set-up.

In this specific method the shape of the droplet is analyzed. The method consists in placing a small droplet of liquid using a syringe on top of a flat surface. This liquid droplet is illuminated by a light source, placed behind it. The static drop is then imaged laterally by a microscope (Figure 2.13). The imaged contour of the droplet is fitted by the Young-Laplace equation, assuming rotational symmetry around the vertical axis.

2.1.5 Capillary Force Between a Sphere and a Plane

A smooth, hard sphere of radius R_1 is placed at a distance D from a hard plane in presence of a liquid (Figure 2.14). The liquid forms a contact angle of θ_1 with the sphere and θ_2 with the plane. To calculate the shape of the liquid meniscus, the Laplace equation with appropriate boundary conditions is solved.
As it is shown in Figure 2.14 the curvature of the liquid is characterized by two radii: the azimuthal radius l and the meridional radius r, perpendicular to it. The total radius of curvature of the liquid surface $(1/r_1 + 1/r_2)$ is $(1/l - 1/r)$. Therefore, the pressure difference is $\Delta P = \gamma_L(1/l - 1/r)$.

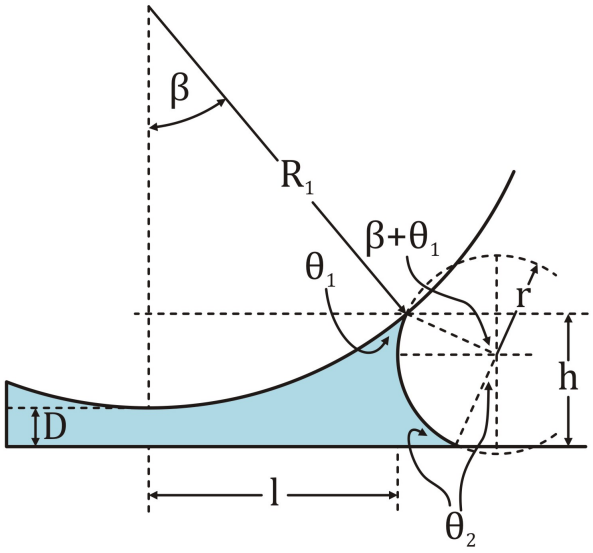

Figure 2.14: Schematic illustration of a spherical particle of radius R_1 at a distance D from a planar surface. The angle β describes the position of the three-phase contact line on the surface of the particle, and h is the height of the meniscus.

Since $l \gg r$, the curvature is negative, that is, the pressure within the liquid is lower than outside. The pressure gradient acts upon a cross sectional area πl^2 leading to an attractive forces of $-\pi l^2 \Delta P$. The total capillary force is

$$F_{Capillary} = 2\pi l \gamma_L - \pi l^2 \Delta P \tag{2.20}$$

Here, $2\pi l \gamma_L$ is the force caused by the surface tension of the liquid. The second term is Laplace pressure force, which is proportional to the pressure difference between inside and out side of the liquid. ΔP, can be expressed by the curvature of liquid surface (H) and surface tension (γ_L).

$$F_{Capillary} = 2\pi l \gamma_L - \pi l^2 (\gamma_L H) \tag{2.21}$$

Since capillary forces are always attractive, a positive sign was applied to attraction. And capillary forces can be repulsive if surfaces are hydrophobic. To calculate the capillary force, it is convenient to introduce the parameter

$$c = \frac{1}{2}[\cos(\Theta_1 + \beta) + \cos\Theta_2] \tag{2.22}$$

For small menisci, where $R_1 \ll l$, the angle β is small and can be neglected and c simplified to

$$c = \frac{1}{2}[\cos\beta + \cos\Theta_2] \tag{2.23}$$

With the given geometry, the two radii of curvature can be expressed in terms of β.

$$h = 2rc \quad \text{and} \quad h = R_1(1 - \cos\beta) + D \tag{2.24}$$

Setting both expressions equal leads to

$$r = \frac{R_1(1 - \cos\beta) + D}{2c} \tag{2.25}$$

and

$$l = R_1 \sin\beta - r[1 - \cos(\Theta_1 + \beta)] \tag{2.26}$$

The capillary force is then derived by using Equations 2.20, 2.25, and 2.26. In this case the narrowest part of the meniscus is used for the calculation. The capillary force is

$$F_{Capillary} = \pi\gamma R_1 \sin\beta[2\sin(\Theta_1 + \beta) + R_1 \sin\beta \cdot (\frac{1}{r} - \frac{1}{l})] \tag{2.27}$$

2.2 Surface Energy and Adhesion Energy

In case of liquid, to enhance the surface area, dA, the energy dW, is required, which is described by:

$$dW = \gamma_L \cdot dA, \tag{2.28}$$

where γ_L is the surface tension of the liquid. For liquids, an enhancement in surface area is straightly related to an enhancement in the number of molecules N at surface while the area per molecule σ_A stays constant. Thus, surface energy and surface tension are identical.
However, in case of solids, the surface area of the solid can be enhanced in two possible ways: either to enhance the number of molecules N at the surface like the case of liquids which corresponds to a plastic change or to stretch the surface elastically, which leads to enhancement of σ_A while the number of surface molecules is constant. As a consequence, the surface energy γ^S has two contributions: plastic and elastic [67].

$$dW = \gamma^S dA = d(E_s N) \quad \text{with} \quad \gamma^S = E_S \frac{\partial N}{\partial A} + N\frac{\partial E_S}{\partial A}, \tag{2.29}$$

where E_S is an excess energy, which is associated with each molecule.
For a purely plastic change in surface area, the surface energy is similar to that of a liquid and is called surface tension of the solid:

$$\gamma^S_{plastic} \equiv \gamma_S, \tag{2.30}$$

And for a purely elastic change, N is constant and changes in surface area is due to a change in the area per molecule. The change in surface energy is the sum of surface tension and the change of surface tension with the elastic strain $\varepsilon_{elastic}$.

$$\gamma^S_{elastic} = \gamma_S + \frac{\partial \gamma_S}{\partial \varepsilon_{elastic}} \equiv \Upsilon, \tag{2.31}$$

where Υ is called *surface stress*. Generally, new surface area is a consequence of contributions of elastic and plastic change. Therefore, the surface energy of a solid is:

$$\begin{aligned} \gamma^S &= \gamma_S + \frac{\partial \gamma_S}{\partial \varepsilon_{tot}} \\ &= \gamma_S \frac{d\varepsilon_{plastic}}{d\varepsilon_{tot}} + \Upsilon \frac{d\varepsilon_{elastic}}{d\varepsilon_{tot}}, \end{aligned} \tag{2.32}$$

$\varepsilon_{tot} = dA/A$, is the total strain and $\varepsilon_{plastic}$ is the plastic strain. Thus, to expand the surface against the surface tension γ_S and the surface stress Υ, work has to be done.
For the calculation of adhesion forces, the surface energy of solids is of great significance. Since a detailed calculation of all contributing surface forces is not easy, surface energy considerations are often used instead. The surface energy consideration of solids is a simpler approach to calculate adhesion forces.
To split a crystal with cross-sectional area A, one needs to create two new surfaces with total area of $2A$. The work has to be done to break all cohesive bonds in the interface (Figure 2.15).

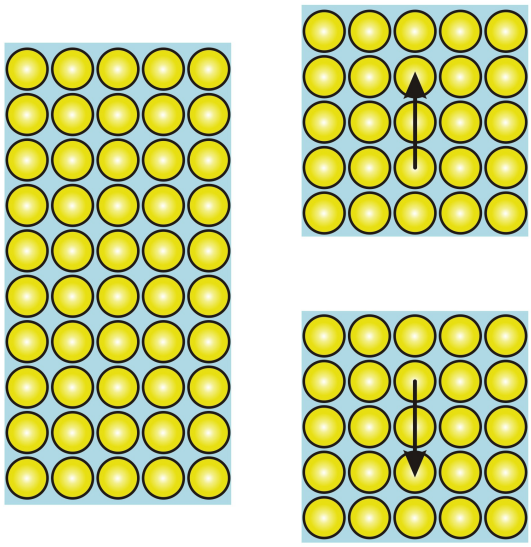

Figure 2.15: Schematic of a cleavage of a crystal.

The newly obtained surface is in a very high energetic state because the energy used to make the bonds, is now available at the surface. To split two blocks of different materials 1 and 2 with surface energy γ_1^S and γ_2^S and interfacial energy γ_{12} , the necessary work per unit area is:

$$w_{adh} = \gamma_1^S + \gamma_2^S - \gamma_{12} \tag{2.33}$$

where w_{adh} describes the adhesion strength between two materials and is called the work of adhesion or the adhesion energy. For instance, adhesion energy for two identical materials becomes the work of cohesion which is $w = 2\gamma^S$.
Due to the surface roughness and surface contamination, experimentally measured adhesion forces may be much lower than expected from surface energy consideration.

2.2.1 Elastic Behavior of Solids

Solids deform under an external force. Thus, to calculate adhesive forces between solid bodies it is required to consider their deformation as well.
The stress acting on a material is defined as force per cross-sectional area:

$$\sigma = \frac{F}{A} \tag{2.34}$$

which has the unite of Pa = N/m^2. The material will be deformed due to the stress applied to it. Strain is the relative elongation of the material:

$$\varepsilon_x = \frac{\Delta L_x}{L_x} \tag{2.35}$$

L_x, is the length of the object in x-direction and ΔL_x is the length change in x-direction due to the stress. A stretch of material leads to a positive strain, while compression leads to a negative strain.
The general Hooke's law relates strains and stress to each other for small strains:

$$\sigma_{ij} = C_{ijkl}\varepsilon_{kl} \quad \text{with} \quad i,j,k,l = 1,2,3 \tag{2.36}$$

where σ_{ij} and ε_{kli} are the stress and strain tensor respectively. C_{ijkl} is the fourth-order stiffness tensor. As a simple example for an isotropic elastic material a strain ε_x in x-direction is due to a stress which is applied only in x-direction, Thus the Hooke's law describing an isotropic material is:

$$\sigma_x = E\varepsilon_x \tag{2.37}$$

where E is Young's modulus of the material.
The linear relation between stress and strain is only valid for small deformations, which for most materials means $\varepsilon < 1\%$. It is called the linear elastic regime of the material. If a higher stress is applied it leads to plastic deformation or material failure.
In Figure 2.16, a stress-strain curve showing typical behaviour of many metals is presented.

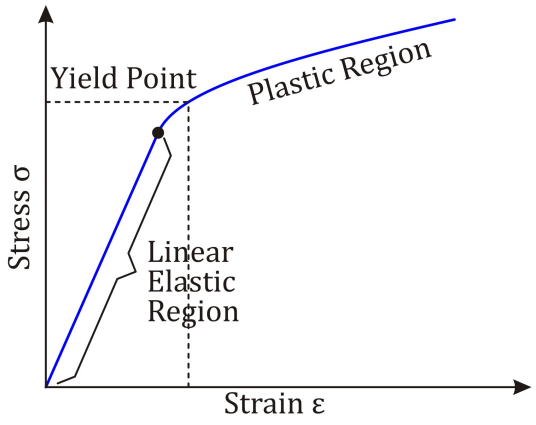

Figure 2.16: Schematic illustration of a stress-strain curve typical for many metals [77].

For small stresses and strains, the material behaves linear elastic up to the yield point, where plastic deformation of the material sets in. Within the plastic region, the relation between stress and strain is no longer linear.

2.2.2 Possion Effect

Many materials, when stretched in one direction, will contract in the direction perpendicular to the stretching direction. This phenomena is called Possion effect (Figure 2.17).

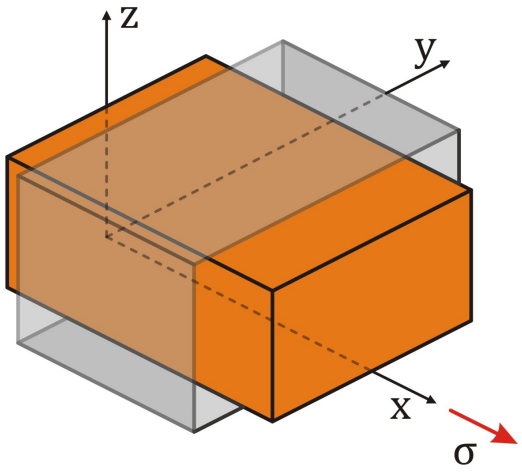

Figure 2.17: Scheme illustrating the Poisson effect: Contraction in y- and z-directions, when stressed in x-direction.

The amount of contraction is identified by the poisson's ratio ν which has typically a value between 0.2 and 0.5. For instance, if a material stretched in x-direction, the contractions in y- and z-direction are

$$\varepsilon_y = \varepsilon_z = -\nu\varepsilon_x \tag{2.38}$$

2.3 Contact Models

In order to calculate adhesion forces between two bodies precisely, it is essential to take the surface deformation of the concerned bodies into account. The surface deformation depends on the contact geometry of solids. There are several models which consider the finite elasticity of the contacting solids.

2.3.1 Hertz Model

The problem of the elastic contact between two spheres and also between a sphere and a planar surface was solved for the first time by Heinrich Hertz, in 1882 [78]. The main assumptions in his model are:

- Surfaces are continuous, smooth and elastic.
- Strains are small, within the elastic limit.
- Contact radius is small compared to the sphere radii.
- Frictionless contact.
- No tensile stress within the area of contact.
- No surface forces between the spheres.

For the sphere-sphere geometry with an external load $F_{external}$ and the contact radius a, he derived an equation

$$a^3 = \frac{3R^*}{4E^*} \cdot F_{external} \tag{2.39}$$

where R^* is the reduced radius and E^*, the reduced Young's modulus , which are defined as

$$\frac{1}{R^*} = \frac{1}{R_1} + \frac{1}{R_2} \tag{2.40}$$

$$\frac{1}{E^*} = \frac{1-\nu_1^2}{E_1} + \frac{1-\nu_2^2}{E_2} \tag{2.41}$$

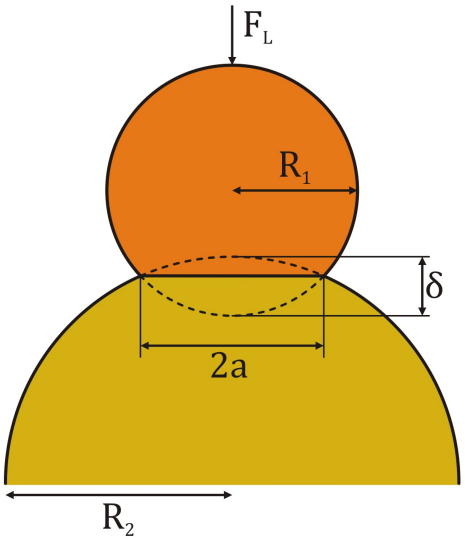

Figure 2.18: Two elastic particles in contact according to Hertz model.

According to Equation 2.39, the contact area πa^2 of the spheres changes due to the applied external load.
The indentation, δ, can be determined from the contact radius

$$\delta = \frac{a^2}{R^*} \tag{2.42}$$

As a consequence, the relation between the force and the indentation is

$$F_{external} = \frac{4}{3} E^* \sqrt{R^*} \cdot \delta^{3/2} \tag{2.43}$$

This implies that the contact does not act as a linear spring because the contact area increases with the applied load. In other words, the contact stiffness $dF_{external}/d\delta = 2E^*a$ increases.
For a rigid sphere with radius R_P, which indents an elastic half-space ($R \to \infty$), Equations 2.40 and 2.41 lead to

$$R^* = R_P \tag{2.44}$$

$$E^* = \frac{E_1}{1 - \nu_1^2} \tag{2.45}$$

The vertical displacement $\Delta z(r)$ of the half-space is shown schematically in Figure 2.19.

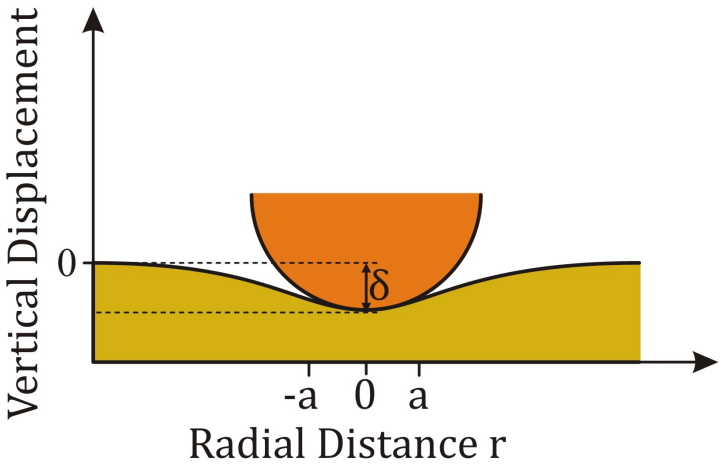

Figure 2.19: Contact between a rigid sphere and an elastic half-space.

According to Equation 2.39, in absence of an external force ($F_{external} = 0$), since no surface forces are considered a point-like contact forms.

In the Hertz model the contact radius a is supposed to be much smaller than the sphere radius $a \ll R$. The indentation of a rigid sphere into an elastic surface without this approximation was studied by Sneddon [79] and Ting [80].

2.3.2 JKR Model

When two surfaces are in contact without an external force, due to the attractive surface forces there is adhesion between them. In the Hertz model surface forces are not considered and when two surfaces detach from each other, they sperate at the point that the indentation δ and the contact radius a are zero . Later on Johnson, Kendall and Roberts extended his theory in 1971, taking into account the adhesive forces between surfaces inside the contact area, which is known as the JKR theory [81].
The JKR theory is based on the balance between the adhesion energy and the stored elastic deformation energy of spheres. Taking into account the adhesive forces leads to enhancement of the indentation and the contact radius compared to the Hertz model for a given applied load. Thus, a characteristic neck forms at the edge of the contact zone, which was not the case in Hertz model (Figure 2.20). The contact radius in equilibrium

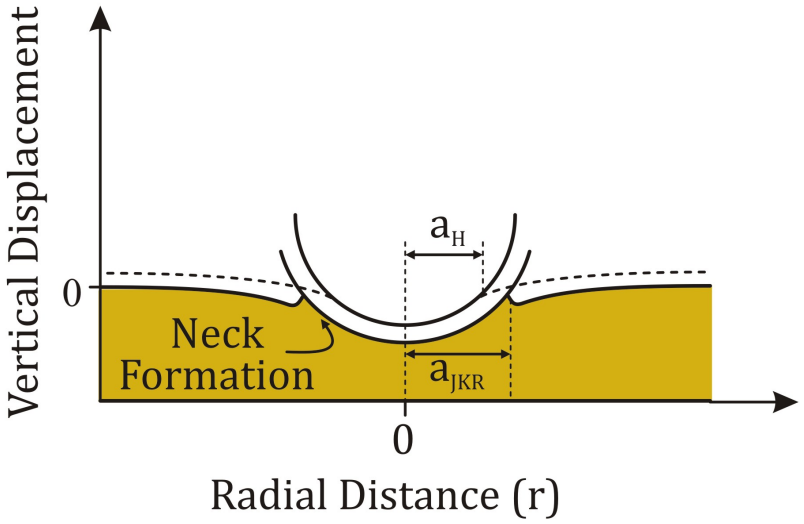

Figure 2.20: Contact between a rigid sphere and an elastic half-space in the JKR model (solid line) compared to the Hertz model (dashed line). In JKR model, due to adhesive forces in the contact zone, a neck forms.

for the JKR model is given by:

$$a^3 = \frac{3}{4}\frac{R^*}{E^*}\left(F_{external} + 3\pi w_{adh}R^* + \sqrt{6\pi w_{adh}R^*F_{external} + (3\pi w_{adh}R^*)^2}\right) \tag{2.46}$$

Where, the first term is identical to the Hertzian contact radius, the second and third terms are due to the adhesive forces that enhance the contact radius compared to cohesionless case (Hertz model).
In absence of external load ($F_{external} = 0$), the contact radius is:

$$a_0 = \left(\frac{9\pi w_{adh}R^{*2}}{2E^*}\right)^{\frac{1}{3}} \tag{2.47}$$

The adhesion force is:

$$F_{adh} = -\frac{3}{2}\pi w_{adh}R^* \tag{2.48}$$

and indentation in JKR model, which corresponds to the height of the neck is:

$$\delta_{min} = -\left(\frac{\pi^2 w_{adh}^2 R^*}{\frac{64}{3}E^{*2}}\right)^{1/3} \tag{2.49}$$

The adhesion force is independent of the elasticity of the materials. This is due to two opposing effects. In a hard material the deformation of the solid is small. As a consequence, the contact area and the total attractive surface energy are small as well, but also the repulsive elastic component is small.
For soft materials deformation and contact area are large but also the repulsive elastic term and the attractive surface energy term. Both effects compensate each other.
The JKR theory uses the assumption that surface forces are acting only within the contact area. However, in reality, surface forces are active also outside of direct contact. Therefore, with the JKR model adhesion force can only be predicted realistically for soft materials with large sphere radii.

2.3.3 DMT Model

The DMT theory describing the adhesive contact between two spheres or a sphere and a plane was developed by Derjaguin, Muller and Toporov soon after the JKR model [82]. They assumed that the stresses and the deformations are given by Hertz model within the contact and considered the attractive forces only in an annular zone outside the contact area (Figure 2.21).

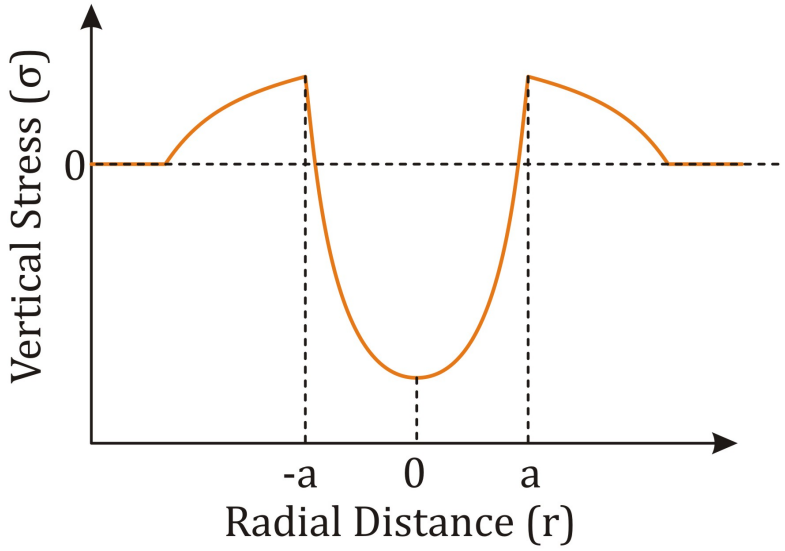

Figure 2.21: Stress distribution for the DMT model. Within the contact area, the stress distribution is that of a Hertzian contact. Outside the contact area, surface forces lead to a tensile stress.

They assumed that the surface forces do not have any contribution to deformation of the surfaces outside the contact zone. Therefore the surface profile in DMT model is the

same as Hertz model. The pull-off in the DMT theory happens at zero contact radius and the adhesion force is given by:

$$F_{adh} = -2\pi w_{adh} R^* \tag{2.50}$$

At the zero external load ($F_{external} = 0$), in the case of spheres of the same material, the contact radius is given by

$$a_0 = \left(\frac{3\pi w_{adh} R^{*2}}{2E^*} \right)^{\frac{1}{3}} \tag{2.51}$$

which differs from the equilibrium contact radius in JKR theory (Equation 2.47).
The DMT model is valid for hard spheres with small radii and more long-ranged forces due to the fact that surface forces inside the contact are not taken into account.
The JKR / DMT do not take into account surface roughness. Furthermore, real contact radii on rough surfaces will be smaller than expected by JKR/DMT since the radii of the surface asperities can become dominating (which are much smaller than the sphere radius).

2.4 Hydrodynamic Forces

Many applications in food science, paper making, mineral precessing, involve colloidal dispersions or emulsions. In all these cases the interacting interfaces are not stationary but move relative to each other. Thus, hydrodynamic forces can be significant and sometimes even dominant.
Hydrodynamics are governed by Navier-Stockes equation. This partial differential equation can be solved analytically only for a few simple cases. In order to understand the hydrodynamic force, it is necessary to briefly introduce the fundamental terms and equations describing hydrodynamic interaction between fluid boundaries.

2.4.1 The Navier-Stockes Equation

The shear force required to slide one plate over another parallel plate at a distance Δz across a fluid (Figure 2.22) is given by

$$\frac{F}{A} = \eta \frac{\Delta \nu}{\Delta z} \tag{2.52}$$

Here, A is the area of the plates, $\Delta \nu$ is the velocity difference tangential to the orientation of the plate, η is the viscosity of the fluid, and Δz is the distance between the plates.

Equation 2.52 is only valid for laminar flow.

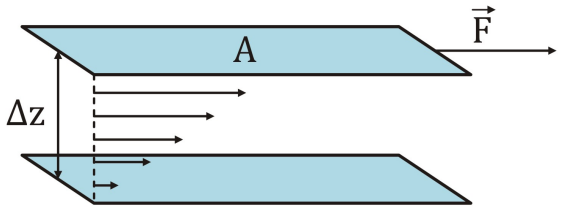

Figure 2.22: The force required to slide a plane over another parallel plane across a fluid.

The fluid is called *Newtonian fluid*, when η does not change with the shear rate.
Shear rate is the rate at which a progressive shearing deformation is applied to some material. The shear rate for a fluid flowing between two parallel plates, one moving at a constant speed and the other one stationary, is defined by

$$\dot{\gamma} = \frac{v}{h} \tag{2.53}$$

where, $\dot{\gamma}$ is the shear rate, v is the velocity of the moving plate and, h is the distance between the two parallel plates.
Any motion of a particle in a Newtonian fluid can be described in terms of the *Navier-Stokes equation*. For tiny amount of the liquid with the volume $\mathrm{d}V = \mathrm{d}x \cdot \mathrm{d}y \cdot \mathrm{d}z$, the flow velocity $\mathrm{d}\nu$, and the mass $\mathrm{d}m$, the flow of the liquid can be described by Newton's equation of motion ($F = m \cdot \mathrm{d}\nu/\mathrm{d}t$) where several forces have to be taken into account [68]. Viscous force, caused by gradients in the shear stress of the fluid has the first contribution to the forces given by

$$F_{\mathrm{Viscous}} = \eta \nabla^2 \vec{\nu} \cdot \mathrm{dV} \tag{2.54}$$

where, η is the viscosity of the fluid and $\vec{\nu}$ is the flow vector.
Second force is caused by a possible pressure gradient which leads to the force given by

$$F_{\mathrm{Pressure}} = -\left(\nabla P\right) \mathrm{dV} \tag{2.55}$$

Furthermore, external forces may contribute. For instance, an external electric field causes an electrostatic force on the ions in solution described by

$$F_{\mathrm{Electrostatic}} = \rho_e \vec{E} \mathrm{dV} \tag{2.56}$$

Where ρ_e is the ion density caused by dissolved ions and $\vec{E}$ is the electric field. Combining all contributing forces into Newton's equation of motion leads to Navier-Stockes equation:

$$\mathrm{d}m\frac{\mathrm{d}\vec{\nu}}{\mathrm{d}t} = \left(\eta\nabla^2\vec{\nu} - \nabla P + \rho_e\vec{E}\right)\mathrm{dV} \tag{2.57}$$

If the fluid velocity is constant the equation simplifies to

$$\left(\eta\nabla^2\vec{\nu} - \nabla P + \rho_e\vec{E}\right)\mathrm{dV} = 0 \tag{2.58}$$

For incompressible liquids, for which the mass density ρ is constant over space and time, the Navier-Stokes equation is complemented by the continuity equation. The first derivative of the velocity in all directions is constant:

$$\nabla\cdot\vec{\nu} = \left(\frac{\partial\nu_x}{\partial x} + \frac{\partial\nu_y}{\partial y} + \frac{\partial\nu_z}{\partial z}\right) = 0 \tag{2.59}$$

2.4.2 Laminar and Turbulent Flow

The liquid flow could be either laminar or turbulent. In all above calculations, the laminar flow is considered and not turbulent flow. As in laminar flow, the different layers do not mix due to the hydrodynamic flow and mixing could happen only by diffusion. When the inertial components of the flow are low compared to frictional effects, laminar flow dominates. If the typical velocity is given as ν and L is the length scale over which the velocity changes, the inertial and frictional components are approximated by:

$$F_{inertial} = \rho(\overrightarrow{\nu}\cdot\nabla)\overrightarrow{\nu} \approx \frac{\rho\overrightarrow{\nu^2}}{L} \tag{2.60}$$

$$F_{frictional} = \eta\nabla^2\nu \approx \frac{\eta\overrightarrow{\nu}}{L} \tag{2.61}$$

The ratio between both force densities is *Reynolds number*:

$$Re = \frac{\rho\overrightarrow{\nu}L}{\eta} \tag{2.62}$$

Laminar flow occurs for small Reynolds numbers, $Re \ll 1$ and turbulence dominates for $Re \gg 1$.

2.4.3 The Hydrodynamic Boundary Conditions

In fluid mechanics, the *Navier-Stokes equations* are used to explain flows in which the fluid can be considered as a continuous medium. To solve the Navier-Stokes equation, boundary conditions need to be set. When liquid flows over a solid, two scenarios are possible: either the liquid at the surface is moving at finite speed (slip boundary condition), or the relative fluid velocity at the solid-liquid interface is zero (no-slip boundary condition). The *no-slip boundary condition* means that the liquid layer in contact with the surface is bound to it and does not move (Figure 2.23).

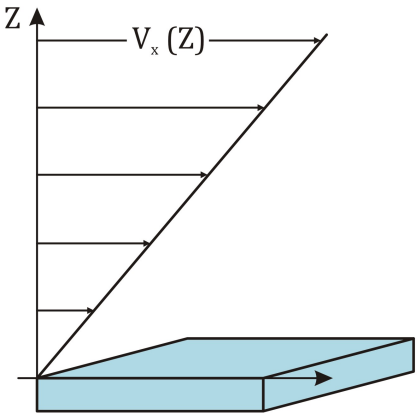

Figure 2.23: Schematic illustration of hydrodynamic no slip boundary conditions at a solid-fluid interface.

The *slip boundary condition* means that the liquid slips over the surface. The amount of slip can be characterized by the so-called slip-length b. It can be derived from the velocity profile, as the distance behind the surface at which the liquid velocity extrapolates to zero. If x is the direction of the flow, z is directed normal to the surface then the slip velocity on the surface ν_s is given by

$$\nu_s = b \cdot \frac{\mathrm{d}\nu_x}{\mathrm{d}y}, \tag{2.63}$$

where $(\mathrm{d}\nu_x/\mathrm{d}y)$ is local shear rate at the surface, and b is slip length (Figure 2.24).

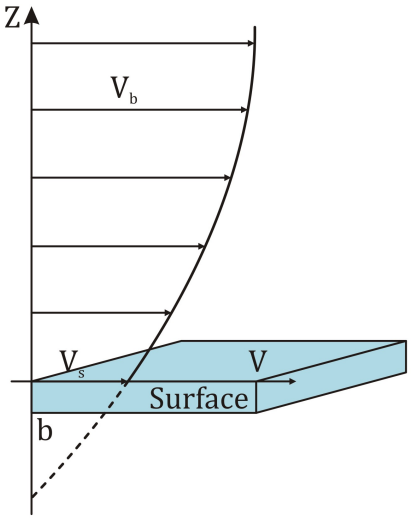

Figure 2.24: Schematic illustration of the shear force near the surface with the velocity ν_b. There is a finite velocity of ν_s on the surface and the slip length b extrapolates into the surface.

The *slip boundary condition* was introduced by Brochard [83]. The surface slip has been studied theoretically [83–87], in computer simulations [88–91] and experiments [92–113].

2.4.4 Hydrodynamic Force Between a Sphere and a Planar Surface

Using all the previously derived equations, calculating hydrodynamic force acting on a sphere approaching a planar surface is possible [114, 115]. However two assumptions should be made. First of all, the radius of the approaching sphere should be sufficiently small, in order to have Reynolds number less than 1. Second, the velocity of the liquid at the surface has to be zero (non-slip boundary condition).

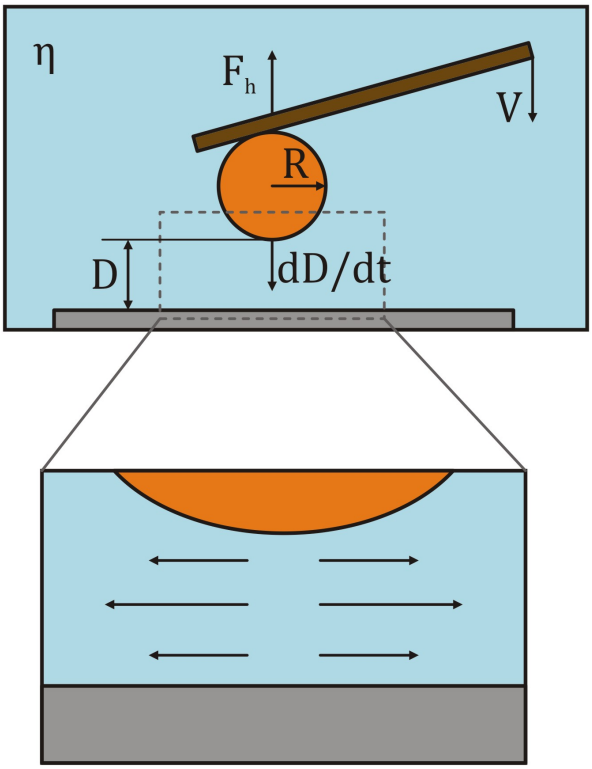

Figure 2.25: Schematic illustration of a sphere approaching a planar surface.

Then the creeping flow is ensured, i.e. inertia effects can be neglected compared to the viscous resistance. Using the equations mentioned above and taking into account these two assumptions, the hydrodynamic force, F_h, for a sphere approaching a planar surface in fluid is given by

$$F_h = -\frac{6\pi\eta R^2}{D} \cdot \frac{\mathrm{d}D}{\mathrm{d}t}. \tag{2.64}$$

Here, η is the liquid viscosity, R is the radius of the approaching sphere, D the distance between a sphere and the surface and, $(\mathrm{d}D/\mathrm{d}t)$ is the approaching velocity of the sphere. The negative sign indicates that the force is directed opposite to the velocity direction. The fluid is drained out from the gap between the surface and the lower part of the sphere (Figure 2.25).
The hydrodynamic force curves are plotted by solving the equation of motion for a sphere attached to a cantilever, moving towards - or retracting from - a plane in a fluid:

$$F_h + F_{vdW} + F_c + F_{drag} = m \cdot \frac{\mathrm{d}^2 D}{\mathrm{d}t^2}. \tag{2.65}$$

F_{vdW} is the van der Waals attraction, F_c is the restoring force of the cantilever, F_{drag} is the hydrodynamic drag on the cantilever, and $m \cdot \mathrm{d}^2D/\mathrm{d}t^2$ takes into account the acceleration of the colloidal probe with the mass of m. Since the system (colloidal probe) is characterized by small Reynolds number ($Re \ll 1$) in Equation 2.65, the acceleration term is negligible. Solving Equation 2.65 results in two equations of motion, for approach and retract separately which are given by

$$\frac{-6\pi\eta R^2}{D} \cdot \frac{\mathrm{d}D}{\mathrm{d}t} f^* - \frac{A_H R}{6D^2} + F_{drag} = \left\{ \begin{array}{ll} k_c \left(D - D_a + \nu_0 t\right), & \text{for } 0 < t \leq t_a \\ k_c \left(D - D_r - \nu_0 t\right), & \text{for } t_a < t \leq t_r \end{array} \right\} \tag{2.66}$$

Here, D_a and D_r are the initial separations of the sphere and the plane for approach and retract part, respectively. t_a and t_r are the approach and retract times. k_c is the spring constant of the cantilever, A_H is the Hamaker constant but the van der Waals interaction barely contributes to the overall force. ν_0 is the approaching velocity of the sphere. The initial conditions are:

$$\left\{ \begin{array}{ll} D|_{t=0} = D_a, & \text{for } 0 < t \leq t_a \\ D|_{t=t_a} = D_r = 0, & \text{for } t_a < t \leq t_r \end{array} \right\} \tag{2.67}$$

The hydrodynamic contributions in Equation 2.66 is given by

$$F_h = -\frac{6\pi\eta R^2}{D} \cdot \frac{\mathrm{dD}}{\mathrm{dt}} \cdot f^* \tag{2.68}$$

Here, b is the slip length and f^* is correction factor which was introduced by Vinogradova [111] and is given by

$$f^* = \frac{D}{3b}\left[(1 + \frac{D}{6b}) \cdot ln(1 + \frac{D}{6b}) - 1)\right]. \tag{2.69}$$

2.5 Friction Forces

Friction plays an important role in daily humans and animals life. Friction is the force between interacting surfaces that resists or hinders their relative movement. Wear is the progressive loss of material from a body caused by contact and relative movement of a contacting solid, liquid or gas. Lubrication reduces friction between surfaces and minimizes wear. The research field of friction, lubrication and wear is called "tribology". Although, friction is important in everyday life, there is no precise macroscopic theory of friction that allows us to predict frictional forces between two given bodies. Recently, the development of new experimental methods such as surface force apparatus, and atomic

force microscope have given scientists new ways to study friction and lubrication at the molecular scale [68].
A solid body placed on a surface will stay in its position unless an external force is applied on it to overcome its inertia and the friction force between the body and the surface, with which it is in contact.
It is useful to understand the difference between static and dynamic friction. Dynamic friction or kinetic friction is the mechanical force between sliding or rolling surfaces that resists the movement of the moving body. Static friction is the friction that must be overcome in order to start movement between two bodies which are initially at rest.
The static friction, f_S is given by

$$f_s = \mu_S \cdot F_N, \tag{2.70}$$

where μ_S is the static friction coefficient and F_N is the normal load.
In 1699, *Guillaume Amontons* found that the frictional force does not depend on apparent contact area. For instance, when two applied loads F_L^1 and F_L^2 are equal, the frictional force is equal as well (Figure 2.26).

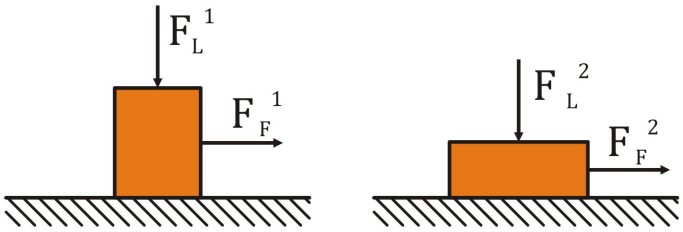

Figure 2.26: Amontons's law: The frictional force is independent from the contact area.

$$\text{If} \quad F_L^1 = F_L^2 \quad \text{then} \quad F_F^1 = F_F^2. \tag{2.71}$$

In other words, μ the coefficient of friction is defined by

$$F_F = \mu F_L. \tag{2.72}$$

According to Equation 2.72, μ should be constant and independent of contact area.
Kinetic friction occurs between surfaces which are moving relative to each other as shown in Figure 2.27 [67]. For most materials, the kinetic coefficient μ_k is smaller than static coefficient μ_S.

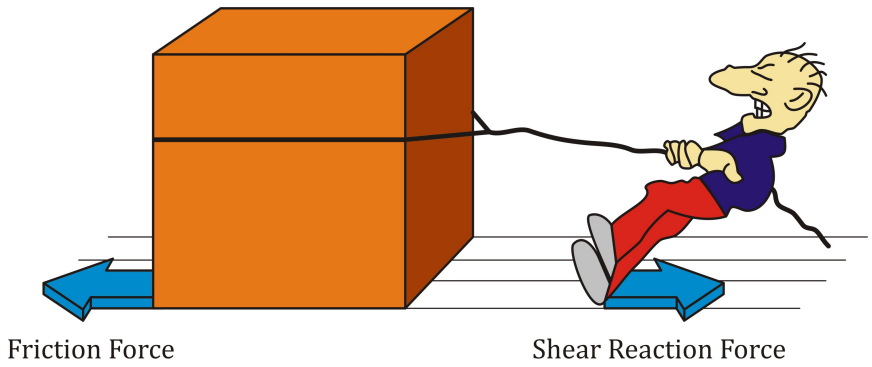

Figure 2.27: Kinetic friction: Two surfaces which are moving relative to each other.

2.5.1 Friction and Adhesion

Increasing adhesion between the two solid surfaces makes the friction stronger. The adhesion force F_{adh} can be considered by adding it to the normal load in Equation 2.72.

$$F_F = \mu(F_L + F_{adh}) \tag{2.73}$$

For macroscopic objects the adhesion force is usually negligible compared to the normal load, while for microscopic bodies the adhesion force can be dominant.

3 Materials and Methods

In this chapter tools to measure adhesion and friction is discussed. The fundamentals of scanning electron microscope, AFM force spectroscopy, cantilever calibration method, and colloidal probe techniques are presented.
In this work, samples are divided into two classes: hard and soft surfaces. The hard substrates were used either as a reference for adhesion measurement on soft surfaces or for measuring the sensitivity of cantilevers.

3.1 Substrates Preparation

In this section, preparation of different samples, based on type of the experiments are described.

3.1.1 Hard Surface: Silicon Wafer

In all experiments in this thesis, as a hard substrate, naturally oxidized silicon wafers were used. Small pieces (4×4 cm) of the wafers were cleaned by putting them in a Argon plasma chamber (PDC-001, Harrick Scientific Corporation, USA) for 10 minutes. The samples were used for measurement immediately after cleaning.

3.1.2 Soft Surface: PDMS

In all experiments in this thesis, as a soft substrate, the polymer polydimethylsiloxane (PDMS) was used. PDMS (Sylgrad Elastomer 184, Dow Corning Corporation, Midland, MI) was mixed properly with a cross linker agent with 10 : 1 ratio and the resulting mixture was degassed in vacuum oven at room temperature.

PDMS Film Preparation For Hydrodynamic Force Measurements

For the hydrodynamic force measurements between a sphere and a soft, elastic surface, which will be described in *chapter 4*, the soft substrates were prepared as the following: The PDMS samples (Dow Sylgard 184) were prepared by mixing at a 10:1 ratio of elastomer to curing agent, then degassing in a vacuum oven at room temperature. To

obtain flat surfaces, 3 mL of the freshly prepared PDMS mixture was poured onto a clean silicon wafer and then cured it in an oven at 90 °C for 1 hour. The cured film was removed gently from the silicon substrate and the side facing the silicon wafer was used in the measurements.

Hexagonally Patterned Surface Preparation For Capillary Force Measurements

The hexagonally patterned soft samples for capillary force measurement described in *chapter 5* is prepared as the following.
Elastic adhesive model for this work was made by cross-linking liquid Polydimethylsiloxane (PDMS). For making smooth, elastic samples, PDMS precursor liquid was mixed with the curing agent (10 : 1 by weight) properly. After mixing, 3 ml of this mixture is applied on a hexagonally patterned mask (Figure 3.1).

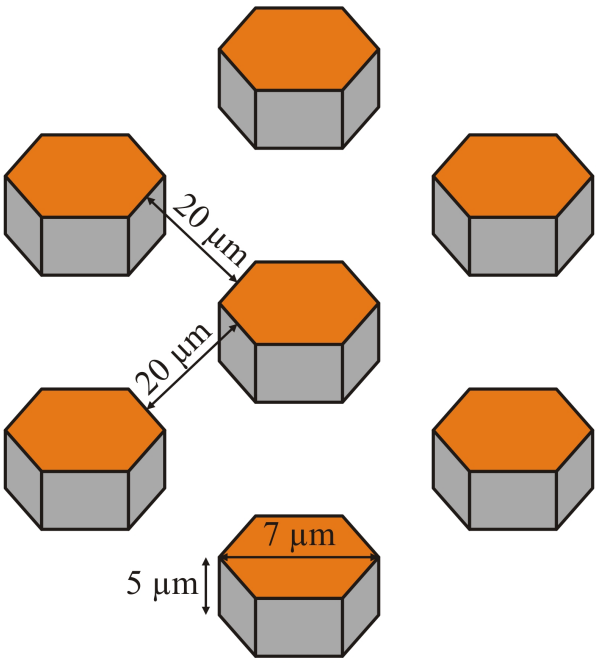

Figure 3.1: (a) Schematic illustration of hexagonally patterned mask.

Hexagonal holes in the mask have diameter, D = 7 µm and height h = 5 µm. These holes are separated by a distance, d = 20 µm . The applied mixture on the patterned mask is cured in an oven at 90 °C for 1 hour. At the end of this step, we have a Normal shape pillar (Figure 3.2). The total thickness of the sample is 1 mm.

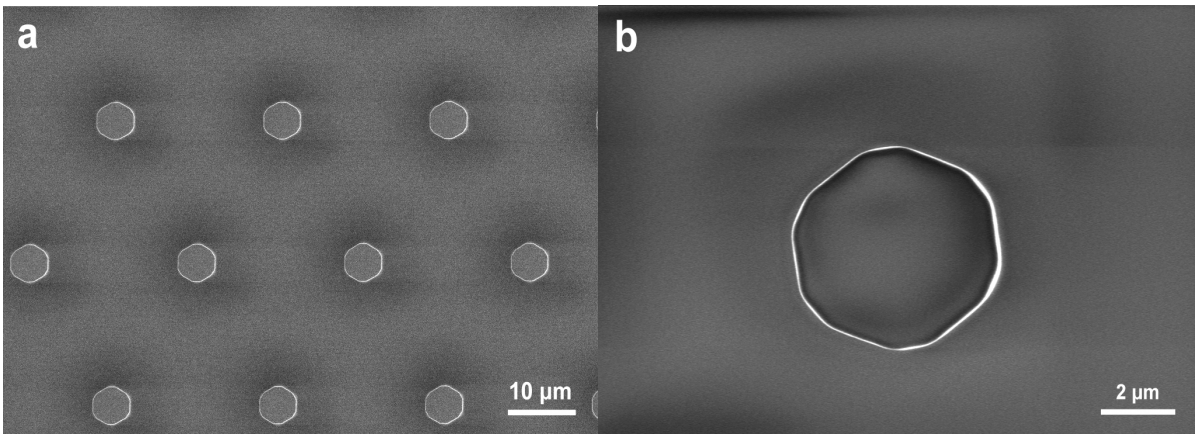

Figure 3.2: SEM images of (a) arrays of Normal shape pillar and (b) a single Normal shape pillar.

T-shape terminated pillars have obtained by inking and printing method. Similar to Normal shape pillar preparation, 10:1 ratio of Sylgard 184 prepolymer and cross linker was mixed, degassed and poured onto the patterned wafer with the hexagonal network and cured. A prepared PDMS pattern with Normal shape hexagonal pillars was inked into the thin liquid PDMS film ($0.6 - 1\,\mu m$). For preparing a thin liquid film, a small droplet of mixed, degassed, Sylgard 184 prepolymer and cross linker (10:1) was poured onto a glass plate. Further by using a film applicator (Erichsen, Hemer, Germany) a thin film was dragged. Inked network hexagonal pillars were pressed against a glass slide and cured for 1 hour at 90 °C. Micro patterned PDMS fields with hexagonal pillars arrays with 7 µm diameter, 5 µm height separated by 20 µm channels were obtained (Figure 3.3).

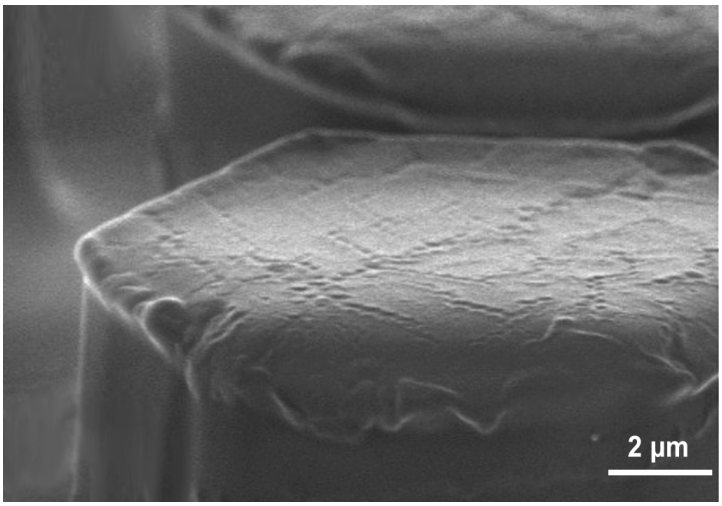

Figure 3.3: SEM image of a T-shape pillar.

Hexagonal pillars with concave cup were fabricated as the following: Sylgard 184 prepolymer and cross linker (ratio 10:1) was mixed and degassed, poured onto a glass Petri dish and precured for 5-6 min at 90 °C. A PDMS mould was pressed against the precured PDMS film and a 125 g weight was applied on the mask and film. The sample was cured in an oven at 90 °C for 55 min. Micro patterned PDMS networks with arrays of hexagonal pillars with 7 µm diameter, 5 µm heights and by separating channel with 20 µm wide were obtained (Figure 3.4) [48]. Since the mechanical properties of polymers may change over time, fresh samples were used for every adhesion measurement. Capillary force measurements were performed by using AFM (Dimension 3100, USA).

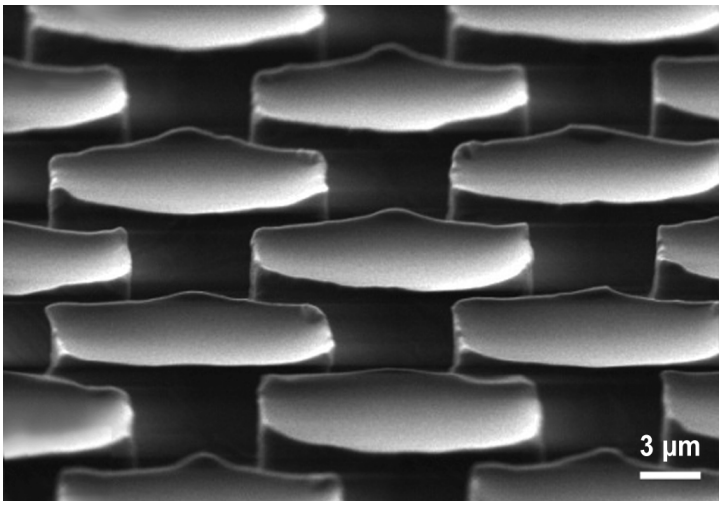

Figure 3.4: SEM image of arrays of concave cup pillars.

Hexagonally-Elongated Patterned Surface Preparation For Friction Force Measurements on Biomimetic Structures

The soft samples for friction force on biomimetic structure project which will be described in *Chapter 6* were prepared as the following: Micropatterns PDMS pillars were prepared by mixing PDMS (Dow Sylgard 184) at a 10:1 ratio of elastomer to curing agent then degassing in a vacuum oven at room temperature. To obtain hexagonal and elongated pillars, 3 ml of the mixture was poured onto the SU-8 patterned wafer with elongated and hexagonal holes and cured at 90 °C in a vacuum oven and then demoulded. Furthermore, the elongated pillars with 1 and 3 µm distance between channels have been obtained as are shown in Figure 3.5.

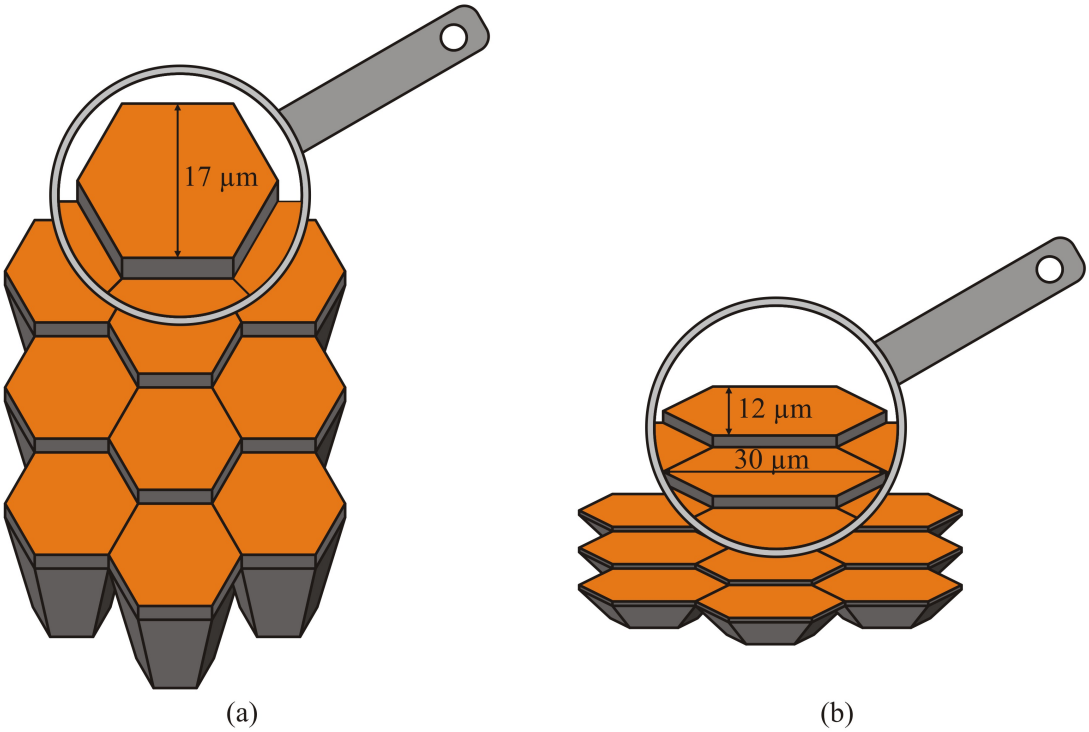

Figure 3.5: Schematic illustration of (a) hexagonal and (b) elongated pillars.

3.1.3 Hydrophilic Samples

Clean silicon wafers are hydrophilic. They are often contaminated with organic surface layers, that render them hydrophobic. The PDMS samples are hydrophobic. In order to make PDMS samples hydrophilic, 10 s, O_2 plasma treatment was applied. Silicon wafers have been cleaned for 10 min by Ar plasma treatment. The properties of O_2 and Ar chambers are:

O_2 Chamber: Oxygen plasma, 80 W, 0.1 mbar, Plasma Activate Statuo 10 USB chamber, Plasma Technology GmbH, Rottenburg, Germany.
Ar Chamber: Argon plasma, PDC-001, 29.6 W, 20 mbar, Harrick Scientific Corporation, USA.

3.2 Scanning Probe Microscopy

Scanning probe microscopy covers many related techniques, which provide topographical information and measurements of surface forces at a fine scale, even down to the level of molecules and groups of atoms. In 1981, the first SPM was developed by invention of *Scanning Tunneling Microscope (STM)* at the IBM Zurich Research Laboratory, Switzerland by Gerd Binnig, Heinrich Rohrer, Christoph Gerber and Edmund Weibel [116]. In the STM, an atomically sharp conductive tip is moved above a conductive sample and the tunneling current is measured. Changes in the sample height lead to changes in the distance between the tip and the sample, and this results in changes in the tunneling current. By keeping the current constant, the height of the tip above the sample is maintained constant. Some years after the advent of SPM, in 1981, Gerd Binnig along with Calvin Quate and Christoph Gerber invented the first Atomic Force Microscopy (AFM) [117]. This technique was used first to obtain topographical information of the surfaces. Nowadays, the AFM is used to study a broad range of surface properties such as viscoelastic, thermal and mechanical properties of surfaces, and various AFM-based instruments have been developed. For instance, Kelvin probe force microscopy (KPFM), Electrostatic Force Microscopy (EFM), Magnetic Force Microscopy (MFM), Friction Force Microscopy (FFM) and the colloidal probe technique have become available. All this instruments are categorized as Scanning Probe Microscopy. The simplest AFM consists of a sharp tip at the end of a flexible cantilever, which is raster scanned across the surface (Figure 3.6). The cantilever is usually made of silicon or silicon nitride which has a tip apex lying in the range of 5-50 nm. In an AFM, the cantilever is brought into close contact with the surface of the sample, then the tip scans across the surface, either by moving the tip or the sample. Any deflection of the cantilever due to the interaction of the tip with the surface is detected by reflection of a laser beam from the cantilever backside onto a photodiode, which is divided into four quadrants. The cantilever can be assumed as a spring with spring constant of k. For a small deflection Δz of the cantilever the force between tip and surface will be given by Hooke's law as

$$F = -k \cdot \Delta z. \tag{3.1}$$

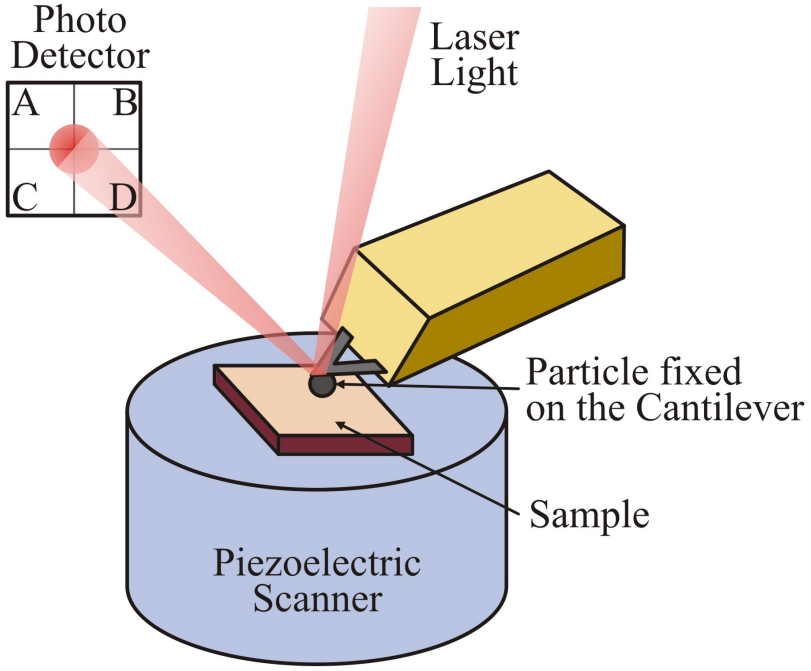

Figure 3.6: Schematic illustration of an atomic force microscope (AFM): The cantilever is brought into contact with the sample surface, and raster-scanned. The sample-surface interaction results in cantilever deflection, which is measured with a laser beam reflected from the cantilever backside onto a photodiode.

3.2.1 Imaging with an Atomic Force Microscope

Depending on the application, the atomic force microscopy can be performed in different operating modes. The basic imaging mode is divided into static (*Contact mode*) or dynamic (*Tapping or Intermittent contact mode*). These modes are classified based on the interaction of the tip with the sample surface. This interaction includes both attractive and repulsive forces, which can be described by the Lennard-Jones potential (Figure 3.7).

$$U_{LennardJones} = [\frac{A}{r^{12}} - \frac{B}{r^{6}}] \tag{3.2}$$

where r is the distance between the tip and the sample, A and B are constants. The term, r^{-12} describes the repulsive forces and arises due to the overlapping of the electron orbits and the r^{-6} term explains the attractive force and arises from sum of various effects such as van der Waals forces. Two different modes in AFM can be classified as the following:

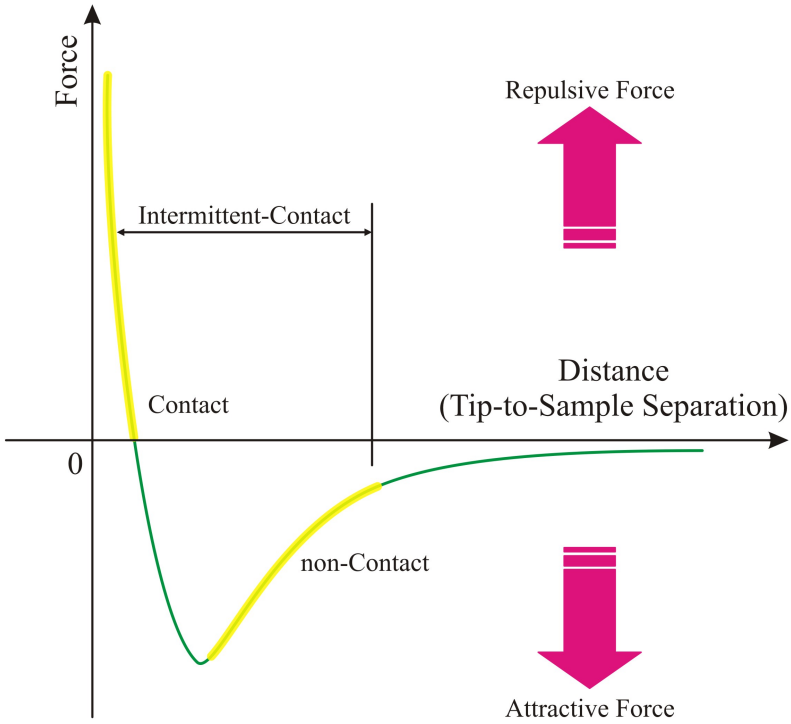

Figure 3.7: Schematic illustration of Lennard-Jones potential describing the tip-sample interaction with distance between tip and sample.

Contact Mode

In contact mode, where the tip is in constant contact with the surface, the tip raster-scans the sample surface line by line. Normally, the force between the tip and the surface is kept constant by a feedback loop that maintains a predefined deflection of the cantilever. This constant deflection value is called *set- point* and is defined by the user. During scanning, topographical differences of the surface cause a change of cantilever deflection, which is detected with photodiode and the feedback loop moves the cantilever in z direction by applying a voltage to the z-piezo-scanner until the force is at the set-point value again. Recording this z-movement while raster scanning the probe across the sample surface, a topographic image of the surface is obtained. However, imaging in contact mode has certain drawbacks. The friction between tip and sample surface, which is caused by lateral movement of the cantilever on the surface, can lead to damage of tip or sample. On soft samples, the tip may indent the surface easily, even with smallest possible load and this leads to tip contamination or surface damage [118]. On a hard substrate, the tip wears off during the scanning leading to errors in the determination of the size of the surface structures due to changes tip radii [119].

Tapping Mode

To avoid wear of the surface or the tip, the dynamic operation mode can be used [120]. In tapping mode (also called intermittent contact mode), the cantilever is oscillated vertically near to its resonant frequency [121] by an additional piezo actuator. When the tip interacts with the surface, the amplitude and the frequency of the oscillation change. Depending on the topography of the sample and interactive forces between the tip and the sample, the cantilever motion can be described as a harmonic oscillator [120].

$$m\ddot{z} + kz + \gamma\dot{z} = F_{ts} + F_0 \cos(\omega t) \tag{3.3}$$

where k and γ are the spring constant and the damping factor of the cantilever, respectively. F_{ts} is the tip-sample interaction force . F_0 and ω are the amplitude and the angular frequency of the driving force, respectively. If no tip-sample interaction is present ($F_{ts} = 0$), Equation 3.3 simplifies to:

$$\ddot{z} + \omega_0^2 z + \frac{\omega_0}{Q}\dot{z} = \frac{F_0}{m}\cos(\omega t) \tag{3.4}$$

where $Q = (\omega_0 m)/\gamma$ is the quality factor, m is the effective mass of the cantilever and $\omega_0 = \sqrt{k/m}$ is the free cantilever resonance frequency. A solution for Equation 3.4 is

$$z(t) = A(\omega)\cos(\omega t + \phi) + z_0 \tag{3.5}$$

where the amplitude $A(\omega)$ and the phase shift $\phi(\omega)$ are given by

$$A(\omega) = \frac{F_0/m}{\sqrt{(\omega_0^2 - \omega^2)^2 + (\omega_0^2\omega^2)/Q^2}} \tag{3.6}$$

$$\phi(\omega) = \arctan\left(\frac{\omega\omega_0/Q}{\omega_0^2 - \omega^2}\right) \tag{3.7}$$

The cantilever resonance frequency will change due to the interaction between the cantilever and the surface.
Topography images can be obtained by two different techniques: by *amplitude modulation* or by *frequency modulation*. In amplitude modulation mode, at a fixed frequency the cantilever is excited while the change in amplitude is measured and compared with value of amplitude set-point that the user has defined. The feedback loop system by applying a voltage to the z-piezo scanner tries to keep the amplitude of the cantilever constant which leads to a change of cantilever height. In frequency modulation mode the

cantilever oscillates with a fixed amplitude while the feedback loop keeps the frequency shift constant.
Different measurements in this thesis have done with different AFMs.
The hydrodynamic experiments (Chapter 4) were performed using an AFM equipped with a liquid cell (Multi Mode Pico force, Veeco, USA) operated in closed-loop scanning mode. The liquid cell components (cantilever holder, O-ring, etc. , (Figure 3.8) were cleaned before experiments in an ultrasonic bath with ethanol for two hours.

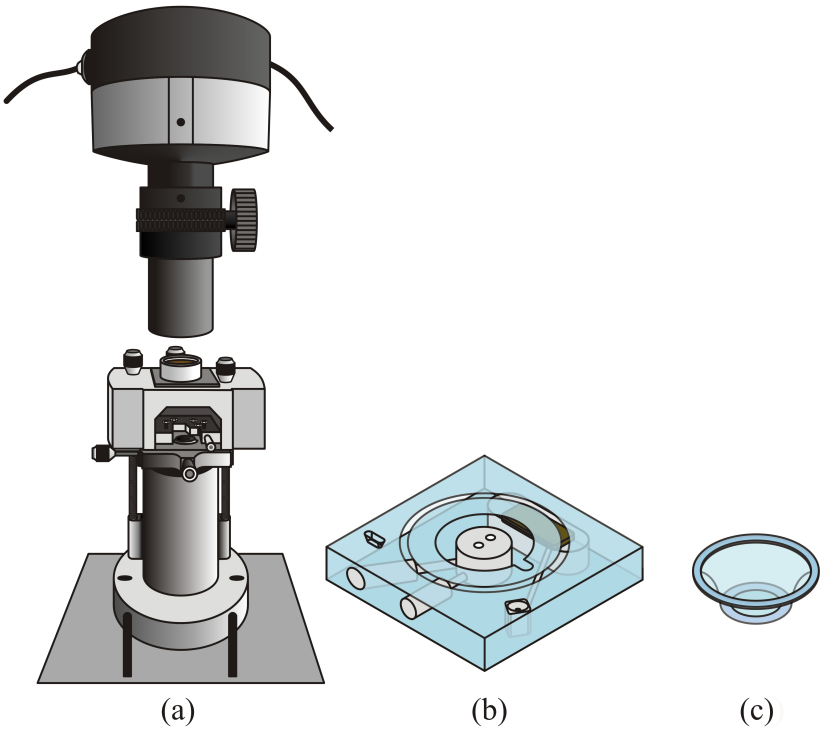

Figure 3.8: (a) Schematic illustration of Pico force AFM, (b) liquid cell and (c) O-ring.

The capillary force (Chapter 5) and friction force (Chapter 6) experiments on micro-pillars were carried out using Dimension 3100, Veeco, USA.

3.2.2 Force Spectroscopy

In addition to the imaging, AFM is a prominent tool to measure surface forces, as well as to analyze the mechanical behaviour of the surface. The principle of force spectroscopy is as the following: Either the sample or the cantilever stays fixed and the other one is moved vertically by the z-piezo translator. During a force spectroscopy measurement cycle, the AFM tip moves towards the sample surface until reaches the surface and the cantilever starts to deflect until a predetermined maximum force is reached. Then

it is again withdrawn from the surface. During approach-retract cycles the cantilever deflection is measured by reflection of a laser beam from the cantilever backside onto a photodiode. The detector signal usually is recorded in volts (V). The output of such a measurement is the amount of the cantilever deflection in volts versus the piezo position (Δz), as described in detail in six steps in Figure 3.9.
First, when the probe is approaching but still far from the surface, no forces are detected between probe and the sample surface (step 1). As the probe approaches further, due to the attractive forces the cantilever bends and if the gradient of the surface forces exceeds the cantilever spring constant, the cantilever will jump into contact (step 2). From the step 'jump into contact' on, if a hard contact between a probe and the surface is assumed, the probe and the sample move in parallel and they are in contact (step 3). The linear regime, where tip and sample are in contact is called *constant compliance*. Usually this is continued until a predefined deflection which corresponds to a predefined maximum load, is reached. Then the retracting cycle starts, the cantilever deflects less and less and finally bends downward due to the adhesive forces between probe and the sample (step 4). When the restoring force of the cantilever exceeds the adhesion force the cantilever pulls off the surface complectly and relaxes to its equilibrium position (step 5). At the end, the adhesion force is obtainable from the force-distance curve (step 6).
To obtain the adhesion force, one needs first to convert recorded voltage to force. To do so, the process described below should be followed: First of all a line is fitted to the part where probe and sample are far from each other and no force detected which is depicted in step 1 in Figure 3.9. This gives us an offset that should be subtracted from the deflection data. The vertical deflection signal can be converted to the force by:

$$F(\mathrm{N}) = \Delta V(\mathrm{V}) \cdot k(\frac{\mathrm{N}}{\mathrm{m}}) \cdot \alpha(\frac{\mathrm{nm}}{\mathrm{V}}), \tag{3.8}$$

where ΔV is the vertical deflection signal in volts, k is the spring constant of the cantilever and α the deflection sensitivity. The deflection sensitivity of the cantilever α, can be determined for each measurement. In the constant compliance region, the deflection of the cantilever is equal to the piezo displacement assuming that tip and sample deformation can be neglected. By fitting a line to that regime and inverting the value, the conversion factor between vertical deflection signal in V and cantilever deflection in nm is obtained.
To obtain the distance between the probe and the surface D, the cantilever deflection δ_C, and sample deformation δ_S, should be subtracted from the piezo position (Z_{Piezo}) as shown in Figure 3.10.

$$D = Z_{Piezo} - (\delta_C + \delta_S) \tag{3.9}$$

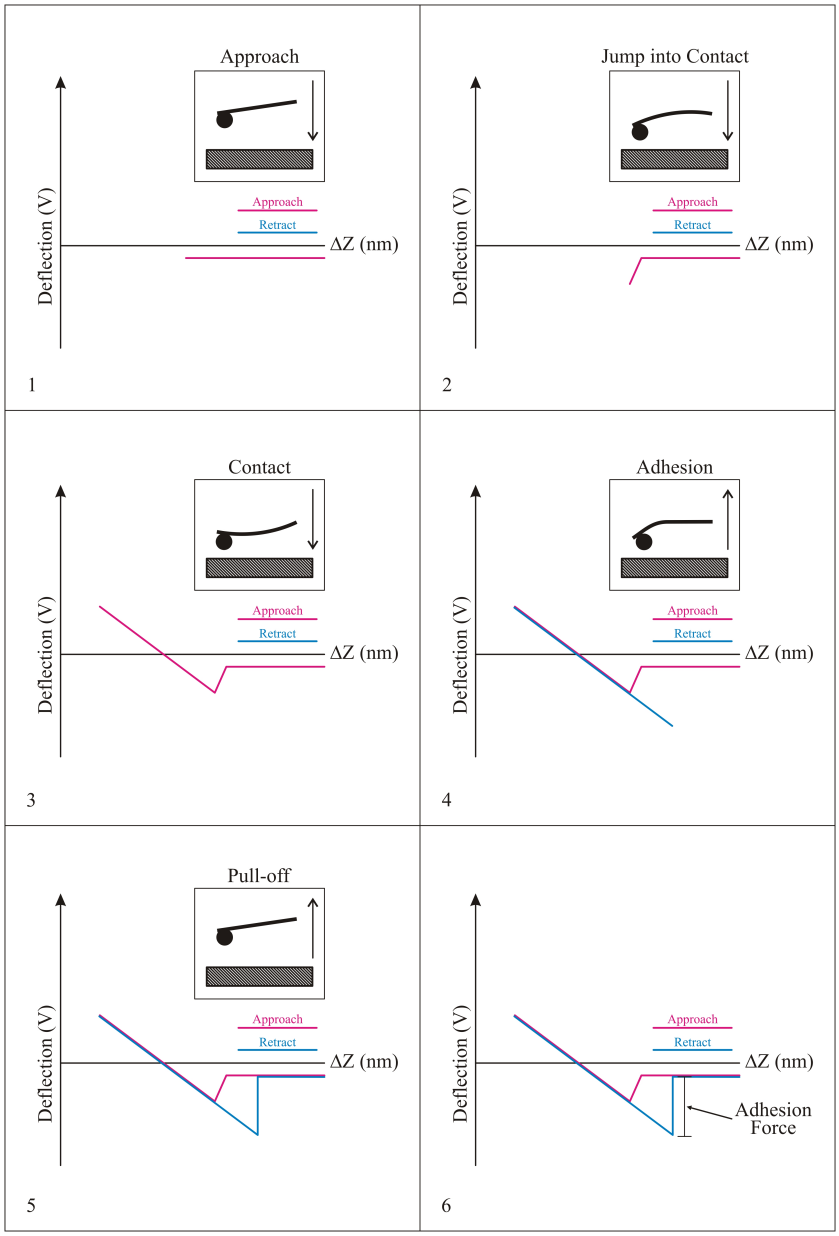

Figure 3.9: Schematic illustration of an AFM force spectroscopy measurement: vertical deflection versus piezo movement curve as the probe is approaching (blue) and retracting (red) from a surface in different steps.(1) Zero force regime, no forces detected while the probe is far from the surface; (2) Jump into contact due to the attractive forces; (3) Probe and surface move up in parallel; (4) Probe and surface move down in parallel and cantilever bends down due to the adhesion; (5) Jump out happens when the bending force of the cantilever exceeds the adhesion between tip and surface; (6) Complete curve showing the adhesion force. The vertical axis represents the detection signal from the detector.

By adding the cantilever deflection to the piezo position, the probe-sample distance is calculated.

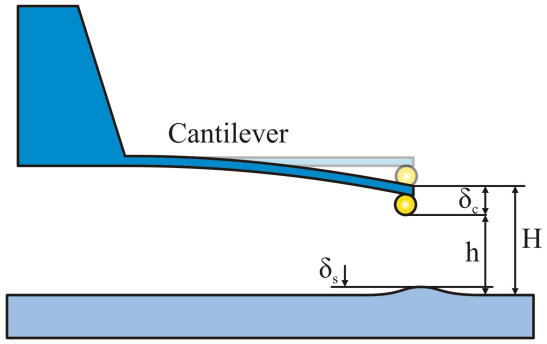

Figure 3.10: Schematic illustration of probe-sample distance force curve.

The result of converting *vertical deflection-piezo displacement* to *force-distance* are depicted in Figure 3.11. From the force-distance curve, the adhesion force F_{adh} is obtainable. Here after the force vs. distance curves will be called force curves.

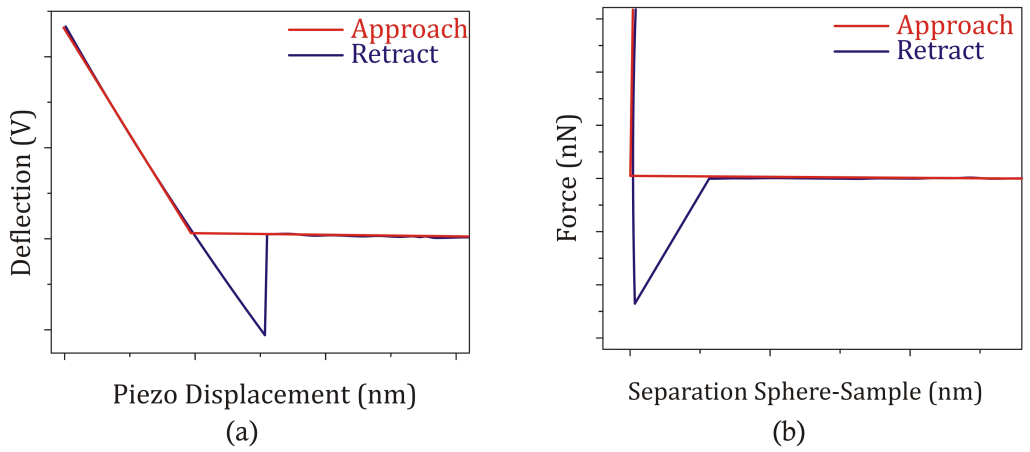

Figure 3.11: Schematic illustration of conversion of (a) vertical deflection-versus-piezo displacement to (b) force-versus-distance on a hard substrate.

3.3 The Colloidal Probe Technique

Force curve results which are obtained from AFM measurement give us the opportunity to study mechanical properties of surfaces, such as elasticity, and to calculate different surface forces in different environments like in air and in liquid. To achieve this aim, the tip geometry needs to be known. One possible method to image the tip geometry is scanning electron microscope (SEM). In case of imaging an AFM tip, charging of the tip and low image resolution are the barriers against obtaining the shape of very sharp tips. As computer simulation shows, the tip and the surface sample change during the force curve measurements when they get into contact and even at low forces the apex of the tip changes dramatically during the first approach [67]. To overcome these problems, the so-called colloidal probe technique was introduced by Ducker [122, 123] and Butt [124] independently. In this method, a single micro-sphere is attached to a tipless cantilever to measure force distance curves [125]. Preparing such a probe is usually done under an optical microscope by means of a micromanipulator. The necessary steps are depicted in Figure 3.12.
A small droplet of glue is deposited onto a clean glass. Then a cantilever is brought into contact with the glue to pick up a small amount of it. Several small (at the order of micron size) glue spots can be deposited onto the glass slide by using a micromanipulator (step 1) to touch the glass surface with the glue-loaded cantilever. Then the used cantilever is exchanged with a new cantilever. By touching one of the small glue spots, the fresh cantilever can be coated with glue at the very end only (step 2). Finally, a micro-sphere is picked up by touching the upper side of it with the glue-coated end of the cantilever (step 3).
Consequently, a probe with defined geometry of a sphere is obtained (step 4). Since it is difficult to properly attach small size particles (below 1 µm size) under an optical microscope to the cantilever, this technique limits the minimum particle size. Colloidal probe technique is a well-established method for exploring particle-wall and particle-particle interactions in air or liquids [122, 124]. For some materials such as glass [101] or polymers [126], sintering of the particles to the cantilever was demonstrated instead of gluing to avoid the risk of probe contamination.

3.3.1 Colloidal Probe For Hydrodynamic Force Measurements

The borosilicate particles with a nominal diameter of 20 µm were glued to the ends of AFM cantilevers (Mikromasch NSC-12 silicon cantilevers, nominal spring constant 4.5 N/m, length 130 µm, width 35 µm, 2 µm thick) with an epoxy glue (Epikote 1004) to make colloidal probes [124]. Actual particle diameters were measured using a scanning electron microscope (SEM) and Image J software (Version 1.46r, National Institutes of

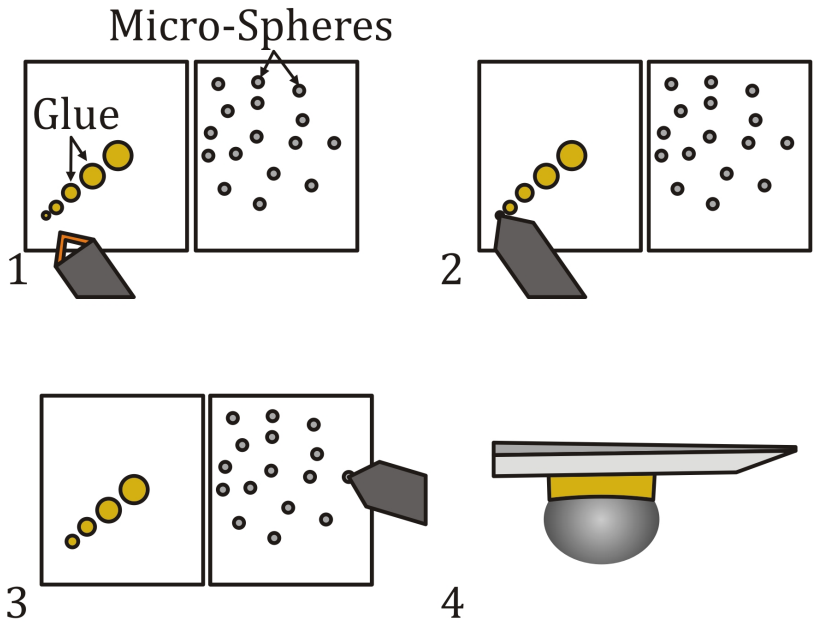

Figure 3.12: Schematic illustration of colloidal probe preparation.

Health, USA).

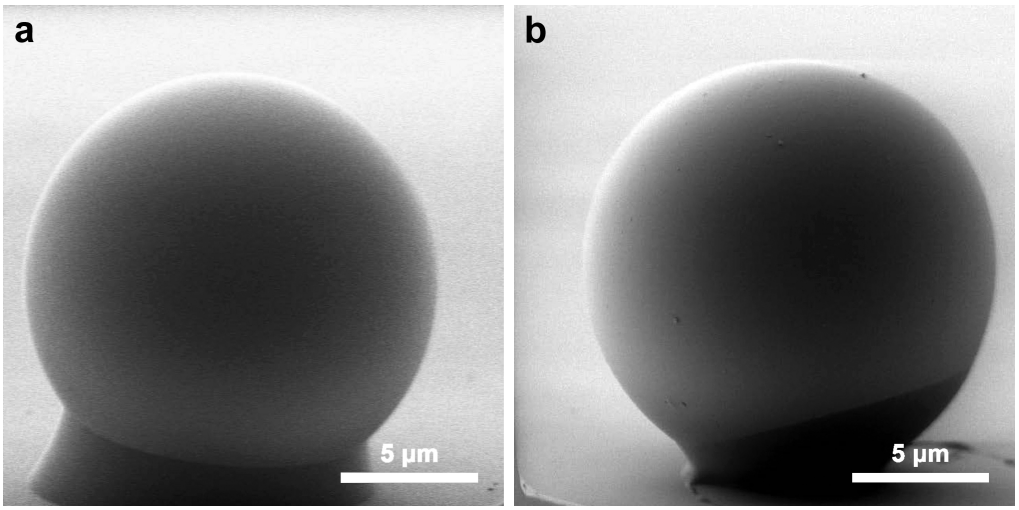

Figure 3.13: The SEM Images of 15.5 µm, colloidal probe (a) before and (b) after the measurement.

The resulting colloidal probe, (Figure 3.13) and the silicon substrates were cleaned with ethanol and by plasma cleaning in argon for ten minutes.

3.3.2 Colloidal Probe For Capillary Force Measurements

10 µm diameter spherical glass particles (Duke Scientific) were glued to the end of tipless cantilevers (Budget sensors, cantilever length 100 µm, width 50 µm, thickness 2.7 µm, spring constant: typical values 40 N/m) by means of a micromanipulator.
The resulting colloidal probes were modified, by cutting off a spherical cap with a Focused Ion Beam (FIB, FEI Nova 600 Nanolab). This modification leads to a flat circular surface with a tilt angle of 12 ° which compensates for the tilt of the cantilever when mounted in the AFM. In Figure 3.14, SEM images of a 10 µm diameter colloidal probe before and after cutting with FIB are shown.

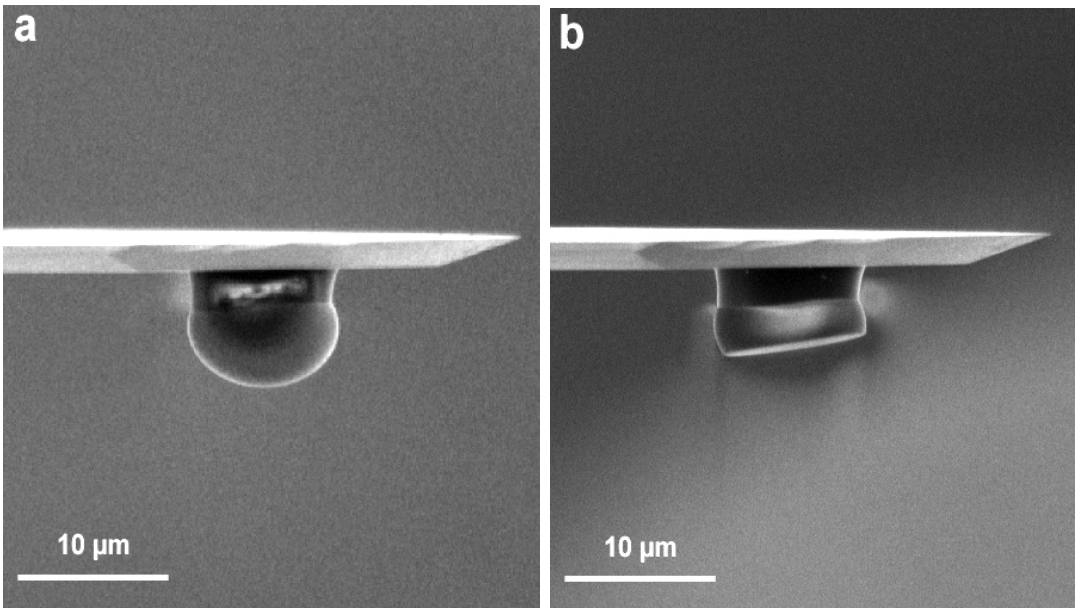

Figure 3.14: The SEM Images of 10 µm, colloidal probe (a) before and (b) after cutting with FIB.

The modified colloidal probe was cleaned in an Argon plasma cleaner for ten minutes before each measurement.

3.3.3 Colloidal Probe For Friction Force Measurements on Biomimetic Structures

Borosilicate particles with nominal diameter of 20 µm were glued to the end of AFM cantilevers (Budget Sensors, part D, Aluminium reflex coating, nominal spring constant: 40 N/m, length 100 µm, width 50 µm, 2.7 µm thick) with an epoxy glue (Epikote 1004) to make colloidal probe. Actual particle diameter was measured using a scanning electron

microscope (SEM) and Image J software (Version 1.46r, National Institutes of Health, USA).

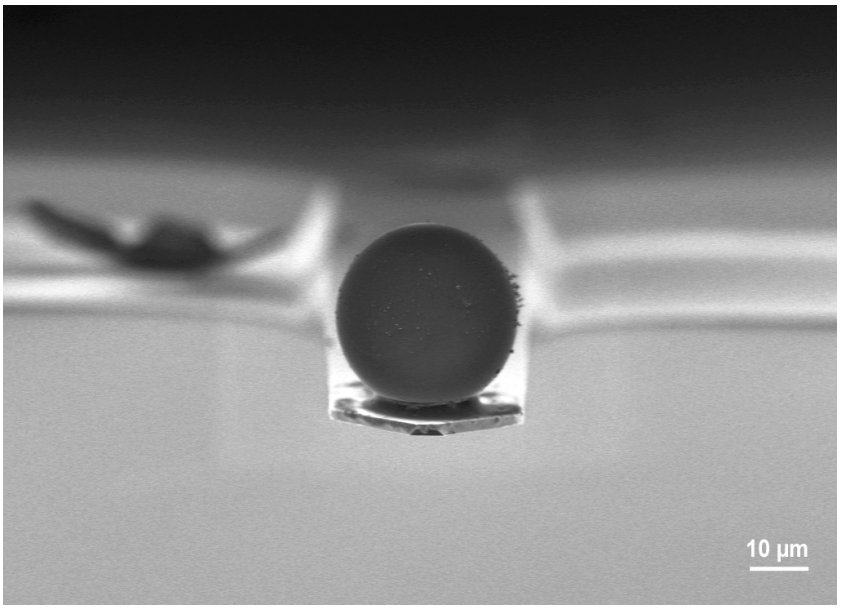

Figure 3.15: The SEM Images of 20 µm diameter colloidal probe.

3.4 Spring Constant Calibration

In order to derive quantitative force versus distance data from the vertical deflection signal, accurate value of the spring constant is necessary. Although the nominal value is provided in the data sheet of the manufacturer, it may deviate significantly from the true spring constant due to variability of the fabrication process. Thus, calibration of spring constant of each cantilever is necessary. In this work *Thermal noise method* has been used to calibrate the spring constant as described below.

Thermal noise method, is a common and reliable method to calibrate the spring constant and is now integrated into the software of many commercial AFMs. This method was introduced by Hutter and Bechhoefer [127] who modeled the cantilever as a harmonic oscillator. They applied the equipartition theorem and related the cantilever's thermally induced vibration to its thermal energy by:

$$\frac{1}{2}k\langle Z_c^2\rangle = \frac{1}{2}k_B T \tag{3.10}$$

where $\langle Z_c^2 \rangle$ is the mean square displacement of the cantilever, k_B the Boltzmann constant and T is the temperature. Therefore, the spring constant of the cantilever k can be determined by measuring $\langle Z_c^2 \rangle$,

$$k = \frac{k_B T}{\langle Z_c^2 \rangle} \tag{3.11}$$

The mean square of cantilever displacement $\langle Z_c^2 \rangle$ is obtained by carrying out a power spectral density analysis of the cantilever oscillation and afterwards integrating the area under the peak of the first oscillation mode.
Since AFM measures inclination of the cantilever's end and not the displacement, Butt and Jaschke [128] corrected the Equation 3.11 by taking into account the tilt of the cantilever. The corrected equation for the first mode oscillation of a rectangular cantilever is [129]:

$$k = 0.817 \cdot \frac{k_B T}{\langle Z_c^{*2} \rangle} \cos^2 \theta \tag{3.12}$$

where $\langle Z_c^{*2} \rangle$ is the displacement of the cantilever measured by optical detection and θ is the tilt angle of the cantilever.

4 Hydrodynamic Force Between a Sphere and a Soft, Elastic Surface

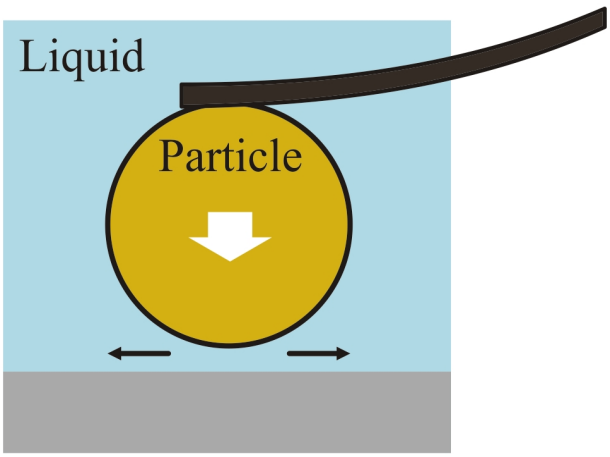

Hard Substrate

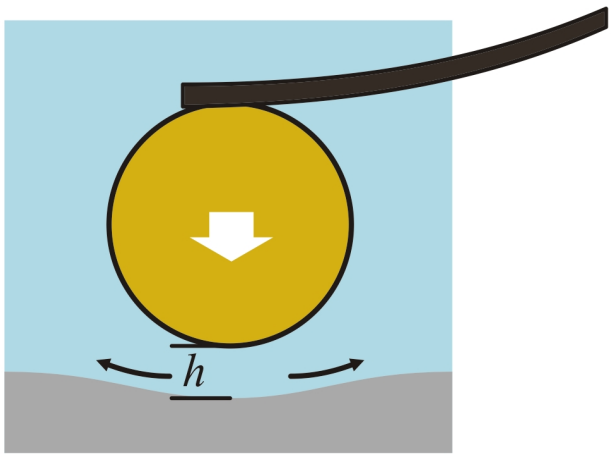

Soft Substrate

In this chapter, the hydrodynamic drainage force between a spherical silica particle (colloidal probe) and a soft, elastic polydimethylsiloxane (PDMS) surface, using the colloidal probe technique is described. The experimental force curves are compared to finite element simulations and the predictions of an analytical model. The simulation of this work is done by Javed Ally.

4.1 Introduction

In wet adhesion, the space between the two adhering solid surface is filled with a liquid, usually an aqueous electrolyte. Wet adhesion is dominated by capillary and hydrodynamic forces; the latter is sometimes called Stefan adhesion [130]. Van der Waals forces between solid surfaces are usually weak in liquids because the Hamaker constant is typically ten times lower than the case of air or vacuum [67, 73]. Capillary forces appear in presence of a liquid meniscus. Without a meniscus, i.e. in dry conditions or when the whole space is filled with liquid, capillary forces are absent. Stefan adhesion is the adhesive force that appears due to viscous resistance as two parallel planar surfaces are pulled apart in a fluid. While, the fluid has to fill the widening gap leading to hydrodynamic viscous force. The smaller the gap and the higher the separation speed and viscosity of the liquid, the greater the hydrodynamic force is required to separate the surfaces. Thus, Stefan adhesion is particularly important when pulling wet surfaces apart, which have been initially in mutual contact. In bioadhesion, this can help animals such as limpets [131] holding onto the surfaces against violent buffeting or shaking. Hydrodynamic forces between two surfaces in liquid have been measured and calculated for various geometries, such as two parallel circular plates [130, 132]. The most important geometry is a sphere of radius R moving towards or away from a planar surface [133–136]. A sphere at a distance h from a plane surface moving at a velocity U in a Newtonian liquid of viscosity η experiences a distance dependent hydrodynamic force [67, 73, 131–137]

$$F = -\frac{6\pi\eta R^2 U}{h}. \tag{4.1}$$

Equation 4.1 only describes the hydrodynamic drainage force between the sphere and the plane surface and does not include hydrodynamic Stokes friction of sphere in the liquid. However, for distances smaller than the sphere radius, the drainage force is by far dominating. The negative sign indicates that the hydrodynamic force is opposite to the direction of the velocity. The first experiments on force between a sphere and a plane surface were carried out by observing a falling sphere [134, 138, 139]. In the last decade hydrodynamic forces have been measured extensively with the colloidal probe technique mainly to analyze slip [101, 140–142]. Hydrodynamic force has also been studied for film

drainage between a hard surface and a soft, deformable air-liquid interface and in the context of particle-bubble, particle-drop or a soft-soft interaction with the surface forces apparatus (SFA) [143] AFM [144, 145]. Also hydrodynamic force between biomembranes have been analyzed [146].
Leroy and Charlaix studied elasto-hydrodynamic interactions between oscillating spheres and elastic films, and developed an analytical model to determine the elastic modulus of the film [147]. This model was used to measure the elastic moduli of various substrates based on measurements with a SFA [147], and to study drag force and slip length on microstructured surfaces [148]. The model of Leroy and Charlaix requires that the substrate deformation and amplitude of motion of the sphere are small relative to the distance between the sphere and substrate. For studies relating to bioadhesion, we are, however, interested in large amplitude motions that approach the point of contact between surfaces. In order to understand the effect of elastic deformability on hydrodynamic forces, we studied the interaction of a hard sphere and soft, deformable surface as they are brought into contact and pulled apart at various speeds using an AFM. We also developed a numerical model of a sphere interacting with a soft substrate to study the effect of different parameters such as particle size and speed, liquid viscosity, and substrate elasticity. The experimental measurements were used to verify the accuracy of the finite element model. Using the verified numerical model it was possible to study the effects of the parameters over larger ranges than feasible by experimental measurement alone. The numerical model provides additional information about the geometry of the deformed substrate and the liquid flow field around the particle, which cannot be determined from the AFM experiments alone.

4.2 Numerical Model

Numerical simulation of the particle and soft substrate is complicated by the coupling between the liquid motion caused by the moving particle and the deformation of the substrate. When the particle is very close to the substrate, the deformation of the solid alters the boundary geometry of the fluid. We account for this coupling in our simulation. We consider the mechanics of the solid and fluid systems separately, and take advantage of the linearity of the equations governing their motion to couple the deformation of the substrate with the fluid flow.

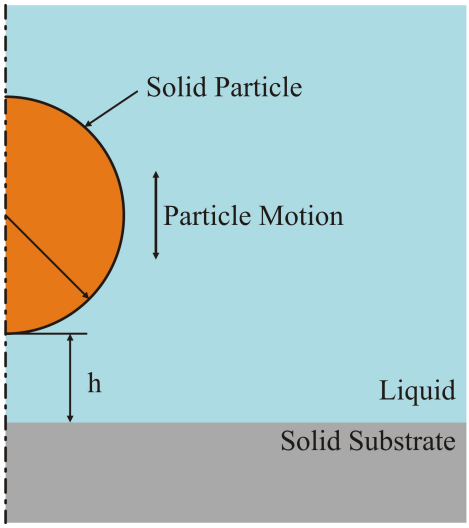

Figure 4.1: The axisymmetric model geometry for a spherical solid particle approaching a solid substrate in a liquid environment.

Considering a spherical particle moving normal to a surface allowed us to simplify our model to an axisymmetric geometry consisting of the section of the particle closest to the substrate, the fluid volume around this section of the particle, and the solid substrate (Figure 4.1). Since the particle is small, liquid flow is laminar, dominated by viscosity and governed by the Stokes equation. We do not consider the entire particle, as the distance-dependent viscous drag is dominated by the lower cap of the particle. The deformation of the substrate is small, and can thus be considered linearly elastic over each time step of our simulation. As the particle is much more rigid than the substrate, we ignore deformations of the particle.

We calculate the liquid flow and solid substrate deformation using finite element analysis (FEA) with the COMSOL Multiphysics package, version 4.2.a. We simulate the approach of the particle toward the substrate and retraction away from it. To model the particle motion, a no-slip condition [149] was assumed at the particle and substrate surfaces. The continuity equation was applied to the other boundaries of the fluid volume, since the liquid was assumed to behave as incompressible fluid.

To couple the liquid and solid substrate, we apply a boundary load at the substrate surface equal to the pressure in the liquid at the interface. The shear stresses at the surface are negligible in comparison with the pressure. Therefore we neglected shear stress for simplicity. The base of the solid volume is rigidly constrained, and the stress and deformation at the edges of the solid volume are assumed to be zero since they are far from the applied stress due to the particle. This assumption and the volume size was

checked and confirmed by convergence analysis. The volume size was increased until the difference in the total stress at the particle surface between successive runs was less than 1%.

In the first step, we simulated the liquid flow between the particle and substrate when the distance between them is larger than the particle diameter. The deformation of the substrate is initially negligible. The pressure distribution in the liquid at the liquid-substrate boundary was applied to the substrate as a boundary load. The radial shear stress is also negligible, so it was not included in our model. We then calculated the substrate deformation under the applied hydrodynamic pressure.

For the next iteration, the calculated deformation of the substrate was considered as the new liquid-substrate boundary. To do this, we took the result of the initial step and, beginning from the center axis of the system where the deformation is the largest, found the point at which the deformation is less than 1%. The interval between the center axis and this point defines the deformed region of the fluid-substrate interface. The deformation was modeled with one hundred evenly spaced position data points from this region. The model geometry was updated by using a cubically interpolated polynomial curve defined by these hundred data points. The mesh was updated for the new geometry. After the initial step, the particle-substrate separation, geometry, and mesh were adjusted. The liquid flow was recalculated with the deformed geometry. The geometry was then updated for the following time step. This procedure was iterated until the particle was close to the substrate. The force on the particle at each step was calculated from the liquid flow in the simulation by integrating the stresses along the particle surface.

A consequence of this modeling approach is that the substrate deformation lags behind the velocity field; i.e. the substrate deformation in each time step corresponds to the fluid flow from the previous step. Thus, the time steps were chosen sufficiently short that the difference can be neglected. Since the experimental measurements were carried out using an AFM, the simulation also had to account for the changes in the particle position due to cantilever deflection. The force on the particle was measured from the deflection of the AFM cantilever; as the force on the particle changes, so does the cantilever deflection. Thus, the motion of the particle is a combination of the constant velocity applied to the cantilever base and the cantilever deflection velocity due to the force on the particle. The velocity in the model was corrected to account for this. The correction was determined in each time step by calculating the derivative of the force on the particle with time using a backward finite difference, and dividing this value by the spring constant of the cantilever used in the experiments.

In order to validate the FEM simulations, the calculations for the hard substrate were done as comparison. We solved the equation of motion for a sphere moving towards a

hard flat surface (silicon). The hydrodynamic force is balanced by the restoring force of the cantilever:

$$F_K = K(h - h_0 + \nu_0 t). \tag{4.2}$$

Here, h_0 is the initial septation at t = 0. The term $h - h_0 + \nu_0 t$ is equal to the deflection of the cantilever. The effect of the hydrodynamic force is to retard the particle. As a consequence, the velocity of the particle at given time t is not equal to ν_0 because the changing deflection of the cantilever has to be taken into account [101]. The equation of motion was solved by plugging in the experimental parameters. Calculation were carried out separately for the approaching and the retracting parts.

4.3 Experimental Methods

As a model system, the hydrodynamic interaction was measured between borosilicate spheres in ethanol and substrates consisting of silicon as a hard substrate and PDMS as a soft one. We use ethanol instead of water in order to avoid hydrophobic interactions and reduce electrostatic repulsion.

4.3.1 Hard Substrate

On a hard substrate, a silicon wafer, the hydrodynamic force appears as a strong repulsion on approach (Figure 4.2a) and a strong attraction when retracting the sphere again (Figure 4.2b). The force decreases steeply with distance and increases with the velocity. Experiments were performed with several particles, cantilevers, and substrates. For better comparison, the experimental results shown in the following figures are taken from measurements with a single colloidal probe of 15.5 µm diameter attached to a cantilever with a spring constant of 1.87 N/m. The results obtained with other probes were consistent with those in Figure 4.2 and Figure 4.3. In all force curves the maximal applied force was constant (1000 nN). When an AFM cantilever moves through a fluid, whether or not a particle is attached, there is some drag force exerted on the cantilever itself. To account for this, the numerical force curves must be offset along the force axis. The required offset was determined from the measured force at each velocity when the particle was at the maximum distance far away from the substrate for both approach and retraction. At this distance, the observed force is by far dominated by the hydrodynamic drag force on the cantilever. For comparing simulations and experiments, this cantilever drag force was added to the respective simulated force curves.

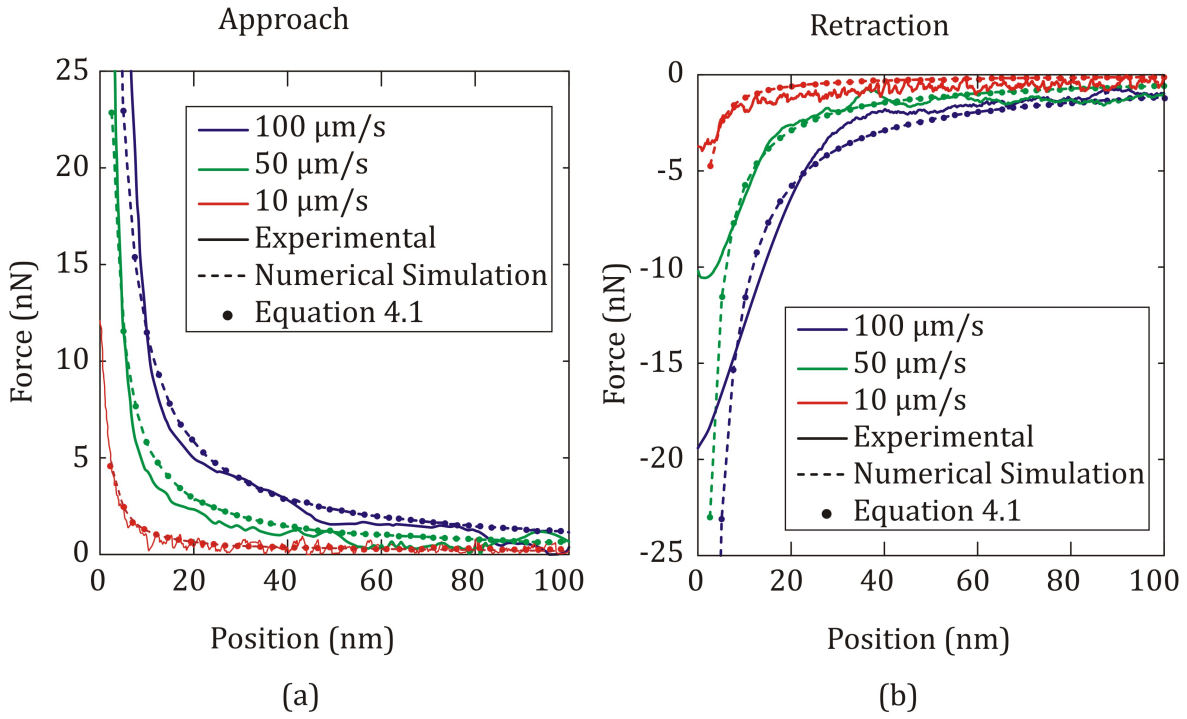

Figure 4.2: Force curves for a 15.5 µm diameter silica particle (a) approaching and (b) retracting from a hard silicon surface. The solid lines are the experimental results; the dashed lines are the results of the numerical model, the dots correspond to the results calculated with Equation 4.1.

In the experimental measurements, the particle position was determined from the extension of the AFM piezoelectric actuator. The measured position values are given relative to the initial position of the actuator. The numerical results, on the other hand, are given with respect to the initial, undeformed position of the solid substrate, i.e. in the case of the hard substrate, the particle makes contact at position '0'. In all measurements on hard surfaces the maximum force was reached before the particle made actual contact with the surface. If the particle was in contact with the hard surface in any of the measurements, the slope of the force curve would be vertical; i.e. the force would increase as the particle is pushed onto the silica wafer without corresponding change in the position. In all measurements the slope of the force curve was finite, proving that the particle never actually makes contact with the surface.
Since it is not possible to determine absolute zero distance in the AFM measurements, the offset in the position axis was determined using least-squares fit with the results of Equation 4.1. With the above-mentioned corrections, the numerically calculated force curves for a hard surface show good agreement with the measurements and calculated forces from Equation 4.1. This shows that the numerical model is valid for hard surfaces in the explored speed range. Force curves recorded at high speeds exhibit a lower

attractive force upon retraction than expected by the model calculations. This can be explained by the fact that when approaching is fast, the particle does not get as close to the substrate as it does when approaching is slow. As a result, the hydrodynamic drainage force is reduced because the starting separation is larger. Force curves calculated with Equation 4.1 and numerically agreed well. Experimental and theoretical force curves nicely agreed. The experimental force curves were slightly steeper close to contact, whereas at large distances the experimentally measured force was slightly lower than calculated. One possible explanation is the influence of the cantilever. We neglected any distance dependent contribution of the cantilever. There may be two contributions. First, the direct distance dependent hydrodynamic force on the cantilever. For spheres with $R \geq 5-7\,\mu\text{m}$ this effect should be negligible because the cantilever is always at least $10 - 14\,\mu\text{m}$ away from the substrate [140]. Second, when the silica sphere approaches the planar surface it is gradually slowed down. This slow-down not only reduces the hydrodynamic drag on the microsphere, but also on the cantilever [150]. It effectively reduced the hydrodynamic drag on the cantilever because the drag is proportional to the speed.

4.3.2 Soft Substrate

For distances $\ll 100$ nm the deformation of PDMS leads to a decrease of the hydrodynamic force during approach (Figure 4.3a) compared to the hard silicon wafer substrate. Upon retraction, we find a higher hydrodynamic force between probe and PDMS (Figure 4.3b). The numerical results for the soft surface agreed well with the experimental measurements. The effect of a soft surface is, that since it is deformed by the hydrodynamic force, the separation distance h between the particle and surface is larger on approach, so that the hydrodynamic force is reduced. On retraction, after a short initial phase, the distance is smaller. The particle pulls on the surface, deforming it upwards, before the particle is completely separated. The adhesion force is larger for the soft surface, since the particle forms a larger area of close contact due to the surface deformation.

The deformation of the soft substrate complicates the definition of zero distances. Therefore, the true distance, the minimal separation between the colloidal particle and the PDMS surface, can only be obtained from a comparison with the numerical solution. Therefore, as before for the hard substrate, zero distance for experimental force curves was obtained by shifting the experimentally obtained distance until optimum match between experimental curves and simulations was obtained. It should be noted that in the following distance is always plotted as the distance from the position of the originally undeformed PDMS surface.

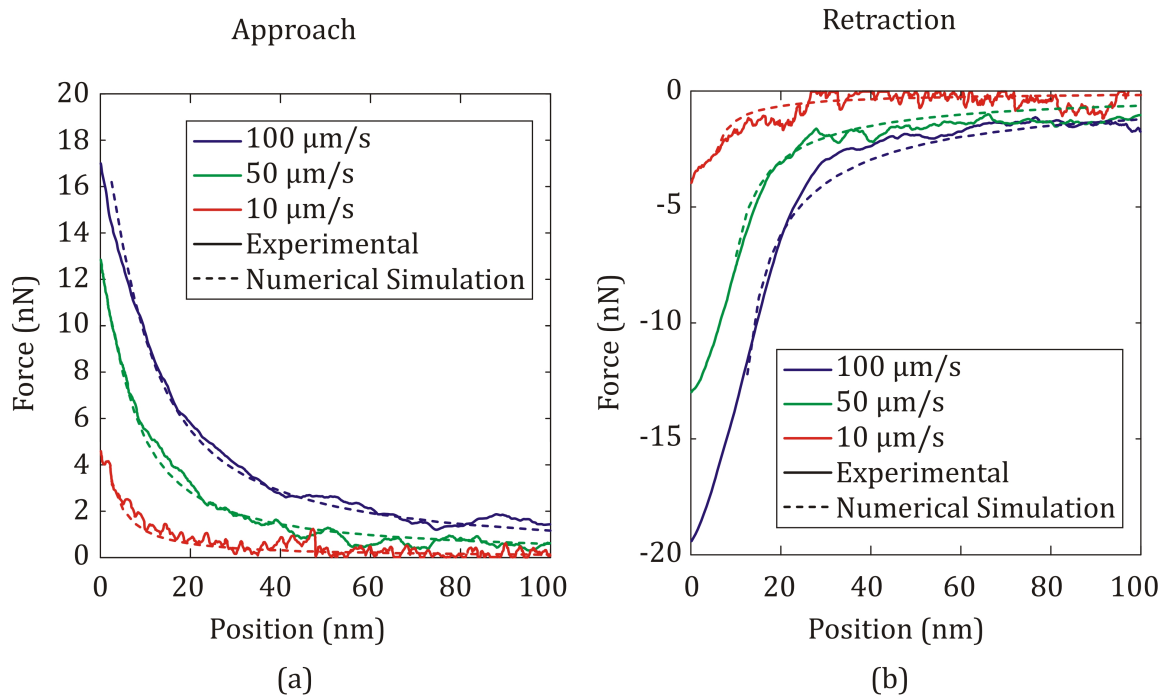

Figure 4.3: Force curves for a 1.55 µm diameter silica particle (a) approaching and (b) being retracted from a soft PDMS surface (E = 1.3 MPa). The solid lines are the experimental results; the dashed lines are the results of the numerical model.

For low approach speeds ($\ll$10 µm/s) we were able to form contact with the PDMS substrate during approach. This contact allows us to calculate the elastic modulus of the PDMS from the contact region of the force curve using the Hertz model for contact between a sphere and an elastic substrate. The elastic modulus calculated from the fit was 1.3 MPa. This value was used in the calculation of the numerical force curves for PDMS. The corrections for the drag force on the cantilever were applied in the same way as for the hard substrate.

From the AFM experiments, we can only conclude that the PDMS deforms strong enough upon approach to reduce the hydrodynamic interaction. From the simulation, we can quantify the amount of deformation (Figure 4.4). The closer the sphere approaches towards the original position of the undeformed interface, the more the interface gets deformed. At a distance of 10 nm from the original position, the interface has already deformed by another 10 nm, leading to a significant reduction of the hydrodynamic interaction. During retraction, the drainage force leads to an upward deformation of the PDMS surface (Figure 4.5), which is strongest while the separation is still small (about 9 nm at a distance of 12.5 nm from the position of the undeformed interface, leaving a gap of only 3.5 nm). This upward deformation retards the widening of the gap and increases the hydrodynamic drainage force compared to a hard substrate.

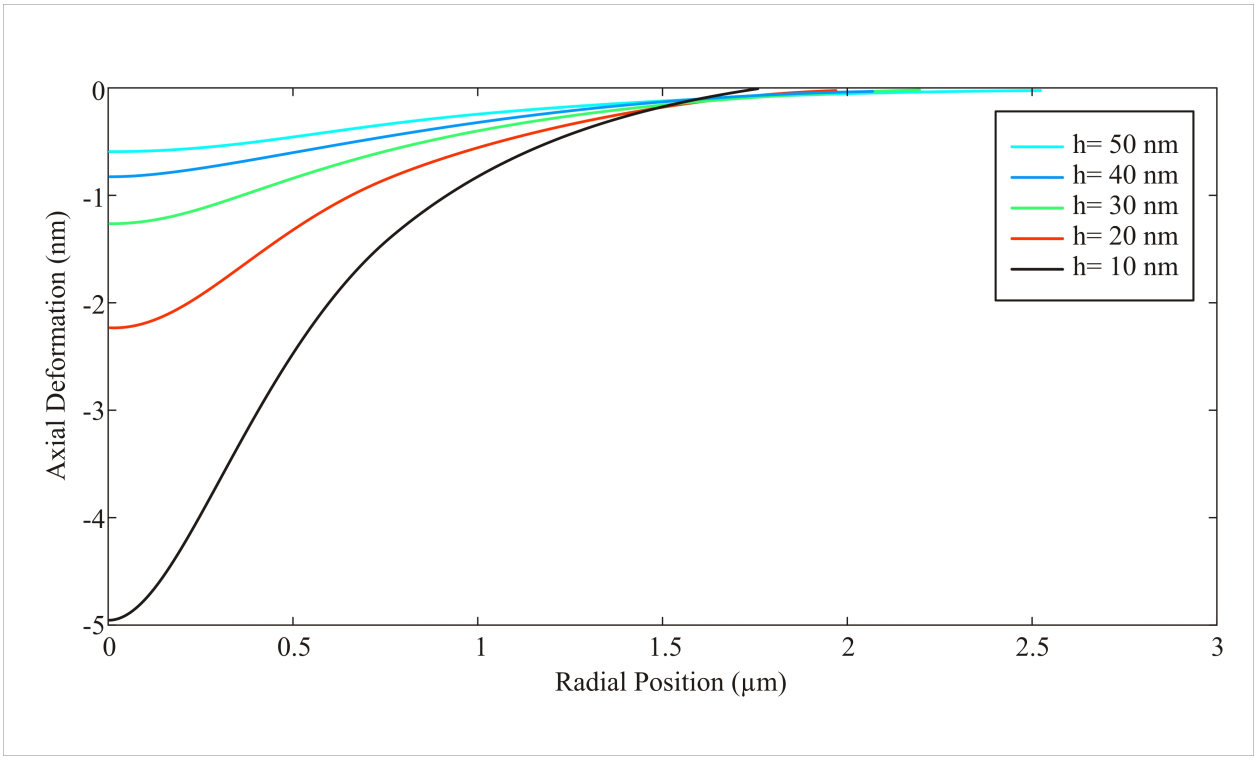

Figure 4.4: Deformation of PDMS versus radial position for an approaching sphere with a velocity of 90 μm/s for different heights h from the position of the undeformed interface. At $h = 10$ nm the sphere ($D = 15.5\,\mu$m) has reached the initial position of the PDMS surface.

After having verified the numerical simulations by experiments we use them to investigate the effect of surface deformability (Figure 4.6). The softer the surface, the more pronounced the effect on the hydrodynamic force is: the reduction of repulsion on approach becomes more pronounced with decreasing Young's modulus of the material. The attraction on separation increases with decreasing Young's modulus.

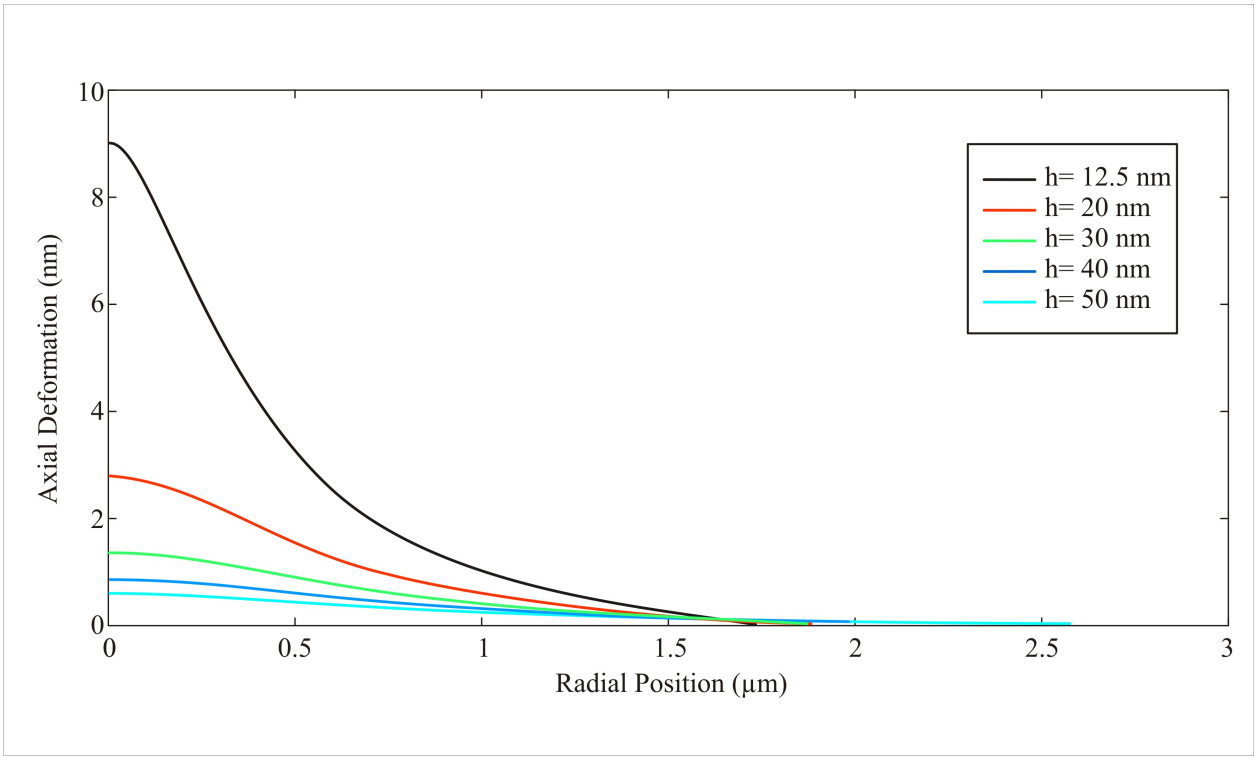

Figure 4.5: Upward deformation of the PDMS surface during retract of the sphere at a speed of 90 μm/s for different heights h from the position of the undeformed interface.

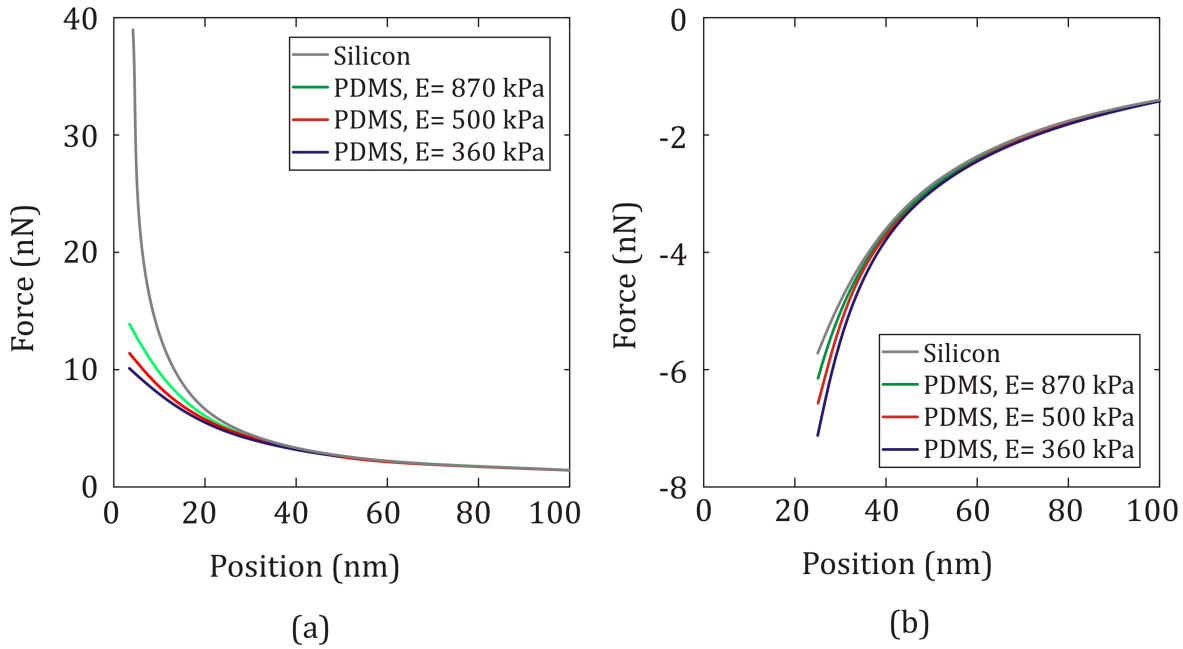

Figure 4.6: Numerically calculated force curves for different Young's moduli of the substrate for a 14 μm diameter silica particle approaching (a) and retracting (b) at a speed of 90 μm/s.

4.3.3 Conclusion

The numerical finite element model was validated and proved to be consistent with experimental results over a range of particle speeds by colloidal probe experiments. The force required to separate a particle from a soft, elastic substrates in liquid is higher than that for a hard substrate. An elastic, soft surface has the effect of decreasing the hydrodynamic force as a spherical particle approaches the surface. It increases hydrodynamic attraction when the particle is pulled away. In the context of bioadhesion, these results show why soft foot pads are advantageous: The hydrodynamic contribution to wet bioadhesion increases by soft adhering surfaces. This would provide stability, particularly against violent buffeting, and allowing time to find more secure footing than if the adhering surfaces, e.g. toe pads, were hard.

5 Capillary Force Between a Soft Single Pillar and a Planar Surface

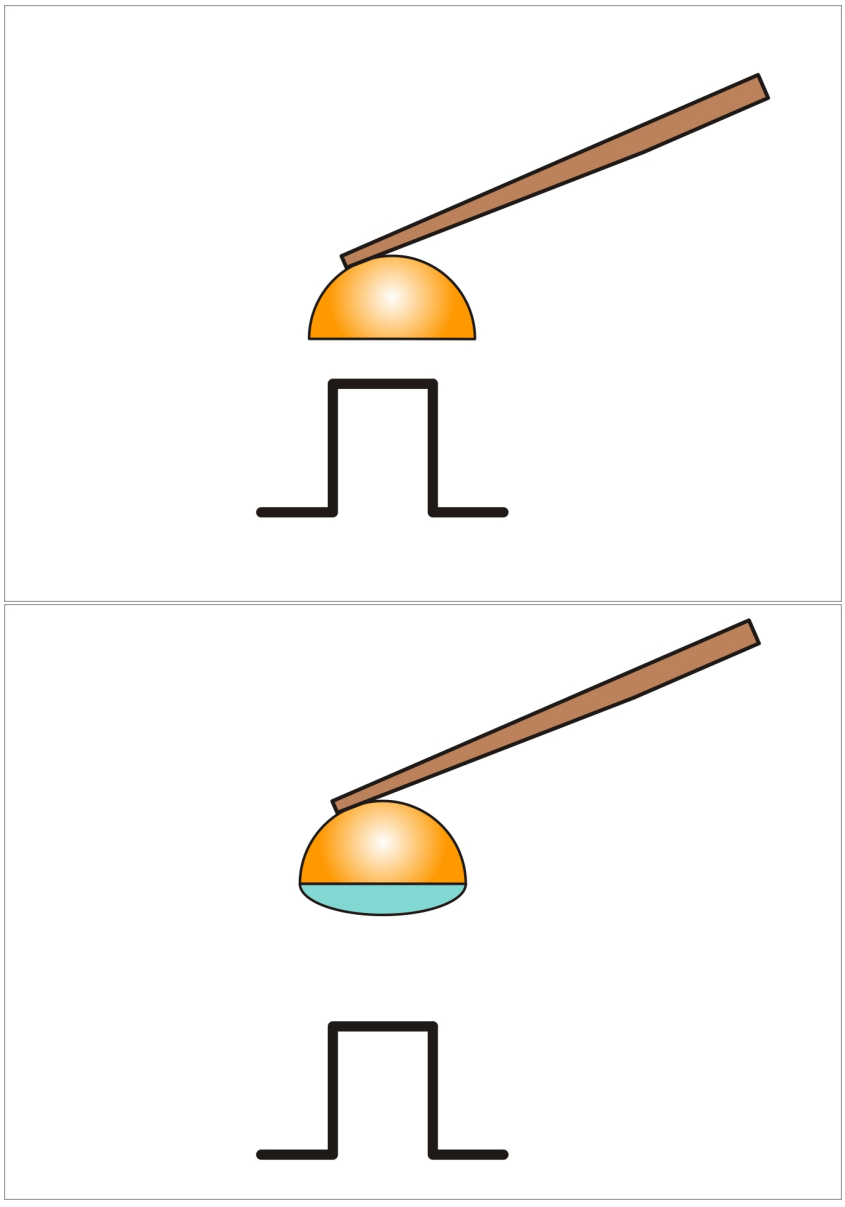

In this chapter, the capillary forces have been studied. Furthermore, elastic micro-structured surfaces were fabricated in order to mimic the toe pads of the tree frogs. The adhesion forces between soft, elastic and hexagonally patterned substrate and planar silica particle (colloidal probe) were investigated. The force is measured by AFM in the presence of a liquid layer; wet condition and in absence of a liquid layer; dry condition, on different shape of micro-structured pillars on hydrophobic and hydrophilic surfaces. Studying the system at single pillar level, which is the smallest part of the toe pad of frogs, gives us a better insight into the adhesion mechanism of tree frogs.

5.1 Introduction

In nature, many animals are able to attach to surfaces by using their especial adhesive pads such as some insects, gecko and tree frogs. The dynamic mechanisms of animal's adhesion have attracted scientific interest in the last decade. The reversible adhesions of animals are of particular interest. By understanding and mimicking the reversible adhesion in animals, we can benefit it in our daily life in different cases, such as using reversible plasters or to produce non slippery tires. To facilitate these, we need to have good adhesion and on the other hand easy detachment from the surface.

5.2 Experimental Method

Adhesion force measurements were done in absence of a liquid layer (dry condition) and in presence of a liquid layer (wet condition) on hydrophobic and hydrophilic surfaces on Normal shape, T-shape and concave cup pillars. For making the surface wet, we used glycerol. Glycerol can wet the surface properly (contact angle on hydrophilic PDMS is 10 °) and it has high surface tension of 64 mN/m and a viscosity of 1.146 MPa.S at 20 °C. Adhesion forces were measured by AFM (Dimension 3100, USA) using colloidal probe. For each sires of measurement adhesion measurements on single pillar, 30 force curves were recorded.

5.3 Results and Discussion

Capillary and hydrodynamic forces are two important components in wet adhesion. Capillary force is the static term of the wet adhesion. It consists of the surface tensional force and the Laplace pressure force terms. Hydrodynamic force is the dynamic term of wet adhesion [144, 146]. It occurs due to the viscous resistance of the fluid. As two surfaces are pulled apart from each other in presence of liquid, the liquid has to flow into the gap in between. Hydrodynamic force is especially important when surfaces are

pulled apart at high speed. It strongly depends on the distance between two surfaces and the viscosity of the liquid. Hydrodynamic force could explain the movement of the frogs when they jump or move with certain speed.

5.3.1 Dependence of Adhesion on the Velocity of the Probe

Inspired by walking and climbing tree frogs, adhesion forces on a single pillar were measured with modified colloidal probe. This spherical probe was cut off at the bottom to result in a plane / plane contact with the top surface of the pillars. This series of experiments are done under dry and wet condition at different probe velocities (8 - 100 µm/s) on hydrophobic and hydrophilic surfaces. The role of hydrodynamic force in wet adhesion is investigated. In Figure 5.1, adhesion force on Normal shape pillar under dry and wet condition and hydrophobic and hydrophilic surfaces are shown. For each data point, 30 force curves were recorded and averaged. Under wet condition, small amount of glycerol was put on the surface and then the adhesion forces were measured at different probe velocities on single pillars.

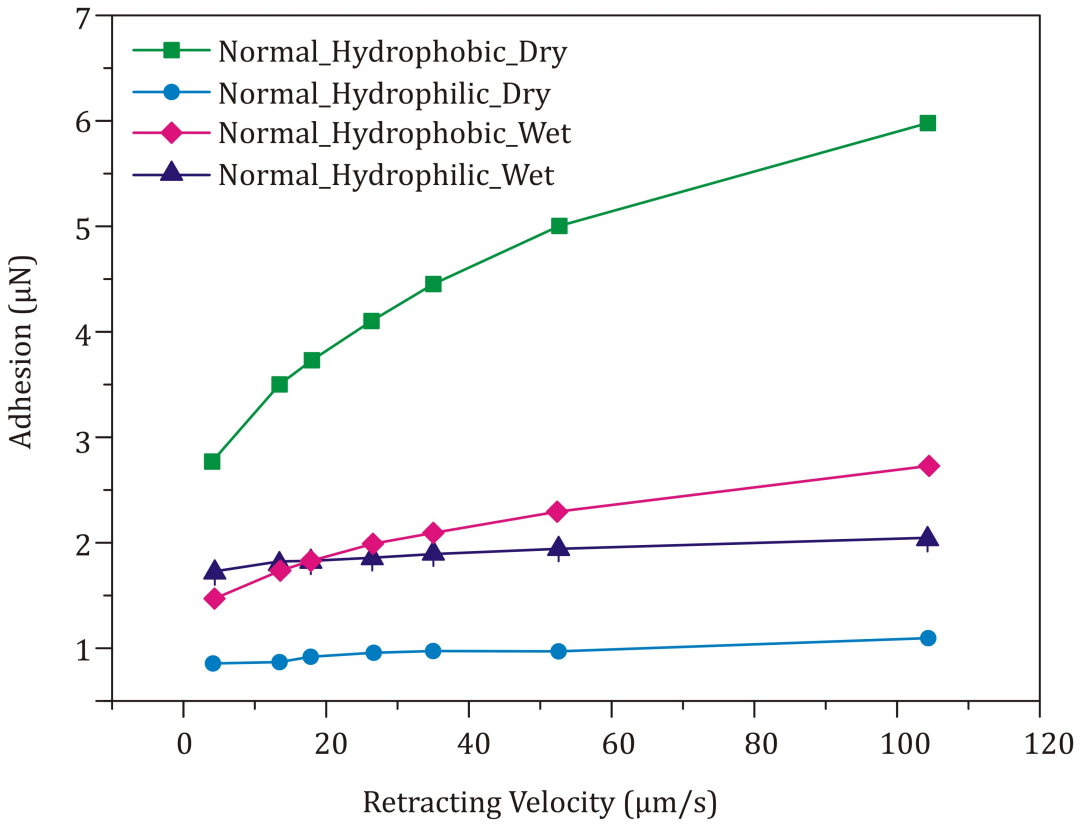

Figure 5.1: Velocity dependence of adhesion force on Normal shape pillar on hydrophobic and hydrophilic surface under dry and wet condition.

In dry condition, adhesion force on the hydrophobic surface is slightly higher than the hydrophilic surface. In terms of surface energy, we expect that adhesion force should be higher on the hydrophilic surfaces than the hydrophobic one. We used two different methods to understand the reason for higher adhesion on the hydrophobic surfaces. At first, we took AFM images of hydrophobic (Figure 5.2) and hydrophilic (Figure 5.3) surfaces in order to compare the roughness of the surfaces. The AFM images show that the roughness does not change dramatically from hydrophobic to hydrophilic surfaces. The rms roughness on hydrophobic surface is 0.494 nm and on hydrophilic is 0.604 nm.

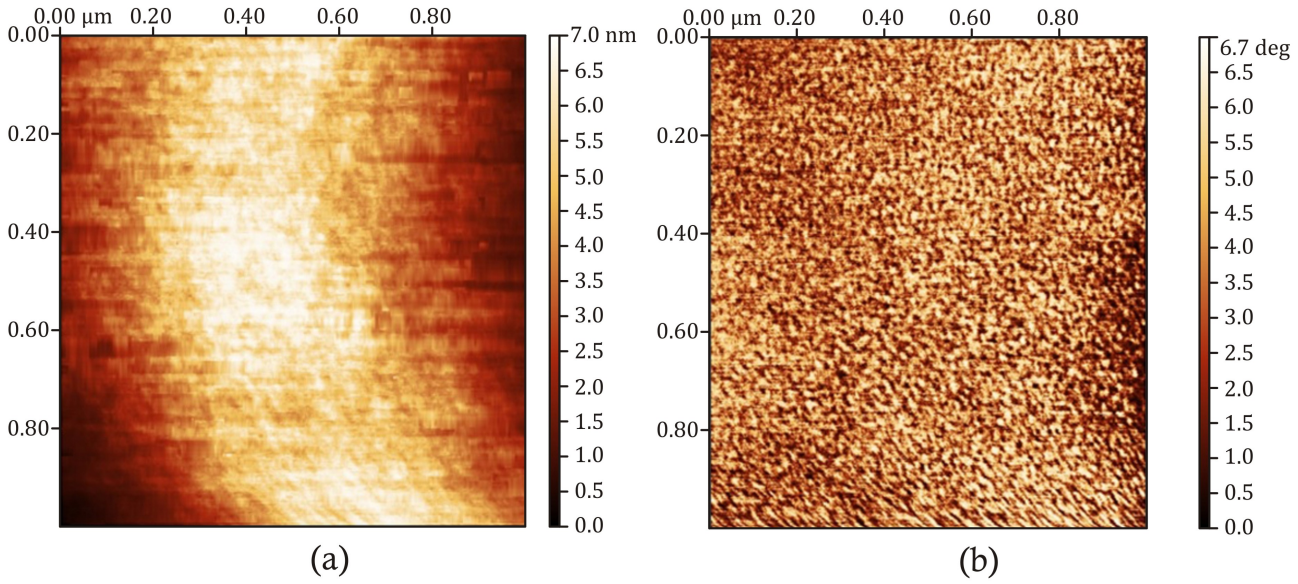

Figure 5.2: AFM tapping mode images of the surface of a hydrophobic pillar (a) height image (b) phase image.

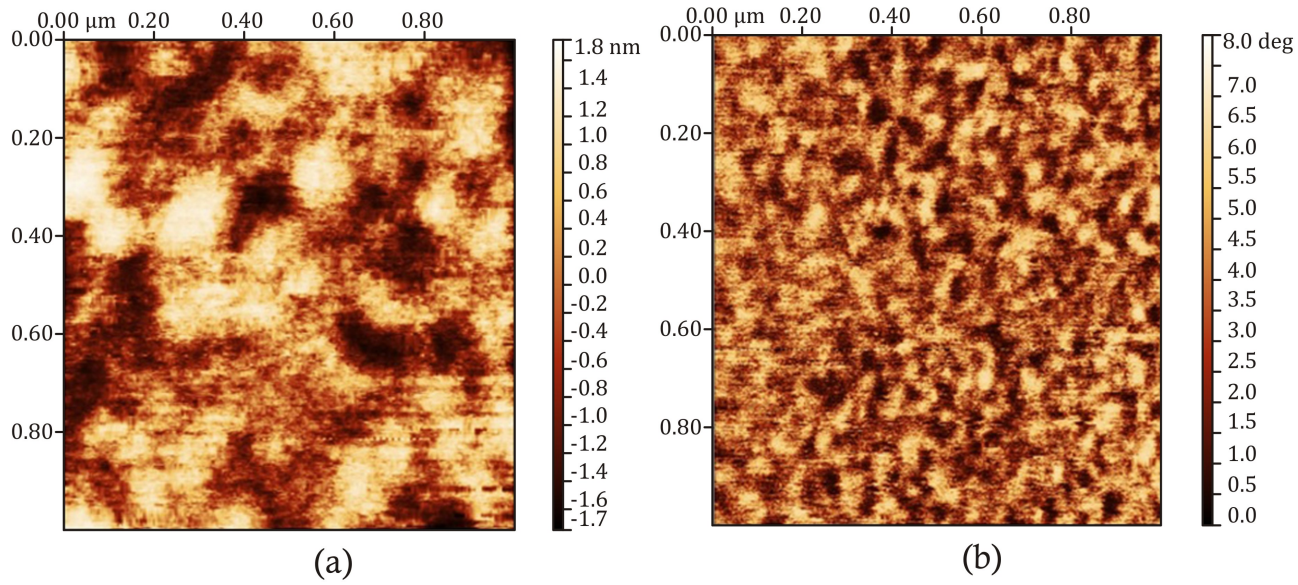

Figure 5.3: AFM tapping mode images of the surface of a hydrophilic pillar (a) height images (b) phase image.

Second, we recorded force curves with a standard AFM cantilever with a sharp tip on hydrophobic and hydrophilic pillars. The recorded force curves show, that the surface of hydrophilic surfaces is harder than the hydrophobic one. This is likely due to the formation of a thin glassy layer of SiO_2 during the plasma treatment and it has made

the hydrophilic surface harder. Thus, the adhesion is slightly higher on hydrophobic surfaces than hydrophilic in our measurements (Figure 5.4) even though the surface energy of the hydrophobic PDMS is lower.

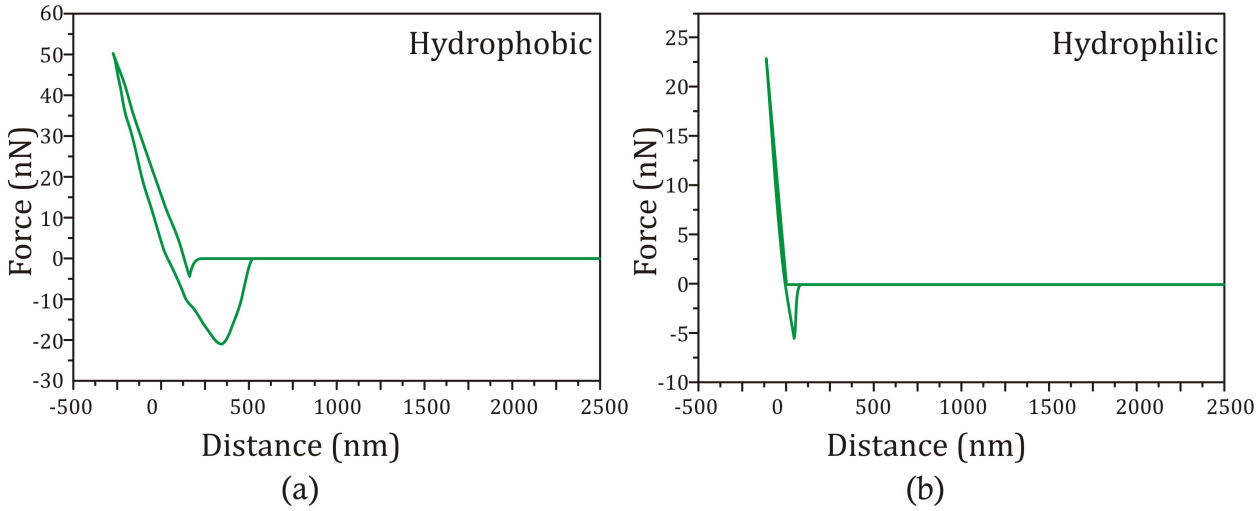

Figure 5.4: Force curves recorded with a standard AFM cantilever with a sharp tip on Normal shape (a) hydrophobic pillar and, (b) hydrophilic pillar. On the hydrophilic pillar; image (b), due to the formation of a thin glassy layer of SiO_2 during the plasma treatment, the glassy layer prevents the viscoelastic dissipation as it is present on the hydrophobic pillar; image (a).

Even as the surface energy is higher for the hydrophilic surface, adhesion is lower, since the glassy layer prevents viscoelastic dissipation. As is shown in Figure 5.1, the adhesion force increases by increasing the probe velocity on Normal shape pillar. This increase in adhesion by probe velocity is due to the visco-elastic properties of PDMS. If the hydrodynamic force has any contribution to the adhesion force, the same increasing trend should not have occurred under dry condition. This results indicated that the increase in adhesion by increasing the speed is due to a peeling effect. During peeling, a crack at the edge of the probe and surface is formed and detachment proceeds by crack propagation. Peeling force is increased by increasing the probe velocity.
Adhesion forces depending on probe velocity are measured on T-shape and concave cup pillars as well.

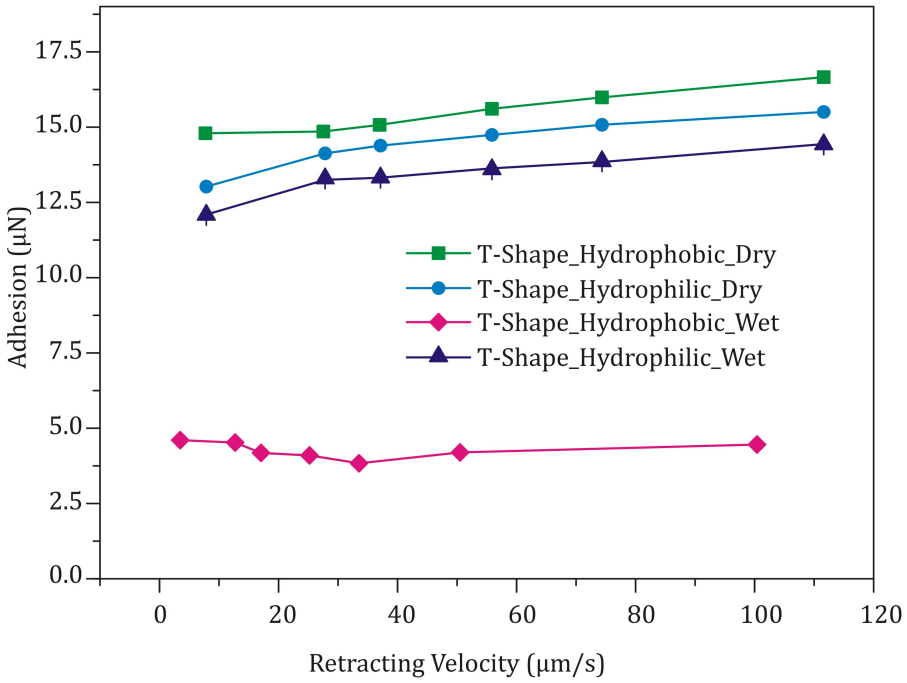

Figure 5.5: Velocity dependence of adhesion force on T-shape pillar on hydrophobic and hydrophilic surface under dry and wet condition.

In Figure 5.5, the adhesion force measurement versus probe velocity is presented. The result show that adhesion force of T-shape pillars under dry condition is higher on hydrophobic surface when compared with hydrophilic surface. A reverse trend is shown by the surfaces under wet condition, where adhesion force is higher on hydrophilic pillars when compared to the hydrophobic pillars.

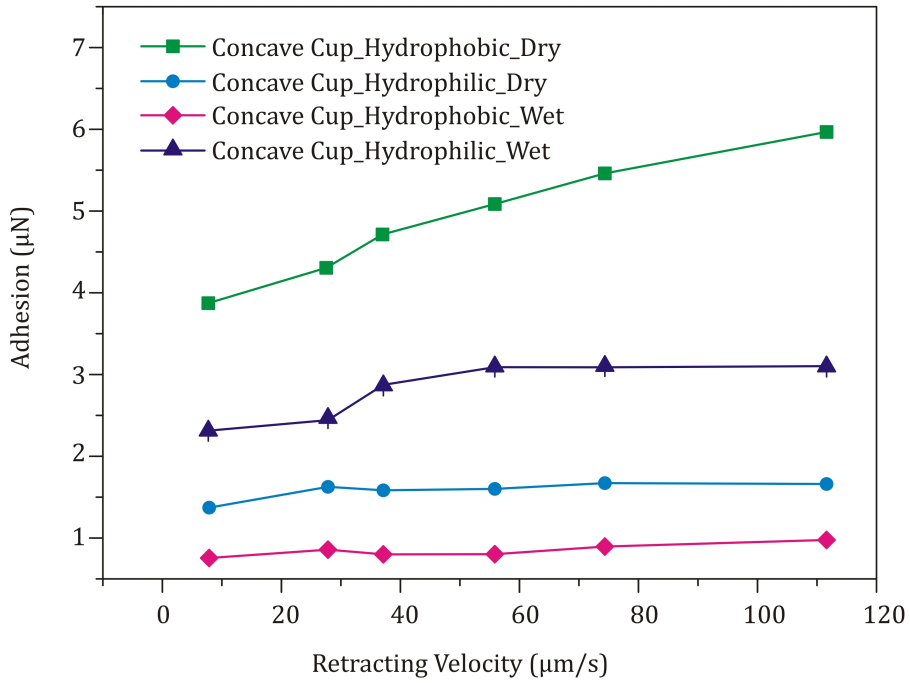

Figure 5.6: Velocity dependence of adhesion force on concave cup pillar on hydrophobic and hydrophilic surface under dry and wet condition.

The dependence of the adhesion force on the retracting velocity is studied for concave cup pillars as well. The experiments were conducted on hydrophobic and hydrophilic surfaced pillars under dry and wet conditions (Figure 5.6). The results shows that the adhesion force is higher on hydrophobic pillars than the hydrophilic pillars under dry condition. Whereas under wet condition, hydrophilic pillars shows a higher value of adhesion force than the hydrophobic surface.
Measurements of the velocity dependence on Normal shape, T-shape and concave cup pillars on hydrophobic and hydrophilic surfaces show that under wet condition, the adhesion force increases by increasing the probe velocity. Force measurements performed in dry conditions, show an increase in the adhesion force with increasing in the probe velocity as well. This indicates that the speed dependence is not due to hydrodynamic forces but due to viscoelastic dissipation in the PDMS during pull-off. A velocity dependent of adhesion on PDMS surfaces has been observed before [151–154].
Experiments on the velocity dependence proved that hydrodynamic force does not play a significant role in wet adhesion and the observed speed dependence is attributed either to viscous dissipation of the PDMS [153, 154] or to inter-diffusion of interfacial polymer chains [151, 152].

5.3.2 Comparison of Adhesion Force Between Different Pillar Shapes under Dry Condition

Adhesion forces were measured on Normal shape, T-shape and concave cup pillars under dry condition on both hydrophilic (indicated by a orange line on the top of the pillar in cartoons in Figure 5.7) and hydrophobic surfaces. Experimental result with a comparison between the different structured pillars is presented in Figure 5.7. Each bar in Figure 5.7 shows the value of the adhesion averaged over 30 different pillars. T-shape pillars (orange) show higher adhesion compared to the Normal shape (green) and concave cup (blue) pillars. The over hanging parts in T-shape structure reduce the stress concentration at the edges of the pillars during the pull-off. Therefore, separation from the top of the T-shape pillar requires more force compared to Normal shape pillar. In case of Normal shape pillars, the stress is maximal on the edges of the pillars. Upward motion of the probe causes crack formation and propagation at the edges and detachment of the probe from the top of the pillar starts from the edge of the pillar when the critical stress for crack propagation is exceeded.

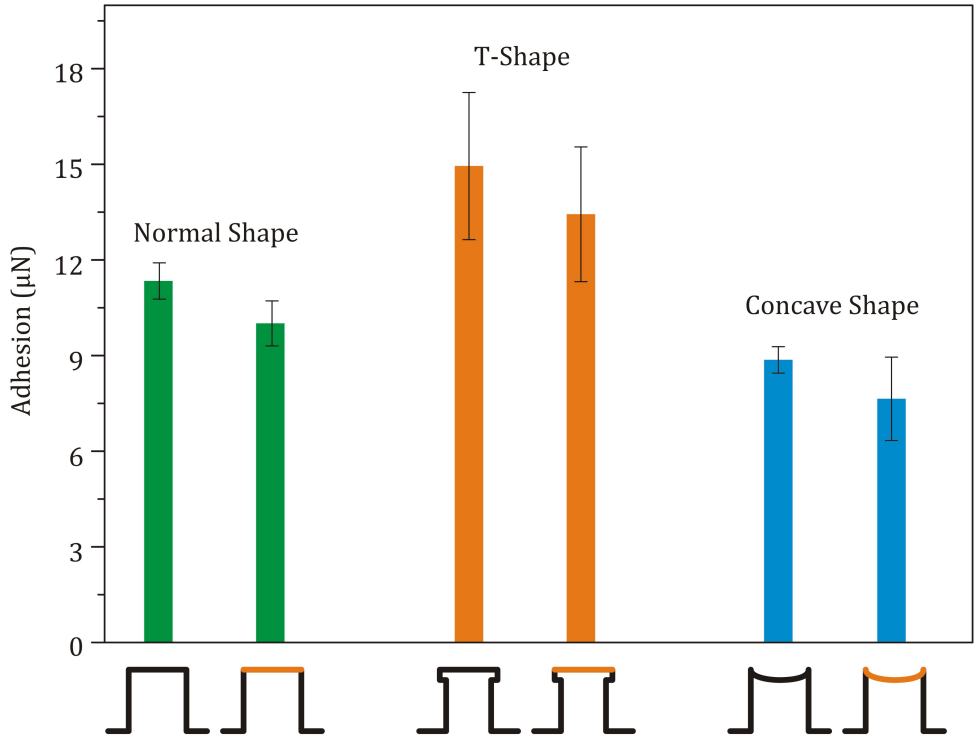

Figure 5.7: Experimental results on the comparison of the adhesion forces of different structured pillars: Normal pillar (green bars), T-shape pillar (orange bars), and concave cup pillar (blue bars). Results are obtained under dry condition for both hydrophobic and hydrophilic (orange line on the top) surfaces.

The adhesion force has been measured on 8 different concave cup pillars at different preloads under dry condition, in order to investigate whether there is any suction effect. The adhesion force on different concave cup pillars at different preloads under dry condition were investigated. Experiments have been performed for a range of preloads from 0.2 μN to 12 μN. The result are shown in Figure 5.8. It is evident from the result, that the adhesion force does not vary significantly by increasing the preload on the pillars. By increasing of preload by 25% , the adhesion increased by only 2.3%, which is already a first indication that there is no suction force present. Furthermore, the adhesion is lower on concave pillars compared to normal shape pillars. Hence, it can be concluded that there is no suction effect present even at the lowest load.

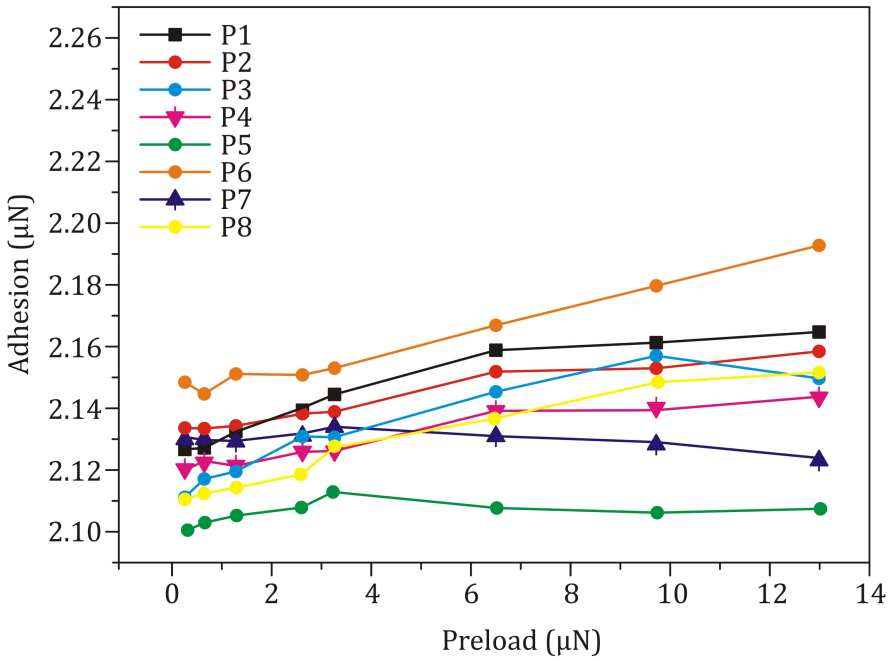

Figure 5.8: Load dependence of adhesion force on eight hydrophobic-concave cup pillars under dry condition. P_1 to P_8 are represent eight different pillars.

5.3.3 Quasi-Static Measurements

Adhesion measurements were performed on different single pillars. To understand how the adhesion varies from one pillar to another pillar on the surface, we measured adhesion force on several single pillars at different parts of the sample. All Quasi-static measurements were performed at 8 µm/s probe velocity. In the velocity dependence section, the wetness of the pillars was not controlled because our aim was to understand the effect of the softness on the adhesion force. In this part we controlled the wetness of the pillars in order to investigate the effect of the volume of the liquid on the adhesion force. In velocity dependence section we have seen that adhesion force is varying when different amount of glycerol was applied on the pillar. Therefore we aimed to carry out experiments with a controlled amount of liquid applied to single pillar. To achieve this goal, we implemented the following protocol: one drop of glycerol was deposited on a clean glass slide (Figure 5.9). Using glycerol instead of water was necessary to avoid fast evaporation of the tiny amount of liquid used in these experiments. A sacrificial cantilever is brought into contact with the glycerol to pick up a small amount of it. Several small (at the order of micron size) glycerol spots can be deposited onto the glass slide by using a micromanipulator to touch the glass surface with the glycerol-loaded cantilever. Then we switched to a new cantilever with the colloidal probe. The resonance frequency

of this cantilever was measured before wetting it with the glycerol (f_0). In the next step, a tiny split glycerol was picked up by colloidal probe, later the frequency of the probe (including the tiny glycerol droplet on it) was measured again (f_1). After picking up a small droplet the resonance frequency decreased due to the added mass. Afterwards, the colloidal probe was approached to a pillar and 30 force curves were recorded. At the end of the force measurement on a pillar, the resonance frequency of probe was measured again (f_2). The mass of a glycerol droplet on a colloidal probe (m_1) and the mass of a glycerol transferred for wetting a pillar (m_2) were calculated from the changes in resonance frequency as described by Equation 5.1.

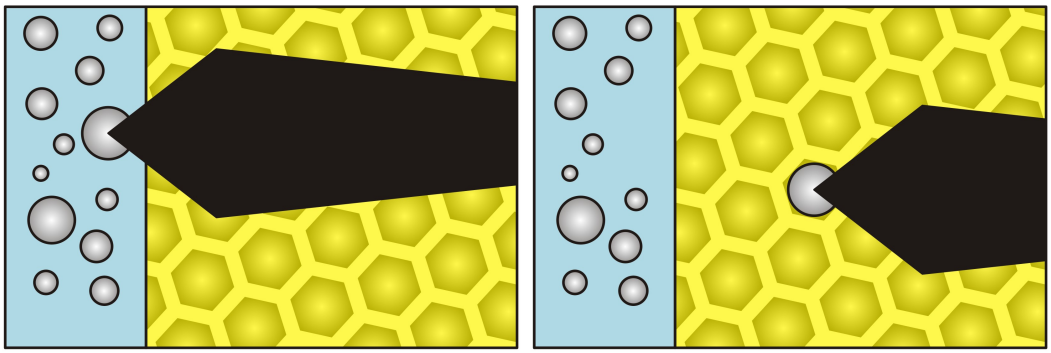

Figure 5.9: (a) A droplet of glycerol being picked up with a colloidal probe (b) the picked up droplet on top of the pillar before force measurement.

$$\begin{aligned} \omega &= \sqrt{\frac{k}{m}} \\ m_1 &= |\frac{k}{4\pi^2}(\frac{1}{{f_1}^2} - \frac{1}{{f_0}^2})| \\ m_2 &= |\frac{k}{4\pi^2}(\frac{1}{{f_2}^2} - \frac{1}{{f_1}^2})| \end{aligned} \tag{5.1}$$

The results of the adhesion measurements on single pillars show strong variation in adhesion, depending on the amount of glycerol on the probe. To understand the effect of amount of glycerol on adhesion force on single pillars, the adhesion is measured on different pillars with defined amount of glycerol. The adhesion force measurement on Normal shape pillars under dry and wet condition and different surfaces are measured and the results are shown in Figure 5.10. Each bar represents the average value of adhe-

sion force on at least ten different pillars. The most interesting case is wet, hydrophilic condition which should be the closest to the toe pad of the frogs. The big deviation among various measurements on the wet-hydrophilic surface (reflected in the size of the error bar), indicates that the adhesion has varied a lot from one pillar to another one. In this case, in each adhesion measurements the volume of the glycerol on the probe was different. Therefore the adhesion changes from one pillar to another pillar.

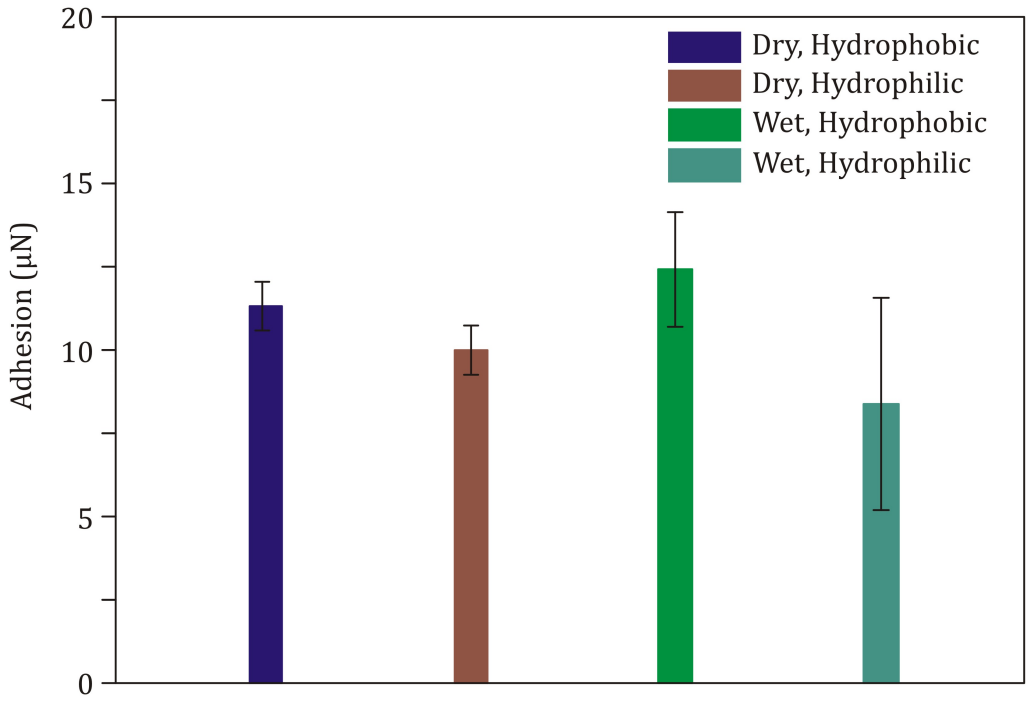

Figure 5.10: Static measurement on Normal shape pillar under dry and wet conditions on hydrophobic and hydrophilic surfaces.

We have investigated the relation between the amount of the glycerol on the probe with adhesion on the pillar. Results from the measurements are given in detail in Figure 5.11.

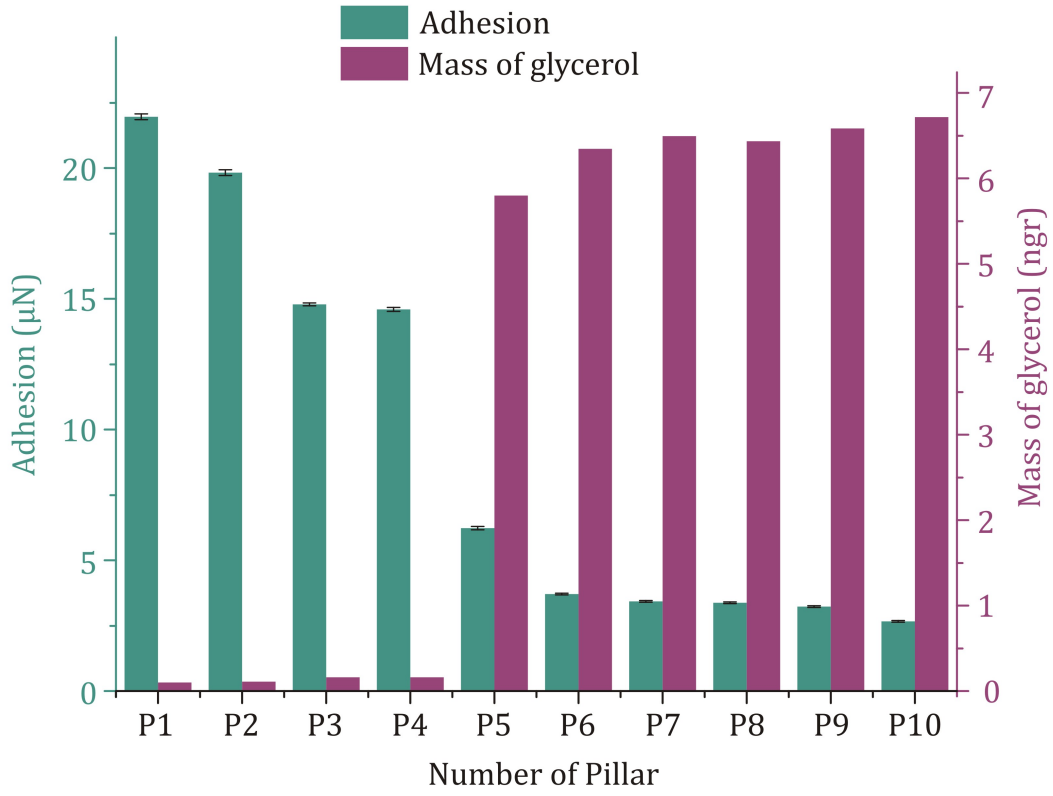

Figure 5.11: Adhesion force on ten Normal shape-hydrophilic pillars (green) with the corresponded mass of glycerol (violet) on them.

In Figure 5.11 the adhesion values on ten different pillars are plotted against the correspond mass of glycerol on the probe. The results verify that adhesion force increases by decreasing the mass of glycerol on top of the pillar. The same measurements were performed on T-shape and concave cup pillars as well. Quasi-static measurements on T-shape pillars shown in Figure 5.12, demonstrate that in absence of glycerol the adhesion force is slightly higher on hydrophobic surfaces than hydrophilic ones similar to the case of Normal shape.

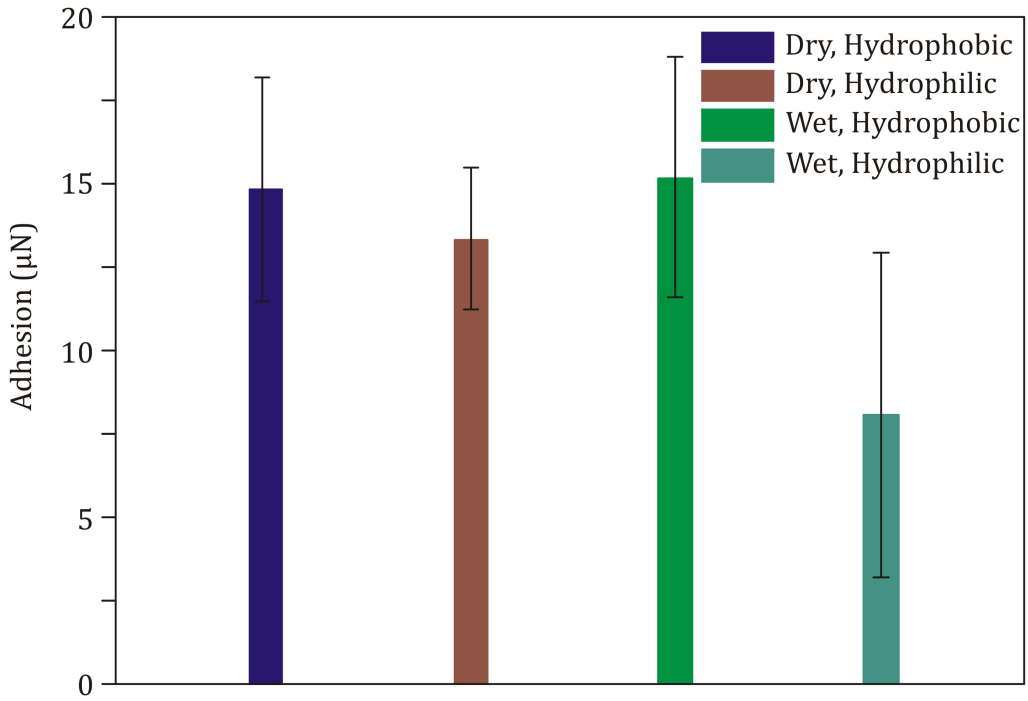

Figure 5.12: Static measurement on T-shape pillars under dry and wet conditions on hydrophobic and hydrophilic surfaces.

We repeated the same experiments on concave cup pillars as well. Results are shown in Figure 5.13. Each bar represents the average value of adhesion force for at least 10 different single concave cup pillars. In dry condition the hydrophobic surface has higher adhesion force compared to the hydrophilic one. Under wet condition, the adhesion force depends on the mass of glycerol on top of the pillar.

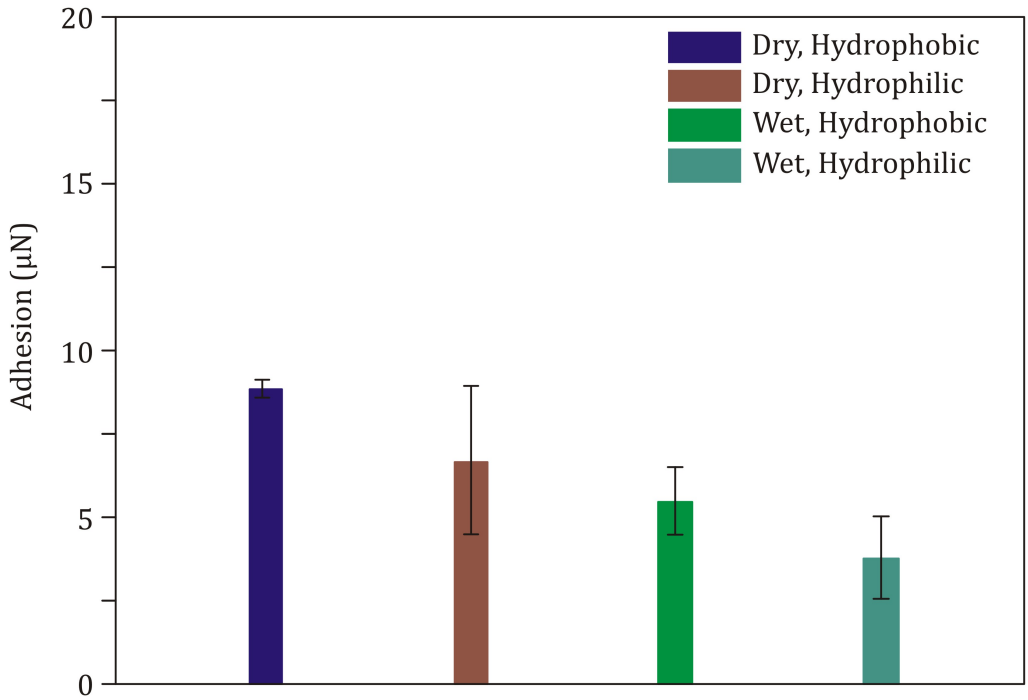

Figure 5.13: Static measurement on concave cup pillars under dry and wet conditions on hydrophobic and hydrophilic surfaces.

Figure 5.14 shows the adhesion force and the corresponded mass of glycerol on ten hydrophilic, concave cup pillars under wet condition. The adhesion force on the pillar has higher value when the mass of glycerol on the probe is smaller.

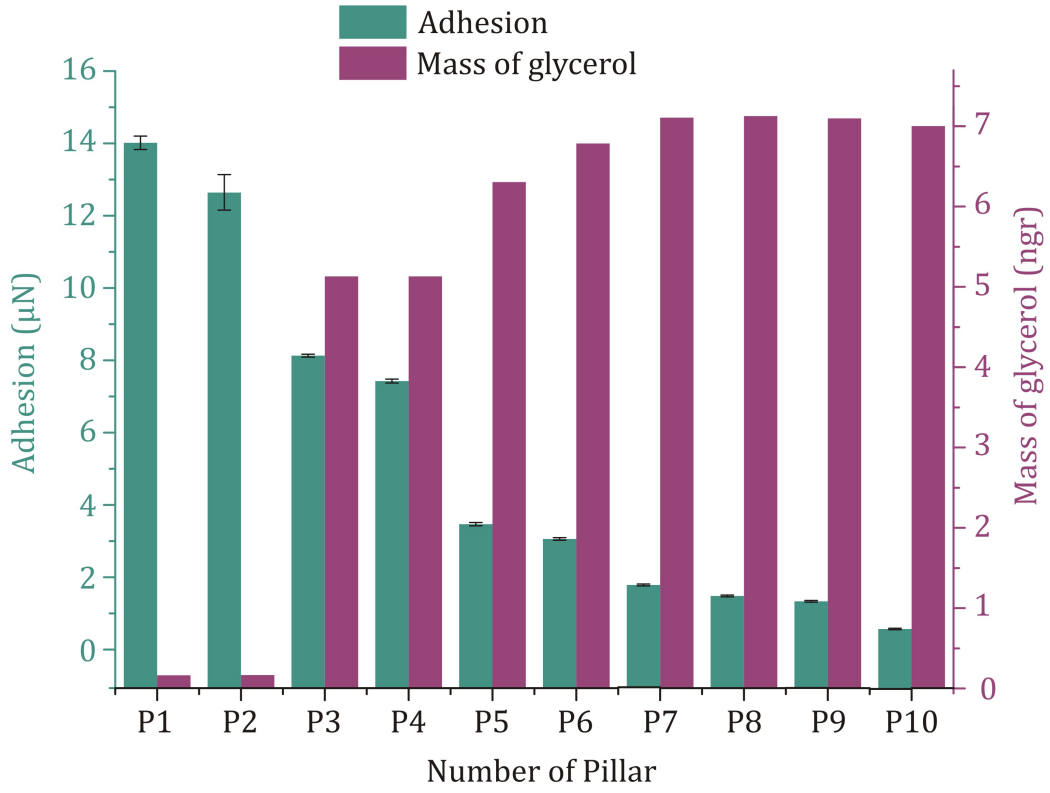

Figure 5.14: Adhesion force on ten concave cup-hydrophilic pillars with corresponded mass of glycerol on them.

5.4 Theory

The experimental results show that the amount of glycerol is the critical parameters controlling the adhesion force. This leads us to the hypothesis that capillary forces are dominating in our experiments. In Figure 5.15 one example of experimental curve on Normal shape, hydrophilic is presented. Three main features are observed in experimental curve. The kink, the rapture point of the drop and the long extension of the retract part. The long extension of the retract part also hints to stretching of a meniscus and rupture of it. From our experimental results we have qualitative understanding of significant contribution of capillary forces in adhesion. We would like to investigate whether a quantitative description of the capillary forces is possible. And what is the origin of the kink. To answer these questions, in this section, we model our experimental system (colloidal probe and pillar in presence of glycerol drop) using numerical calculations.

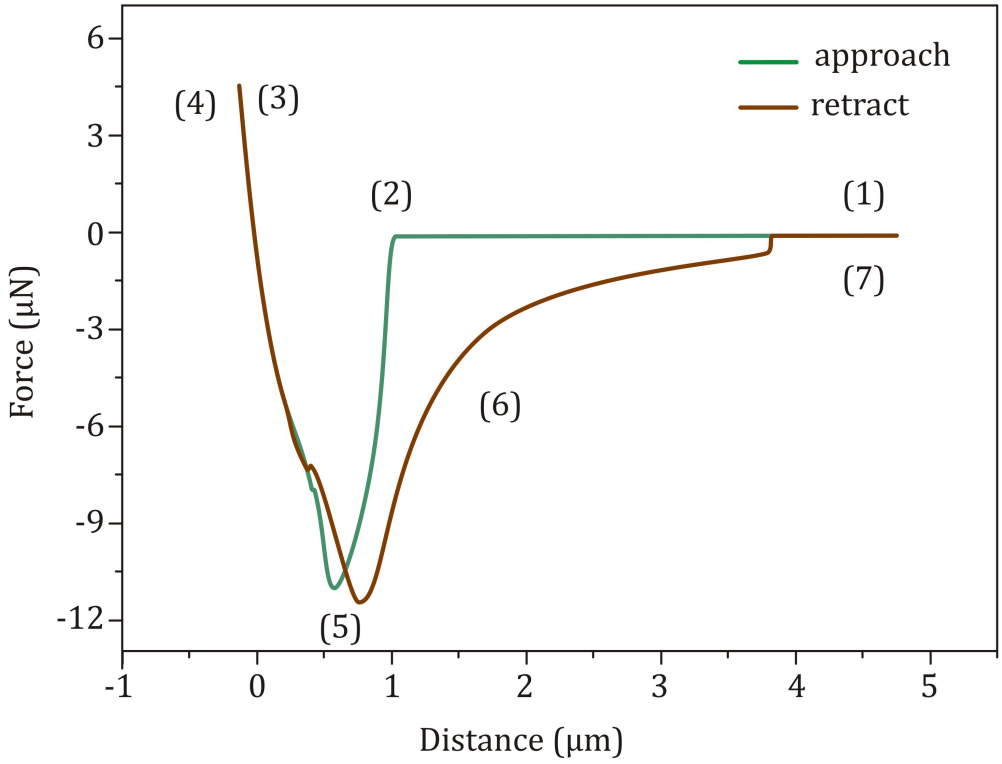

Figure 5.15: Experimental force curve of Normal shape-hydrophilic pillar under wet condition. The colloidal probe is far from the surface, no force was detected, part (1). As the colloidal probe goes closer to the surface and the liquid snaps into the pillar, we will have long range attractive force in the approach part, part (2). In part (3), the probe goes down until reaches the maximum set point and the meniscus slides down on the pillar. At the zero distance we start to compress the pillar. Therefore, the positive force has been observed. When the colloidal probe goes back the retracting part will start part (4) until the probe reaches the maximum capillary force (minimum force) which is shown in part (5). After that the retract part deviates from the approach part. This occurs because in approach the meniscus is formed and at this situation in the retract part the meniscus is already there and by pulling the probe up, the meniscus starts to stretch out, which is obvious in part (6). The probe goes up till the complete rupture of the meniscus happens, part (7).

According to the results from Figure 5.15, when the colloidal probe is far from the surface, no force was detected, part (1). As the colloidal probe goes closer to the surface and the liquid snaps into the pillar, we will have long range attractive force in the approach part, Part (2). In part (3), the probe goes down until reaches the maximum set point and the meniscus slides down on the pillar. At the zero distance we start to compress the pillar. Therefore, the positive force has been observed. When the colloidal probe goes back the retracting part will start part (4) until the probe reaches the maximum capillary force

(minimum force) which is shown in part (5). After that the retract part deviates from the approach part. This occurs because in approach the meniscus is formed and at this situation in the retract part the meniscus is already there and by pulling the probe up, the meniscus starts to stretch out, which is obvious in part (6). The probe goes up till the complete rupture of the meniscus happens, part (7).
In Quasi-static experiments, we observed that adhesion force has higher value when the mass of glycerol on top of the pillar is lower. In this section, we calculated capillary force in order to understand its contribution to the total measured force. The schematic image of a planar colloidal probe approaching to the top of a pillar, in presence of glycerol, is shown in Figure 5.16. We calculated the capillary force between modified colloidal probe and Normal shape, hydrophilic pillar according to the Equation 5.2.

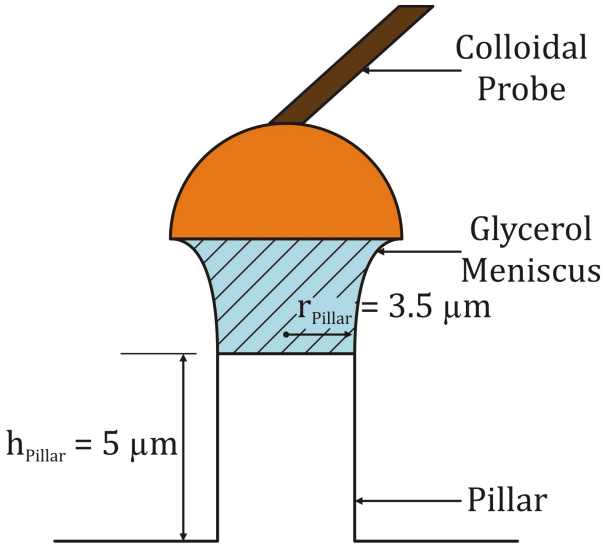

Figure 5.16: Schematic image of a cut colloidal probe and a pillar in presence of glycerol.

We used the "constant mean curvature" surfaces theory to get the geometry of the droplet on the pillar. Capillary force has two components: surface tensional force and Laplace pressure force. In Equation 5.2, the first term is surface tensional force, which is due to the surface tension of a droplet at the interface and the second term is Laplace pressure force, which is due to the pressure difference inside and outside of the droplet.

$$F_{Capillary} = 2\pi r(z)\gamma - \pi r^2(z)\Delta P \tag{5.2}$$

The Laplace pressure term can be described as a function of mean curvature of the meniscus, leading to

$$F_{Capillary} = 2\pi r(z)\gamma - \pi r^2(z)(\gamma H) \tag{5.3}$$

Where, r = 3.5 µm is the radius of the pillar and γ = 64 mN/m is the surface tension of glycerol [155]. ρ = 1.26 gr/cm^3 is the density of glycerol and ΔP is the difference in pressure inside and outside of the droplet and H is the curvature of the meniscus. According to Equation 5.3, by knowing the curvature of the meniscus, capillary force could be calculated. Thus, Surface Evolver (Version 2.7) was used to calculate the capillary force between the planar probe and the pillar. Surface Evolver is a program that numerically calculates the shapes of interfaces by minimizing their energy. These could be liquid-gas or liquid-liquid interfaces. In principle Surface Evolver calculates the shape of the meniscus for each position of a colloidal probe approaching to and retracting from the pillar and calculates the corresponding force. For simplicity in calculation, we consider a pillar as a rigid, cylindrical solid.

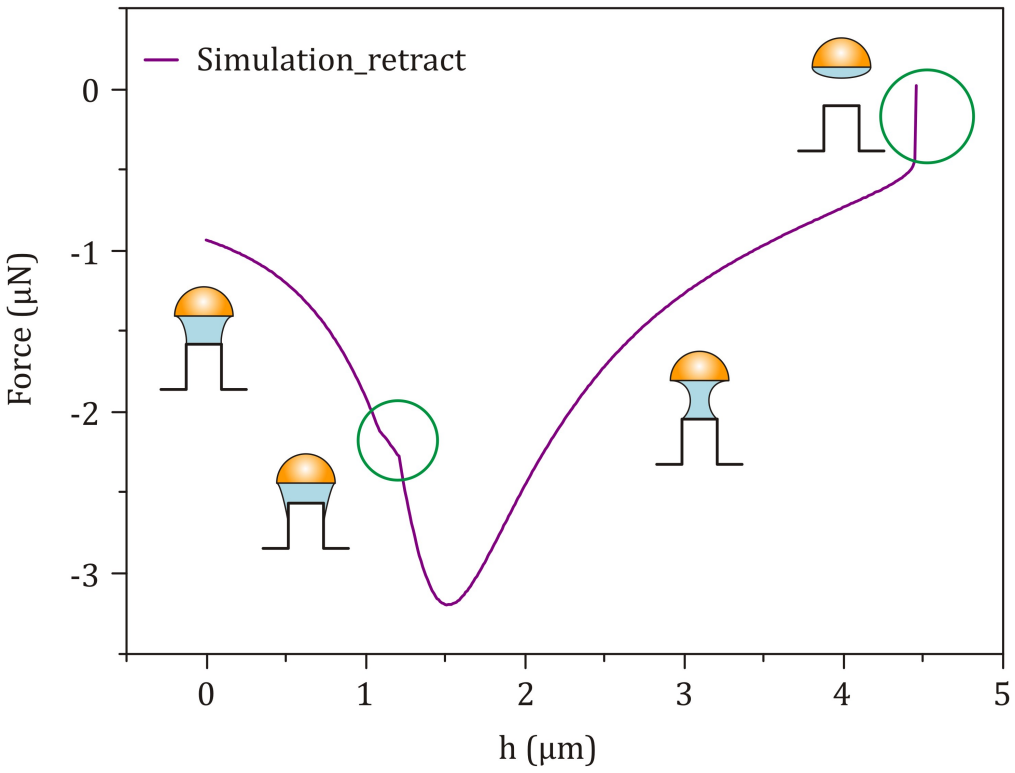

Figure 5.17: The simulation of retract part of the force curve using experimental parameters. Measured volume is V = 60 µm^3. The cartoons show the main features of experimental curves.

In Figure 5.17, experimental parameters such as radius of the pillar (3.5 µm), radius of the probe (5 µm), and the measured volume of glycerol on the probe ($V = 60\,\mu m^3$) have been plugged into the Equation 5.3 to simulate the capillary force between the probe and the pillar in presence of glycerol. As a result of the simulation, a curve similar to the experimental curve was obtained. The kink, the rupture point and stretching part of the meniscus were observed in simulation curve as well. From the numerical modeling, we understand the shape of the meniscus and prove the depinning of the drop from the top of the pillar.
While there is a good qualitative agreement between experiments and calculation, there is a discrepancy in the value of the minimum force between experimental curve and simulation curve, when we used our experimental parameters for simulation. As evident from Figure 5.18, this discrepancy disappears when the volume of the glycerol plugged into the simulation, is changed to $V = 21\,\mu m^3$. It indicates that some of the glycerol applied to the probe does not contribute to the meniscus. It might either be wetting the upper part of the probe and form a meniscus between particle and cantilever or it might be shifted down the pillar and end up as a meniscus between pillar side wall and bottom of the PDMS structures.

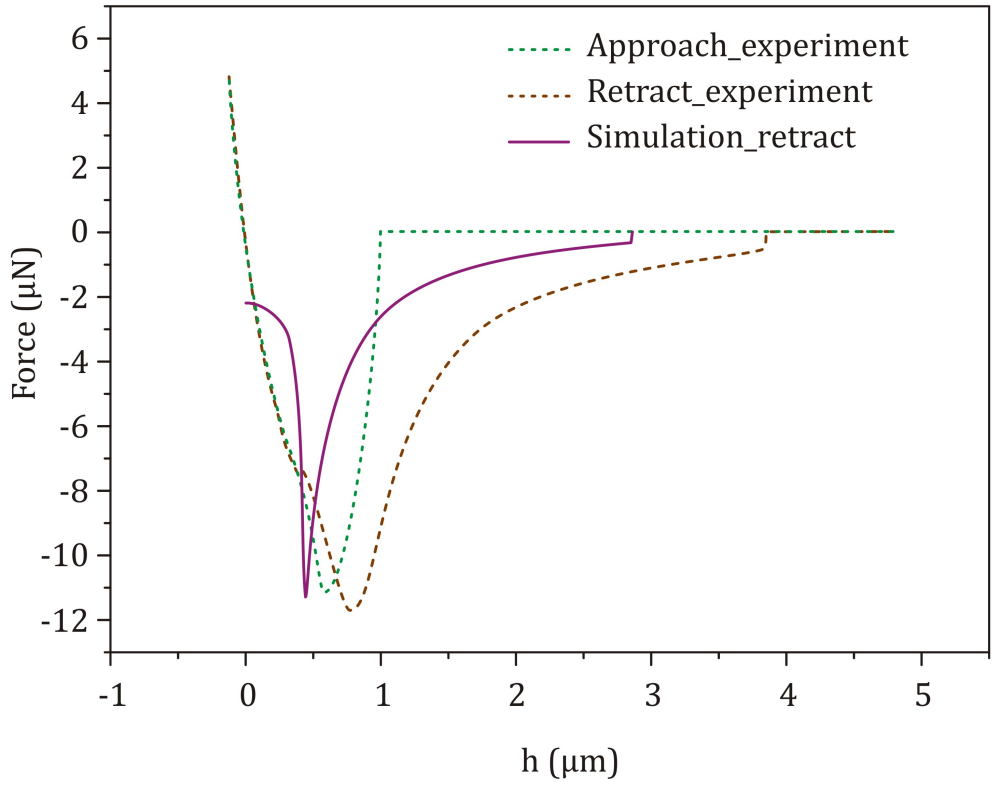

Figure 5.18: Direct comparison between experimental result (dash line) and simulation (solid) is shown. Measured volume is, $V = 60\,\mu m^3$ and volume used to simulate the curve is $V = 21\,\mu m^3$.

There is another discrepancy between the experimental and the simulation curve evident from Figure 5.18. The simulated curve is shifted to left compared to the experimental curve. This is due to the fact that in the simulation, the softness of the PDMS is not taken into account, i.e. we assumed the pillars to be a rigid structure that does not change its shape. In reality, however, the capillary forces will be strong enough to deform the pillar significantly. For a simple estimate, we consider a pillar as a spring with a spring constant. The deformation of the pillar due to the force ΔZ can be calculated as the following:

$$\frac{F}{A} = \frac{\Delta Z}{h} \cdot E^* \tag{5.4}$$

In Equation 5.4, F is the pulling up force, A is the cross sectional area of the pillar, h = 5 µm is the height of the pillar, and $E^* = 3.2$ MPa is the Young's modulus of the pillar. The deformation of the pillar due to the pulling force according to the Equation 5.4 for the minimum force (maximum capillary force) is 0.48 µm. By taking into account

0.48 µm deformation of the pillar and shifting the x axis by this value, the discrepancy between theory and experimental result will be compensated.
In order to understand the contribution of surface tensional force and Laplace pressure force to the total measured force, we simulated these contributions separately. As shown in Figure 5.19, the Laplace pressure force is dominating and surface tensional force has minor contribution to the total force.

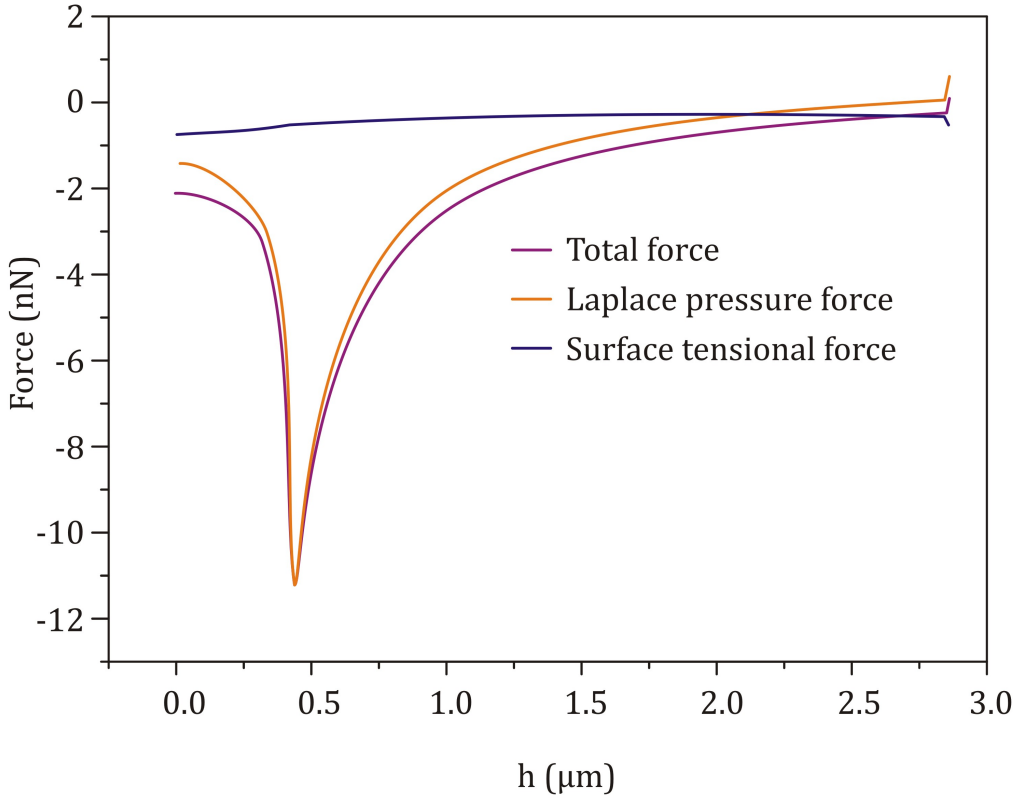

Figure 5.19: Contribution of surface tensional forces (dark blue) and Laplace pressure (orange) to the capillary force (violet).

5.4.1 Conclusion

As a conclusion, the experimental curves under wet condition show the strong contribution of capillary forces in adhesion. The observed forces can be fully understood by modeling of capillary forces. The numerical results approve that other contributions to the adhesion are not significant compared to capillary forces. In addition, numerical model did capture all details of the characteristic shape of the experimental force curves, as the kink and the rupture point. From the simulations it became obvious, that the kink occurred due to the pinning and depinning of the drop at the top edge of the pillar. Hence, measured adhesion forces can be explained theoretically just by capillary forces.

6 Friction Force on Biomimetic Structures

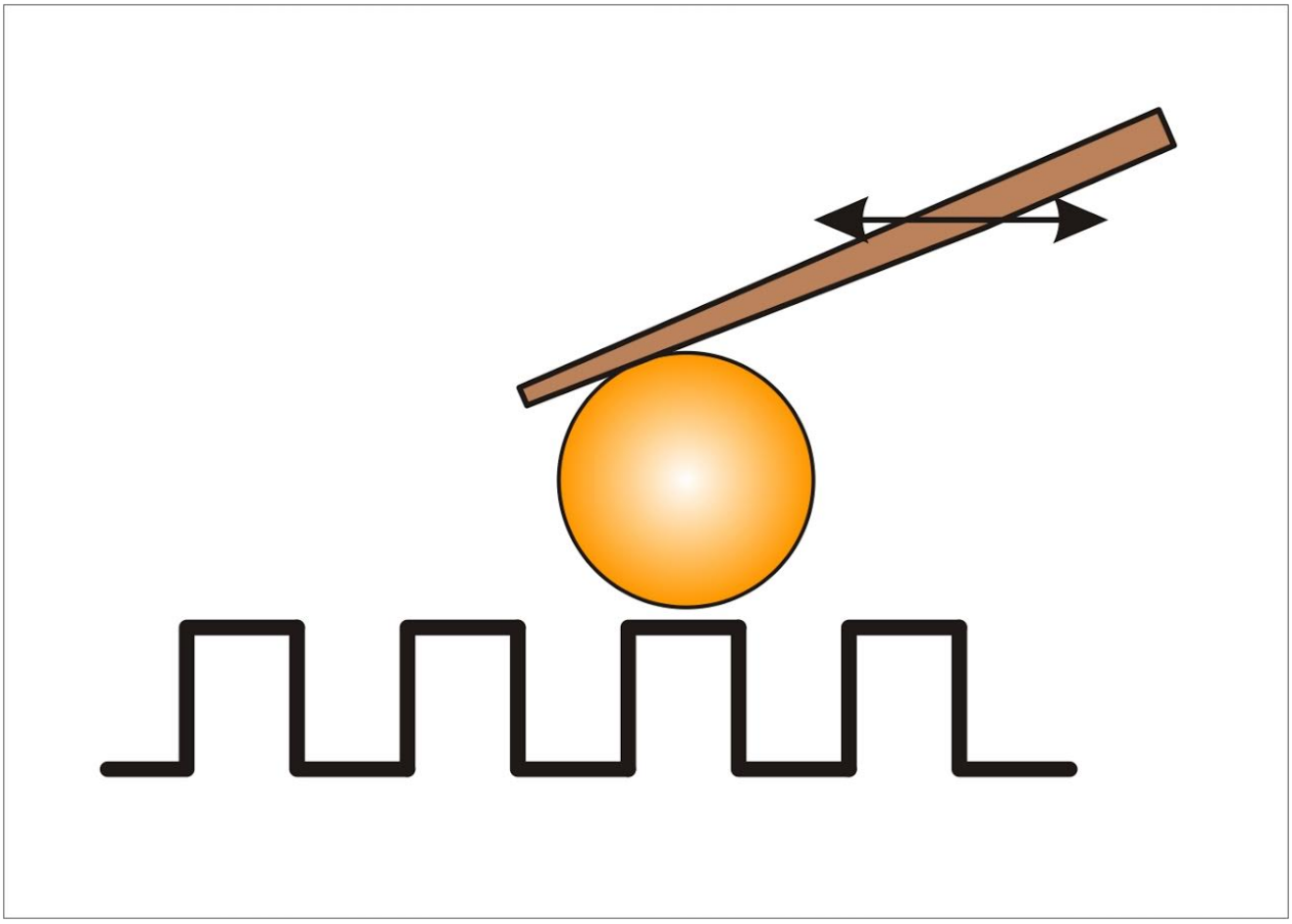

Since friction forces have major contributions in frogs's attachment and detachment [27, 48], in this chapter, friction forces between a spherical silica particle and soft and elastic micro-pillars, which are hexagonal, elongated pillars (see Chapter 3) have been studied using AFM (DI 3100).

6.1 Experimental Method

A 17 μm diameter colloidal probe was cleaned by plasma cleaning in Argon (properties of the plasma chamber discussed in Chapter 3) for ten minutes before each measurements. The vertical spring constant of the cantilever was 65 N/m, which has been measured by the thermal noise method. The probe scanned 50 μm of the surface with the scan rate of 0.5 Hz at different applied loads. The trace and retrace images of the scanned pillars have been recorded. Furthermore, the difference of the trace and the retrace signals at different loads were calculated using Gwyddion 2.36 software.

6.1.1 Results and Discussion

The friction on the soft, structured samples with elongated hexagonal micro-pillars (D15/20, d3, h5, aspect ratio 0.33) was studied. In the first series of measurements, the surface of the micro-pillars has been scanned parallel to the longer side of the pillars at different applied load using a colloidal probe. Since the friction force is proportional to the normal force, we are interested in understanding how friction forces change at different applied loads. Therefore, we have measured the voltage of the piezo while tracing and retracing the surfaces at 0.3, 2.3, 4.4 and, 6.8 μN applied load. The applied load is calculated by multiplying the deflection sensitivity and the spring constant of the cantilever to the set point.
The friction force can be calculated from the measured lateral deflection signal, lateral sensitivity, and torsional spring constant. In principle, calibration of the lateral deflection signal is possible. However, for such stiff cantilevers and large colloidal probes as we have used in our experiments the established methods fail either because the torsional resonance frequency is beyond the measurement range [156] in our AFM setup ($>$ 1 MHz) or because the sphere radius does not match the calibration gratings commercially available [157]. Hence, we used a relative approach to calculate friction force from the recorded lateral deflection signal. As the long axis of the cantilever is oriented perpendicular to the scan direction, the cantilever bends laterally depending on the scan direction. When the probe scans from left to right (trace), friction bends the probe to the right. When the probe scans from right to left (retrace), cantilever bends more to the left due to the friction. The schematic images of trace and retrace are shown in Figure 6.1 (a) and (b) respectively.

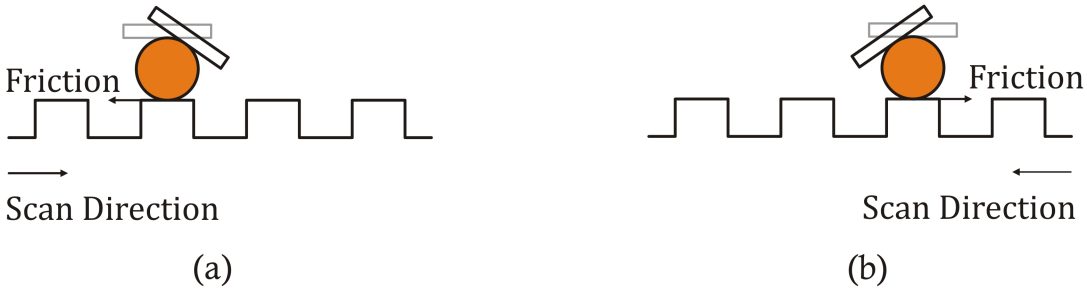

Figure 6.1: The schematic image of (a) trace: the colloidal probe scans from left to right. Large friction leads to stronger torsion of the cantilever to the right and therefore to a larger positive voltage signal. (b) Retrace: the colloidal probe scans from right to the left. Larger friction leads more bending to the left and therefore more negative voltage.

Cantilever bends differently as is shown in Figure 6.1 depending on the scan direction. To eliminate this direction dependence, difference of the trace and the retrace signals was calculated. Therefore, any possible zero offset of the lateral deflection signal is eliminated.
In Figure 6.2 the schematic image of $50 \times 50\,\mu m$ scanned area of elongated pillars from the top view is shown. The cartoons indicates that the pillars have been scanned parallel to the long side of the elongated hexagons.

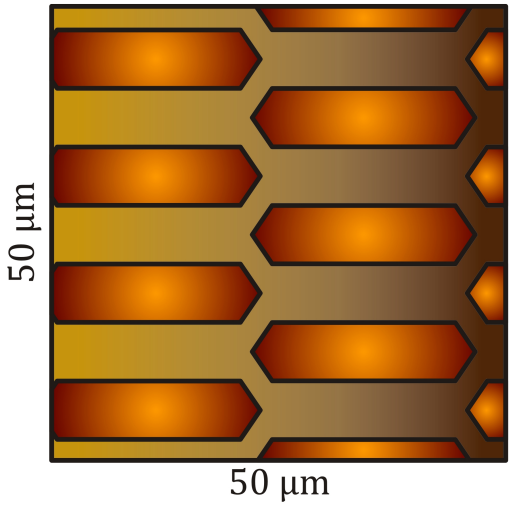

Figure 6.2: The schematic image of $50 \times 50\,\mu m$ scanned area with colloidal probe. The black solid lines are the edges of the pillars and the lighter brown areas are the surfaces of the pillars which are separated by narrow channels.

In order to understand the distribution of the friction forces on the elongated pillars, the surface has been scanned parallel to the larger axis of the pillars at the lowest

applied load, 0.3 μN. The trace and the retrace images of this measurement are shown in Figure 6.3 (a) and (b) respectively. In the trace image, when the colloidal probe scans the surface from left to right, there will be a large friction in the opposite direction, which leads to stronger torsion of the cantilever to the right and to the larger positive voltage signal. In the AFM images, areas of high friction are bright. In the retract image, colloidal probe scans from right to left. Furthermore, larger friction means more bending to the left and therefore more negative voltage. In the retract image, areas of high friction appear dark. The difference image of the trace and the retrace signals at applied force of 0.3 μN is shown below in Figure 6.3 (c).

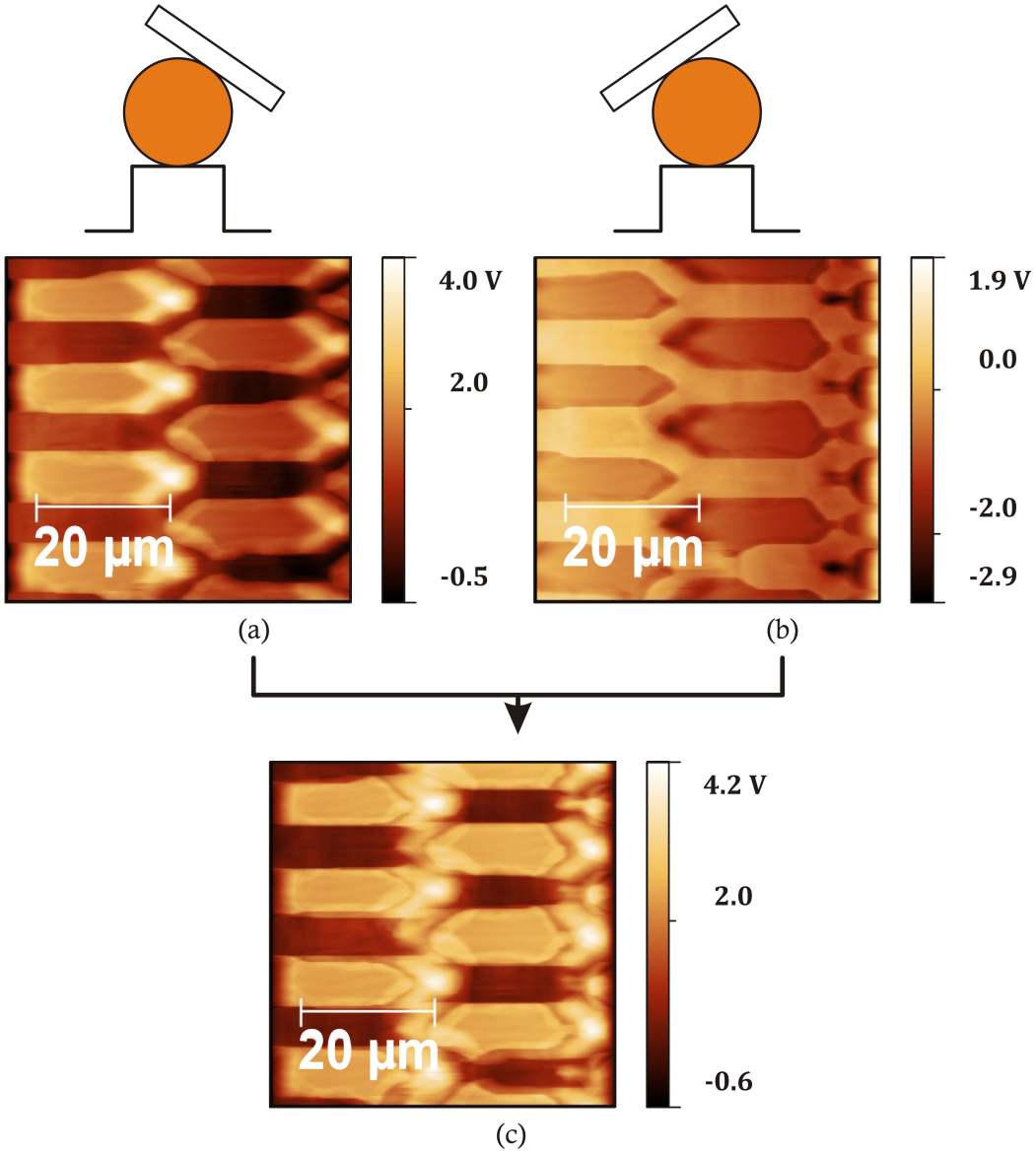

Figure 6.3: The colloidal probe scanning of elongated micro-pillars at applied load of 0.3 µN. (a) Trace and (b) retrace images of the scanning. The surface has been scanned parallel to the long side of the elongated hexagons. In part (c) the difference image of the trace and the retrace signals is shown. During the trace, which probe scans the surface from left to right, friction bends the probe to the right. While retracing, which the probe scans from right to left, due to the friction, cantilever bends to the left. In order to eliminate any possible zero offset of lateral deflection signal, the difference of the trace and the retrace signals is calculated.

Furthermore, the surface of the elongated pillars has been scanned at higher applied loads, 2.3, 4.4 and, 6.8 µN parallel to the larger side of the pillars, in order to investigate

the effect of an increase in the applied load on friction. As is shown in Figure 6.4, the deflection signal is increased by increasing the applied load.

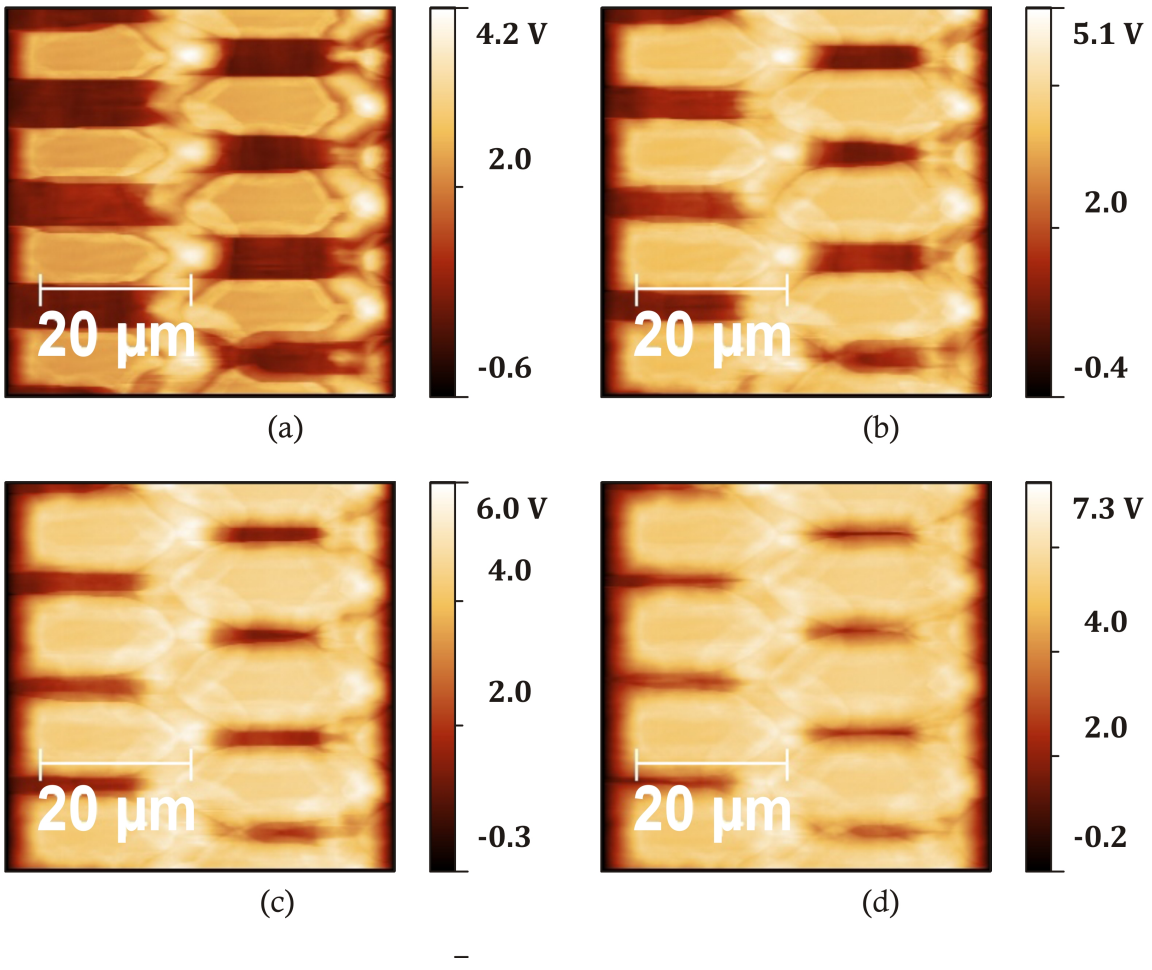

Figure 6.4: Image showing friction distribution that was calculated from the difference of trace and retrace signals at applied forces of (a) 0.3, (b) 2.3, (c) 4.4, and (d) 6.8 µN. The surface has been scanned parallel to the long side of the elongated hexagons. The deflection signal is increased by increasing the applied load.

In order to understand how the friction force changes by changing the scan direction, the surface of the pillars was scanned perpendicular to the larger side of the hexagons as well. The same colloidal probe was used to scan the surface perpendicularly as well as the same mounting of the probe as in the parallel scan direction (that means with the same lateral sensitivity and spring constant).
In Figure 6.5 the schematic image of 50×50 µm scanned area of elongated pillars from the top view is shown. The cartoons indicates that the pillars have been scanned perpendicular to the long side of the elongated hexagons.

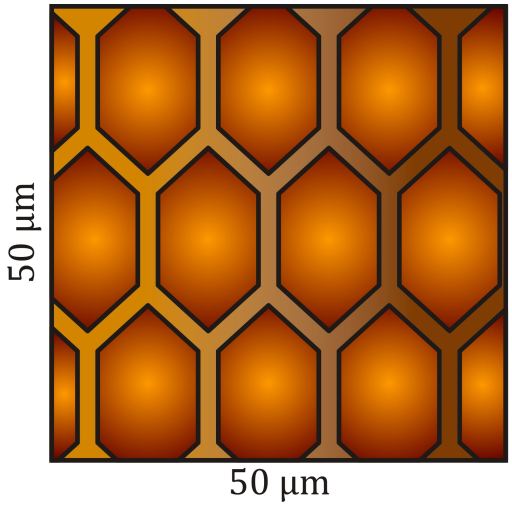

Figure 6.5: The schematic image of $50 \times 50\,\mu m$ scanned area with colloidal probe. The black solid lines are the edges of the pillars and the lighter brown areas are the surfaces of the pillars, which are separated by narrow channels.

The trace and the retrace images of the perpendicularly scanned micro-pillars were recorded at different applied loads. In Figure 6.6 one example of the trace and the retrace of perpendicularly scanned pillars are shown. the surface was scanned at applied load of, $0.3\,\mu N$, which is the lowest applied load.

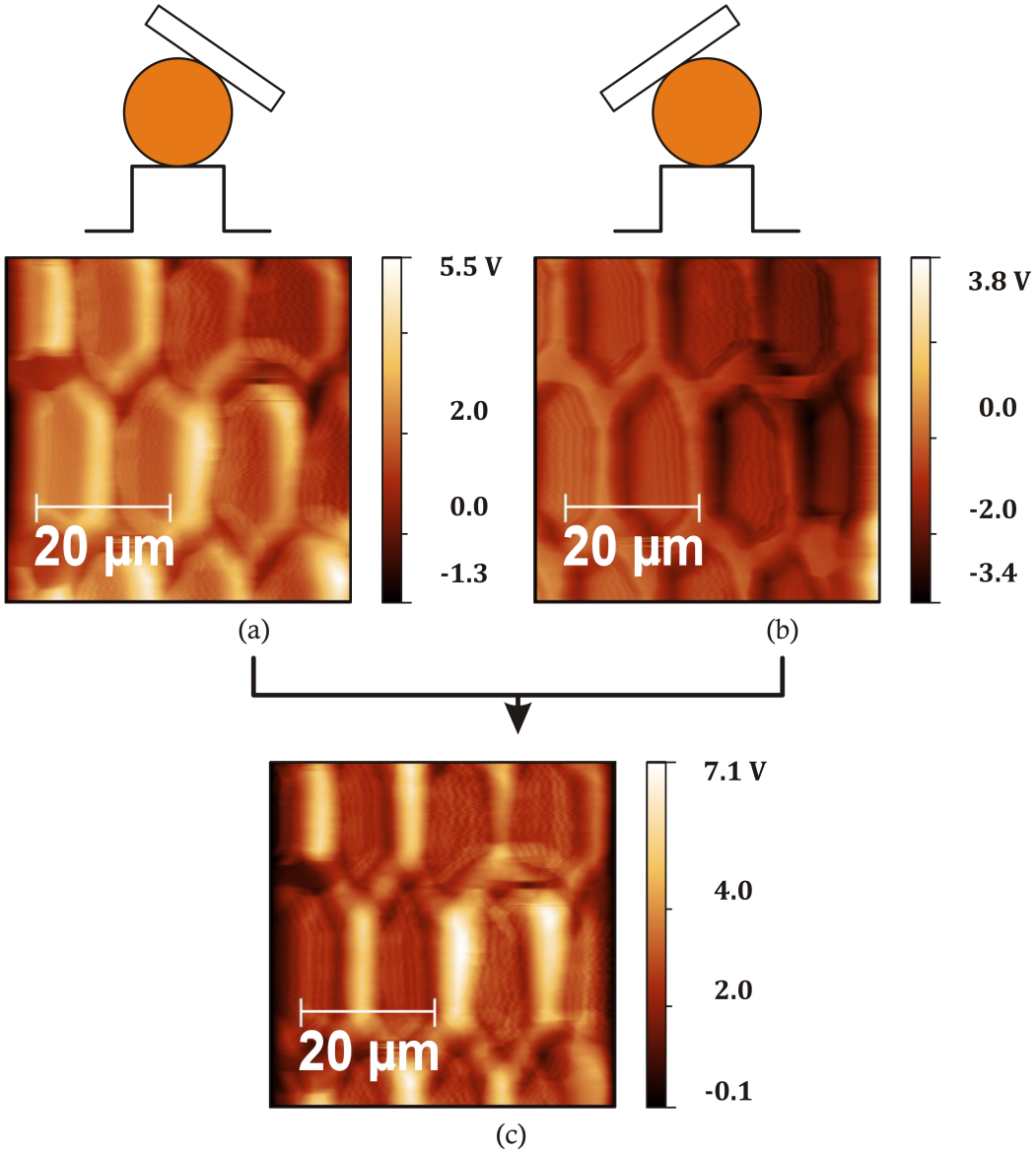

Figure 6.6: The colloidal probe scanning of elongated micro-pillars at applied load of 0.3 µN. (a) Trace and (b) retrace images of the scanning. The surface has been scanned perpendicular to the long side of the elongated hexagons. In part (c) the difference image of the trace and the retrace signals is shown. During the trace, which probe scans the surface from left to right, friction bends the probe to the right. While retracing, which the probe scans from right to left, due to the friction, cantilever bends to the left. In order to eliminate any possible zero offset of lateral deflection signal, the difference of the trace and the retrace signals is calculated.

The surface of the elongated pillars has been scanned at higher applied loads, 2.3, 4.4 and, 6.8 µN perpendicular to the larger side of the pillars, in order to investigate the

effect of an increase in the applied load on friction. As is shown in Figure 6.7, the deflection signal is increased by increasing the applied load.

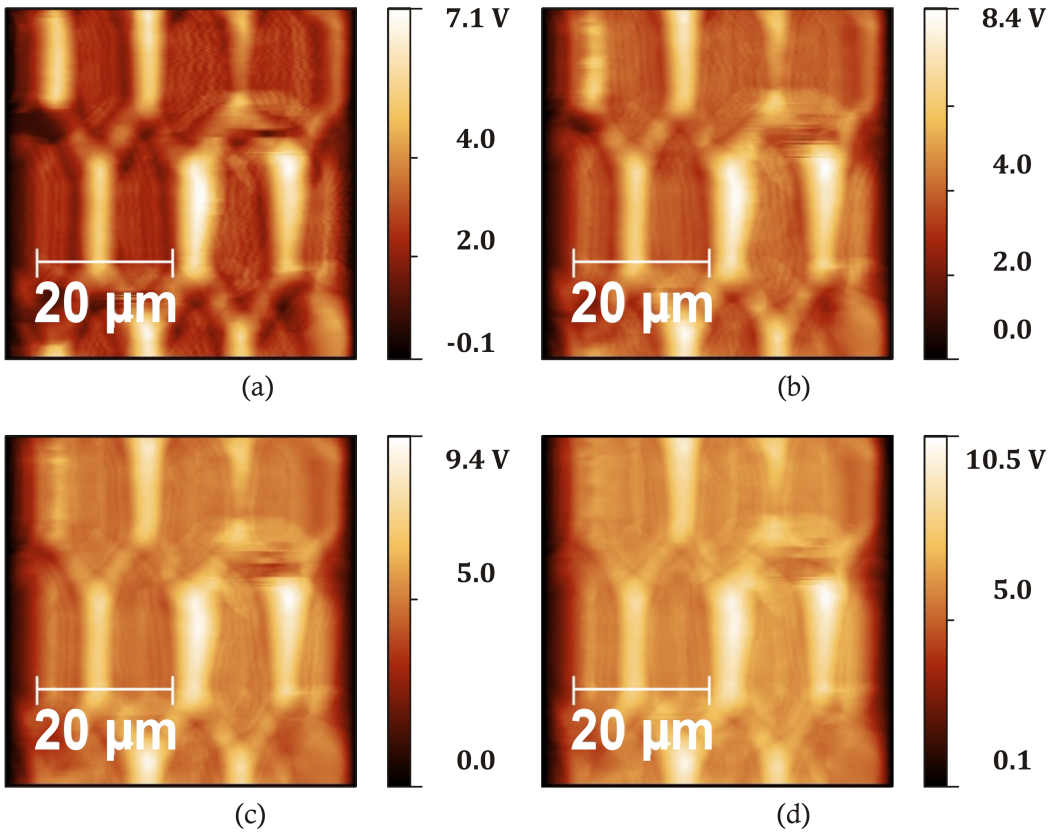

Figure 6.7: Image showing friction distribution that was calculated from the difference of trace and retrace signals at applied force of (a) 0.3, (b) 2.3, (c) 4.4, and (d) 6.8 µN. The surface has been scanned perpendicular to the long side of the elongated hexagons. The deflection signal is increased by increasing the applied load.

The deflection voltage is increased by increasing the applied load in the case of scanning perpendicularly to the longer side of the hexagons.
Now the relation between the applied load and the deflection voltage (proportional to the friction force) will be discussed. In Figure 6.8 the dependency of the deflection voltage to the applied load to the measurements in the parallel and the perpendicular directions, in respect to the longer side of the pillars are compared. The dependencies can be modelled by a linear fit in both cases, however with a larger offset of 2.89 V and smaller slope of 0.44 V/μN in the perpendicular direction compared to the parallel direction with the offset of 0.47 V and slope of 0.55 V/μN. These results can be interpreted in the following way. The friction force in the perpendicular direction in the absence of any normal load is larger than the force in the parallel direction. However, by increasing the normal load,

the rate of increase in the friction force (equivalent to the friction coefficient) in parallel direction is larger.

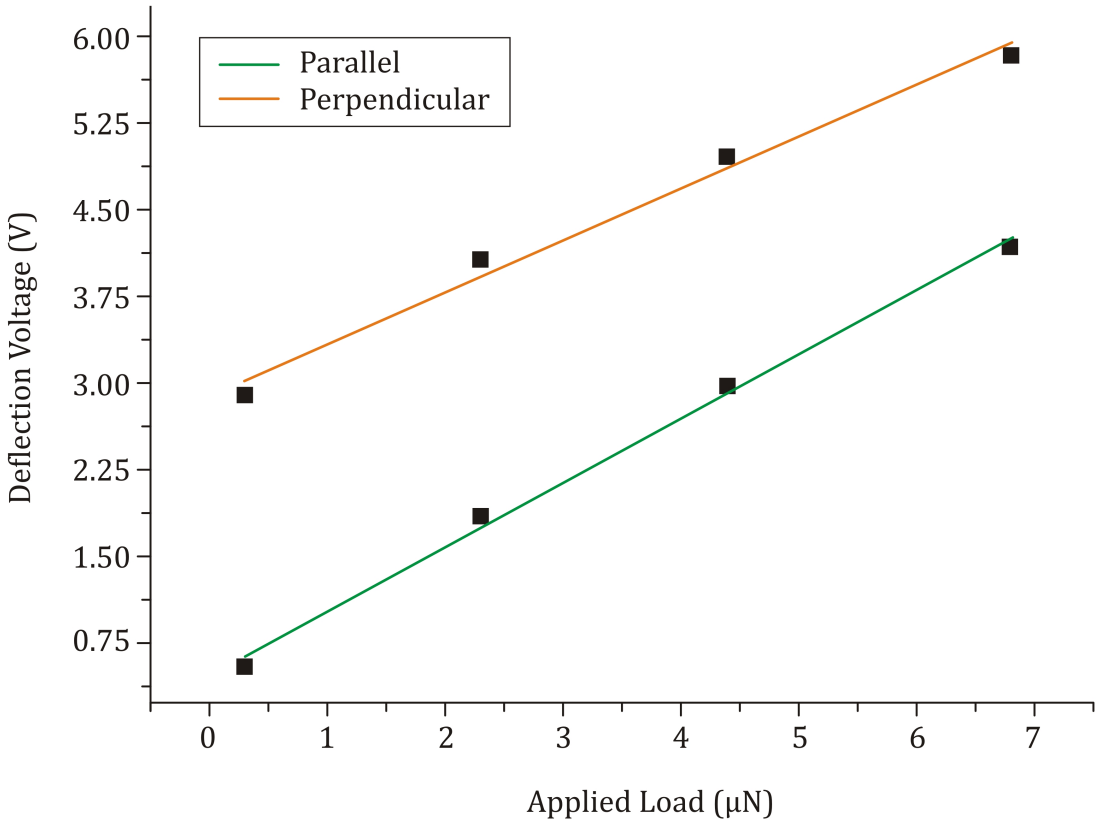

Figure 6.8: The dependency of the deflection voltage to the normal force for the measurements in the parallel and the perpendicular directions, in respect to the longer side of the pillars. The green line represents the linear fit for the measurements in the parallel scan direction. Equation $y = 0.55x + 0.47$ describes the fit. The orange line shows the linear fit to the measurements in perpendicular direction. Equation $y = 0.44x + 2.89$ describes the fit.

6.1.2 Conclusion

In the absence of any normal load, the friction force is larger than the force in the parallel direction. Moreover, the rate of increase in the friction force, by increasing the normal load, in parallel direction is larger. Finally we return to our motivation of biological attachment pads such as insects and tree frog's pads, which show a variety of structured contact surfaces. They seem to have taken advantage of these principles in attachment mechanism. So all that remains for us to better understand and mimic infinite nature variety.

7 Summary, Conclusion and Outlook

7.1 Summary and Conclusion

In this thesis, a better understanding of wet bioadhesion in tree frogs has been established. This was achieved by covering different aspects of wet bioadhesion. The surface forces such as hydrodynamic, capillary and frictional forces, which have contributions to the wet adhesion in tree frogs have been studied. Since the toe pad of the tree frogs are soft, we have studied the effect of the softness on the hydrodynamic force. The hydrodynamic drainage between a spherical silica particle and a soft, elastic polydimethylsiloxane (PDMS) surface was measured in ethanol using the colloidal probe technique at different particle speeds (Chapter 4). The finite element simulations and an analytical model were presented. Furthermore, the experimental force curves were compared to finite element simulations and the analytical model. The numerical finite element model was validated and approved to be consistent with experimental results over the range of $10 - 100\,\mu m/s$ speed between approaching / retracting sphere and planar surface.
As the experimental and simulation results have shown, the required force to separate a particle from a soft, elastic substrates in liquid is higher than that for a hard substrate. An elastic, soft surface has the effect of decreasing the hydrodynamic force compared to hard surface as a spherical particle approaches the surface.
The adhesion force on biomimetic hexagonal structure at the scale of single pillar was studied experimentally (Chapter 5). Measurements were performed on various single pillars on hydrophobic and hydrophilic surfaces under dry and wet condition by using colloidal probe technique. The role of different structures such as Normal shape, T-shape, and concave cup pillars were studied. The T-shape structure has shown the highest adhesion under dry condition. The over hanging parts in T-shape structure reduce the stress concentration at the edges over a larger area, therefore probe separation from the top of the T-shape structure pillars need more force compared to the Normal shape and concave cup pillars to induce crack formation and propagation that leads to detachment. The concave cup pillars have shown less adhesion due to less contact area between the probe and top of the pillar.

Under dry condition, the hydrophobic surfaces have shown slightly higher adhesion compared to the hydrophilic ones. However, from surface energy point of view, adhesion force should be higher on hydrophilic surface than on hydrophobic one. This discrepancy can be explained by the formation of a glassy layer of SiO_2 on top of the PDMS during plasma treatment.
Under wet condition, the experimental results have shown that capillary force is the dominating force. A smaller amount of liquid on the probe leads to the higher adhesion on the pillar. This is due to the increased meniscus curvature for smaller volumes, which leads to a higher Laplace pressure. The experimental results under wet condition were validated by simulation. The geometry of the meniscus, which is confined between the colloidal probe and the pillar was simulated by Surface Evolver (Version 2.7). The distance between probe and pillar, which changes the shape of the meniscus was simulated based on the experimental parameters such as diameter of the colloidal probe and the pillar, viscosity of the liquid, and volume of the liquid on the probe. Simulated adhesion force showed an agreement with experimental results. The main features of the experimental curve were captured in the simulated curve, such as the kink, due to depinning of the meniscus at the contact line of the pillar and the stretching part of the meniscus, the stretching of the meniscus before rupture and the position of the rupture point. However, there were two discrepancies between the maximum capillary force in the experiment and the simulation and position of the curves along the distance axes. This discrepancy in maximum capillary force might be induced by shifting part of the measured liquid volume to positions down the pillar. In this case not all the picked up liquid would contribute to the meniscus on the pillar. The shift in position might be due to elastic deformation of the pillars, which were assumed to be rigid in the simulations. The experimental and simulated curves fit each other when the plugged in liquid volume to the simulation was reduced, as well as by taking the elasticity of the surface into account.
The frictional behaviour of the biomemetic structure was studied using colloidal probe (Chapter 6). In order to understand this behaviour, the hexagonal and elongated pillars were scanned by the probe parallel and perpendicular to the longest side. AFM images of this friction measurements have demonstrated that the elongated pillars show high frictional force at edges. Furthermore, two scenarios describe the frictional behaviour: when no normal load is present, the friction force is larger when the pillars are scanned perpendicularly to the larger side of the hexagons compared to the parallel scanned pillars. By increasing the normal load, friction force increases with larger rate in the case of parallel direction compared to the perpendicular direction.

7.2 Outlook for Future

In this thesis (chapter 5), we have seen that the amount of liquid plays an important role in adhesion. Hence, investigating the role of intervening a liquid layer between toe pad of the frogs and the surface, as well as the drainage of the liquid on adhesion and frictional forces would help us to better understand the attachment and detachment in tree frogs. To achieve this goal, it could be possible to use a high resolution microscope such as a Digital holographic microscope (DHM) to detect the liquid layer and measure the forces simultaneously. At the end of this thesis, some preliminary work was done on studying the frictional behaviour of the biomimetic PDMS structures. The frictional forces could be measured on different structures such as Normal shape, T-shape and concave cup pillars with different sizes and aspect ratios. Further, it is possible to calculate the frictional force by knowing the lateral spring constant and lateral sensitivity of the cantilever [158].

References

[1] S. N. Gorb. The design of the fly adhesive pad: Distal tenent setae are adapted to the delivery of an adhesive secretion. *Proceedings of the Royal Society B-Biological Sciences*, 265(1398):747–752, 1998.

[2] W. J. P. Barnes. Functional morphology and design constraints of smooth adhesive pads. *MRS Bulletin*, 32:479, 2007.

[3] J. Berengueres, S. Saito, and K. Tadakuma. Structural properties of a scaled gecko foot-hair. *Bioinspiration & Biomimetics*, 2(1):1–8, 2007.

[4] R. Spolenak, S. Gorb, H. J. Gao, and E. Arzt. Effects of contact shape on the scaling of biological attachments. *Proceedings of the Royal Society A-Mathematical Physical and Engineering Sciences*, 461:305–319, 2005.

[5] John Tamelier, Sathya Chary, and Kimberly L. Turner. Vertical anisotropic microfibers for a gecko-inspired adhesive. *Langmuir*, 28(23):8746–8752, 2012.

[6] E. Arzt, S. Gorb, and R. Spolenak. From micro to nano contacts in biological attachment devices. *Proceedings of the National Academy of Sciences*, 100(19):10603–10606, 2003.

[7] B. Bhushan. Adhesion of multi-level hierarchical attachment systems in gecko feet. *Journal of Adhesion Science and Technology*, 21(12-13):1213–1258, 2007.

[8] G. Huber, H. Mantz, R. Spolenak, K. Mecke, K. Jacobs, S. N. Gorb, and E. Arzt. Evidence for capillarity contributions to gecko adhesion from single spatula nanomechanical measurements. *Proceedings of the National Academy of Sciences of the United States of America*, 102(45):16293–16296, 2005.

[9] K. Autumn, Y. A. Liang, S. T. Hsieh, W. Zesch, W. P. Chan, T. W. Kenny, R. Fearing, and R. J. Full. Adhesive force of a single gecko foot-hair. *Nature*, 405(6787):681–685, 2000.

[10] Kellar Autumn. Gecko adhesion: Structure, function, and applications. *MRS Bulletin*, 32:473–478, 2007.

[11] K. Autumn, M. Sitti, Y. A. Liang, A. M. Peattie, W. R. Hansen, S. Sponberg, T. W. Kenny, R. Fearing, J. N. Israelachvili, and R. J. Full. Evidence for van der waals adhesion in gecko setae. *Proceedings of the National Academy of Sciences*, 99(19):12252–12256, 2002.

[12] W. R. Hansen and K. Autumn. Evidence for self-cleaning in gecko setae. *Proceedings of the National Academy of Sciences of the United States of America*, 102(2):385–389, 2005.

[13] N. S. Pesika, Y. Tian, B. Zhao, K. Rosenberg, H. Zeng, P. McGuiggan, K. Autumn, and J. N. Israelachvili. Peel-zone model of tape peeling based on the gecko adhesive system. *The Journal of Adhesion*, 83(4):383–401, 2007.

[14] Y. Tian, N. Pesika, H. Zeng, K. Rosenberg, B. Zhao, P. McGuiggan, K. Autumn, and J. Israelachvili. Adhesion and friction in gecko toe attachment and detachment. *Proceedings of the National Academy of Sciences*, 103(51):19320–19325, 2006.

[15] A. Del Campo, C. Greiner, and E. Arzt. Contact shape controls adhesion of bioinspired fibrillar surfaces. *Langmuir*, 23(20):10235–10243, 2007.

[16] S. Reddy, E. Arzt, and .A. Del Campo. Bioinspired surfaces with switchable adhesion. *Advanced Materials*, 19(22):3833–3837, 2007.

[17] A. Carlson, A. M. Bowen, Y. G. Huang, R. G. Nuzzo, and J. A. Rogers. Transfer printing techniques for materials assembly and micro/nanodevice fabrication. *Advanced Materials*, 24(39):5284–5318, 2012.

[18] H. E. Jeong, M. K. Kwak, and K. Y. Suh. Stretchable, adhesion-tunable dry adhesive by surface wrinkling. *Langmuir*, 26(4):2223–2226, 2010.

[19] E. V. Gorb and S. N. Gorb. Attachment ability of the beetle chrysolina fastuosa on various plant surfaces. *Entomologia Experimentalis Et Applicata*, 105(1):13–28, 2002.

[20] T. Eisner and D. J. Aneshansley. Defense by foot adhesion in a beetle (Hemisphaerota Cyanea). *Proceedings of the National Academy of Sciences of the United States of America*, 97(12):6568–6573, 2000.

[21] J. H. Dirks and W. Federle. Fluid-based adhesion in insects: Principles and challenges. *Soft Matter*, 7(23):11047–11053, 2011.

[22] I. Scholz, W. J. P. Barnes, J. M. Smith, and W. Baumgartner. Ultrastructure and physical properties of an adhesive surface, the toe pad epithelium of the tree frog, litoria caerulea white. *J. Exp. Biol.*, 192:1193, 2009.

[23] V. Mizuhira. The digital pads of rhacophorid tree frogs. *Journal of Electron Microscopy*, 53(1):63–78, 2004.

[24] S. Chakraborti, D. Das, S. K. De, and T. C. Nag. Structural organization of the toe pads in the amphibian Philautus annandalii (Boulenger, 1906). *Acta Zoologica*, 95(1):63–72, 2014.

[25] W. J. P. Barnes, H. Peisker, S. N. Gorb, and S. N. Gorb. Comparative cryo-sem and afm studies of hylid and rhacophorid tree frog toe pads. *Journal of Morphology*, 274:1384–1396, 2013.

[26] W. J. P. Barnes, J. Pearman, and J. Platter. Application of peeling theory to tree frog adhesion, a biological system with biomimetic implications. *Eur Acad Sci E-Newslett Sci Technol*, 1(1):1–2, 2008.

[27] W. J. P. Barnes, C. Oines, and J. M. Smith. Whole animal measurements of shear and adhesive forces in adult tree frogs: Insights into underlying mechanisms of adhesion obtained from studying the effects of size and scale. *Journal of Comparative Physiology A*, 192:1179, 2006.

[28] W. J. P. Barnes. Biomimetic solutions to sticky problems. *Science*, 318, 2007.

[29] W. J. P. Barnes, J. Smith, C. Oines, and R. Mundl. Bionics and wet grip. *Tire Technology International*, 2002:56–60, 2002.

[30] V. V. Ernst. The digital pads of the tree frogs, Hyla-Cinerea.2. Mucous glands. *Tissue & Cell*, 5(1):97–104, 1973.

[31] W. J. P. Barnes, P. J. P. Goodwyn, M. Nokhbatolfoghahai, and S. N. Gorb. Elastic modulus of tree frog adhesive toe pads. *Comp. Physiol. A*, 197:969, 2011.

[32] D. M. Drotlef, E. Appel, H. Peisker, K. Dening, A. del Campo, S. N. Gorb, and W. J .P. Barnes. Morphological studies of the toe pads of the rock frogs, staurios parvus (family: Ranidae) and their relevance to the development of new biomimetically-inspired reversible adhesives. *In perpration*, 2014.

[33] W. Federle, W. J. P. Barnes, W. Baumgartner, P. Drechsler, and J. M. Smith. Wet but not slippery: Boundary friction in tree frog adhesive toe pads. *J. R. Soc. Interface*, 3:689, 2006.

[34] B. N. J. Persson. Wet adhesion with application to tree frog adhesive toe pads and tires. *Journal of Physics-Condensed Matter*, 19(37), 2007.

[35] A. Majumder, A. Sharma, and A. Ghatak. Bio-inspired adhesion and adhesives: Controlling adhesion by micro-nano structuring of soft surfaces. *Macromolecules*, 35(12):283–307, 2010.

[36] M. Varenberg and S. N. Gorb. Hexagonal surface micropattern for dry and wet friction. *Advanced Materials*, 21(4):483–486, 2009.

[37] S. B. Emerson and D. Diehl. Toe pad morphology and mechanism of sticking in frogs. *Biological Journal of the Linnean Society*, 13(3):199–216, 1980.

[38] G. Hanna and W. J. P. Barnes. Adhesion and detachment of the toe pads of tree frogs. *Journal of Experimental Biology*, 155:103–125, 1991.

[39] W. J. P. Barnes. Tree frogs and tire technology. *Tire Technology International*, pages 42–47, 1999.

[40] E. J. De Souza, M. Brinkmann, C. Mohrdieck, A. Crosby, and E. Arzt. Capillary forces between chemically different substrates. *Langmuir*, 24(18):10161–10168, 2008.

[41] H. J. Butt, W. J. P. Barnes, A. del Campo, M. Kappl, and F. Schonfeld. Capillary forces between soft, elastic spheres. *Soft Matter*, 6(23):5930–5936, 2010.

[42] M. Zakerin, M. Kappl, E. H. G. Backus, H. J. Butt, and F. Schonfeld. Capillary forces between rigid spheres and elastic supports: The role of Young's modulus and equilibrium vapor adsorption. *Soft Matter*, 9(17):4534–4543, 2013.

[43] B. N. J. Persson. Biological adhesion for locomotion: basic principles. *Journal of Adhesion Science and Technology*, 21(12-13):1145–1173, 2007.

[44] R. Gupta and J. Fréchette. Measurement and scaling of hydrodynamic interactions in the presence of draining channels. *Langmuir*, 28(41):14703–14712, 2012.

[45] J. M. Smith, W. J. P. Barnes, J. R. Downie, and G. D. Ruxton. Structural correlates of increased adhesive efficiency with adult size in the toe pads of hylid tree frogs. *Comp.Physiol. A*, 192:1193, 2006.

[46] X. J. Zhang, Y. Liu, Y. H. Liu, and S. I. U. Ahmed. Controllable and switchable capillary adhesion mechanism for bio-adhesive pads: Effect of micro patterns. *Chinese Science Bulletin*, 54(10):1648–1654, 2009.

[47] Saville D. A. Schowalter W. R. Russel, W. B. *Colloidal dispersion.* 1989.

[48] D. M. Drotlef, L. Stepien, M. Kappl, W. J. P. Barnes, H. J. Butt, and A. del Campo. Insights into the adhesive mechanisms of tree frogs using artificial mimics. *Advanced Functional Materials*, 23(9):1137–1146, 2013.

[49] A. Ohler. Digital pad morphology in torrent-living ranid frogs. *Asiatic Herpetological Research*, 6:85–96, 1995.

[50] P. Drechsler and W. Federle. Biomechanics of smooth adhesive pads in insects: Influence of tarsal secretion on attachment performance. *Comp Physiol A*, 192:1213–1222, 2006.

[51] https://student.societyforscience.org/article/ultrasonic-frogs-raise pitch.

[52] T. Endlein, W. J. P. Barnes, D. S. Samuel, N. A. Crawford, A. Biaw, and U. Grafe. Sticking under wet conditions: The remarkable attachment abilities of the torrent frog, staurois guttatus. *PlOS ONE*, 8(9):e73810, 2013.

[53] J. M. R. Bullock and W. Federle. Division of labour and sex differences between fibrillar, tarsal adhesive pads in beetles: effective elastic modulus and attachment performance. *The Journal of Experimental Biology*, 212:1876–1888, 2009.

[54] T. Endlein, A. Ji, D. Samuel, N. Yao, Z. Wang, W. J. P. Barnes, W. Federle, M. Kappl, and Z. Dai. Sticking like sticky tape: tree frogs use friction forces to enhance attachment on overhanging surfaces. *Journal of The Royal Society Interface*, 10(80):20120838, 2013.

[55] Haimin Yao and Huajian Gao. Mechanics of robust and releasable adhesion in biology: Bottom-up designed hierarchical structures of gecko. *Journal of the Mechanics and Physics of Solids*, 54(6):1120–1146, 2006.

[56] B. Zhao, N. Pesika, K. Rosenberg, Y. Tian, H. Zeng, P. McGuiggan, K. Autumn, and J. Israelachvili. Adhesion and friction force coupling of gecko setal arrays: implications for structured adhesive surfaces. *Langmuir*, 24(4):1517–1524, 2008.

[57] James MR Bullock, Patrick Drechsler, and Walter Federle. Comparison of smooth and hairy attachment pads in insects: friction, adhesion and mechanisms for direction-dependence. *The Journal of experimental biology*, 211(20):3333–3343, 2008.

[58] Walter Federle. Why are so many adhesive pads hairy? *Journal of Experimental Biology*, 209(14):2611–2621, 2006.

[59] Jan-Henning Dirks, MingHe Li, Alexandre Kabla, and Walter Federle. In-vivo dynamics of the internal fibrous structure in smooth adhesive pads of insects. *Acta biomaterialia*, 8(7):2730–2736, 2012.

[60] S. Gorb, Y. Jiao, and M. Scherge. Ultrastructural architecture and mechanical properties of attachment pads in tettigonia viridissima (Orthoptera tettigoniidae). *Journal of Comparative Physiology A*, 2000.

[61] S. Niederegger and S. Gorb. Tarsal movements in flies during leg attachment and detachment on a smooth substrate. *Journal of Insect Physiology*, 49(6):611–620, 2003.

[62] S. Gorb. Biological microtribology: anisotropy in frictional forces of orthopteran attachment pads reflects the ultrastructure of a highly deformable material. *Proceedings of the Royal Society of London. Series B: Biological Sciences*, 267(1449):1239–1244, 2000.

[63] W. Federle, E. L. Brainerd, T. A. McMahon, and B. Hölldobler. Biomechanics of the movable pretarsal adhesive organ in ants and bees. *Proceedings of the National Academy of Sciences*, 98(11):6215–6220, 2001.

[64] W. Federle and T. Endlein. Locomotion and adhesion: dynamic control of adhesive surface contact in ants. *Arthropod structure and development*, 33(1):67–75, 2004.

[65] C. J. Clemente and W. Federle. Pushing versus pulling: division of labour between tarsal attachment pads in cockroaches. *Proceedings of the Royal Society B: Biological Sciences*, 275(1640):1329–1336, 2008.

[66] K. Autumn, A. Dittmore, D. Santos, M. Spenko, and M. Cutkosky. Frictional adhesion: a new angle on gecko attachment. *Journal of Experimental Biology*, 209(18):3569–3579, 2006.

[67] H-J. Butt and M. Kappl. *Surface and interfacial forces*. Wiley-VCH, Weinheim, January 2010.

[68] H. J. Butt, K. Graf, and M. Kappl. *Physics and chemistry of interfaces*. Wiley-VCH, 2 edition, March 2006.

[69] J. Mahanty and B. W. Ninham. *Physics and chemistry of interfaces*. Academic Press: New York, January 1976.

[70] H. C. Hamaker. The london-van der Waals attraction between spherical particles. *Physica*, 4:1058–1072, 1937. Hamaker, HC.

[71] E. M. Lifshitz. The theory of molecular attractive forces between solids. *Soviet Physics Jetp-Ussr*, 2(1):73–83, 1956.

[72] I. E. Dzyaloshinskii, E. M. Lifshitz, and L. P. Pitaevskii. The general theory of van der Waals forces. *Advances in Physics*, 10(38):165–209, 1961.

[73] J. N. Israelachvili. Intermolecular and surface forces, 2011.

[74] M. Fuji, K. Machida, T. Takei, T. Watanabe, and M. Chikazawa. Effect of wettability on adhesion force between silica particles evaluated by atomic force microscopy measurement as a function of relative humidity. *Langmuir*, 15(13):4584–4589, 1999.

[75] T. Young. An essay on the cohesion of fluids. *Philosophical Transactions of the Royal Society of London*, 95:65–87, 1805.

[76] P.S. Laplace. Sur Íaction capillarie. *Dixieme Livre du Traite de Mecanique Celeste*, 1805-1806. Paris.

[77] V. L. Popov. Rigorous treatment of contact problems: Adhesive contact. *Book Chapter*, Contact Mechanics and Friction, 2010.

[78] H. Hertz. Über die berührung fester elastischer körper. *Journal für die reine und angewandte Mathematik*, 92:156, 1882.

[79] I. N. Sneddon. The relation between load and penetration in the axisymmetric boussinesq problem for a punch of arbitrary profile. *International Journal of Engineering Science*, 3:47–57, 1965.

[80] T. C. T. Ting. The contact stresses between a rigid indenter and a viscoelastic half-space. *Journal of Applied Mechanics*, 33(4):845–854, 1966.

[81] K. L. Johnson, K. Kendall, and A. D. Roberts. Surface energy and the contact of elastic solids. *Proceedings of the Royal Society of London Series A-Mathematical and Physical Sciences*, 324(1558):301–&, 1971.

[82] B. V. Derjaguin, V. M. Muller, and Y. P. Toporov. Effect of contact deformations on the adhesion of particles. *Journal of Colloid and Interface Science*, 53:314–326, 1975.

[83] F. Brochard and P. G. Degennes. Shear-dependent slippage at a polymer-solid interface. *Langmuir*, 8(12):3033–3037, 1992.

[84] S. G. Hatzikiriakos and N. Kalogerakis. A dynamic slip velocity model for molten polymers based on a network kinetic-theory. *Rheologica Acta*, 33(1):38–47, 1994.

[85] D. A. Hill. Wall slip in polymer melts: A pseudo-chemical model. *Journal of Rheology*, 42(3):581–601, 1998.

[86] Y. M. Joshi, A. K. Lele, and R. A. Mashelkar. A unified wall slip model. *Journal of Non-Newtonian Fluid Mechanics*, 94(2-3):135–149, 2000.

[87] A. L. Yarin and M. D. Graham. A model for slip at polymer/solid interfaces. *Journal of Rheology (1978-present)*, 42(6):1491–1504, 1998.

[88] J. L. Barrat and L. Bocquet. Large slip effect at a nonwetting fluid-solid interface. *Physical Review Letters*, 82(23):4671–4674, 1999.

[89] S. A. Gupta, H. D. Cochran, and P. T. Cummings. Shear behavior of squalane and tetracosane under extreme confinement. II. confined film structure. *The Journal of Chemical Physics*, 107(23):10327–10334, 1997.

[90] P. A. Thompson and S. M. Troian. A general boundary condition for liquid flow at solid surfaces. *Nature*, 389(6649):360–362, 1997.

[91] M. Sun and C. Ebner. Molecular dynamics study of flow at a fluid-wall interface. *Physical Review Letters*, 69(24):3491–3494, 1992.

[92] John Van Alsten and Steve Granick. Shear rheology in a confined geometry: Polysiloxane melts. *Macromolecules*, 23(22):4856–4862, 1990.

[93] R. G. Horn and J. N. Israelachvili. Molecular organization and viscosity of a thin film of molten polymer between two surfaces as probed by force measurements. *Macromolecules*, 21(9):2836–2841, 1988.

[94] G. Luengo, F. J. Schmitt, R. Hill, and J. Israelachvili. Thin film rheology and tribology of confined polymer melts: Contrasts with bulk properties. *Macromolecules*, 30(8):2482–2494, 1997.

[95] V. M. Litvinov and A. A. Zhdanov. Molecular motions in filled polydimethylsiloxanes. *Polymer Science U.S.S.R.*, 29(5):1133–1140, 1987.

[96] Y. Inn and S. Q. Wang. Hydrodynamic slip: Polymer adsorption and desorption at melt/solid interfaces. *Physical Review Letters*, 76(3):467–470, 1996.

[97] K. B. Migler, H. Hervet, and L. Leger. Slip transition of a polymer melt under shear-stress. *Physical Review Letters*, 70(3):287–290, 1993.

[98] S. Q. Wang and P. A. Drda. Superfluid-like stick-slip transition in capillary flow of linear polyethylene melts. 1. general features. *Macromolecules*, 29(7):2627–2632, 1996.

[99] V. Mhetar and L. A. Archer. Slip in entangled polymer melts. 1. General features. *Macromolecules*, 31(24):8607–8616, 1998.

[100] R. G. Horn, O. I. Vinogradova, M. E. Mackay, and N. Phan-Thien. Hydrodynamic slippage inferred from thin film drainage measurements in a solution of nonadsorbing polymer. *The Journal of Chemical Physics*, 112(14):6424–6433, 2000.

[101] E. Bonaccurso, M. Kappl, and H. J. Butt. Hydrodynamic force measurements: Boundary slip of water on hydrophilic surfaces and electrokinetic effects. *Physical Review Letters*, 88(7):076103, 2002.

[102] E. Bonaccurso, H. J. Butt, and V. S. J. Craig. Surface roughness and hydrodynamic boundary slip of a newtonian fluid in a completely wetting system. *Physical Review Letters*, 90(14), 2003.

[103] V. S. J. Craig, C. Neto, and D. R. M. Williams. Shear-dependent boundary slip in an aqueous newtonian liquid. *Physical Review Letters*, 87(5):054504, 2001.

[104] M. M. Denn. Issues in viscoelastic fluid mechanics. *Annual Review of Fluid Mechanics*, 22(1):13–32, 1990.

[105] M. C. A. Esperidião. Chain-exchange dynamics at a polymer solid interface: Effects of polydispersity and shear stress on linear low-density polyethylene flow. *Industrial & Engineering Chemistry Research*, 42(23):5819–5826, 2003.

[106] L. Hartmann, F. Kremer, P. Pouret, and L. Léger. Molecular dynamics in grafted layers of polydimethylsiloxane. *The Journal of Chemical Physics*, 118(13):6052–6058, 2003.

[107] Liliane Léger. Friction mechanisms and interfacial slip at fluid–solid interfaces. *Journal of Physics: Condensed Matter*, 15(1):S19, 2003.

[108] L. Léger, H. Hervet, Y. Marciano, M. Deruelle, and G. Massey. Role of surface-anchored polymer chains in adhesion and slippage. *Israel Journal of Chemistry*, 35(1):65–74, 1995.

[109] R. Pit, H. Hervet, and L. Léger. Direct experimental evidence of slip in hexadecane: Solid interface. *Phys. Rev. Lett.*, 85:980–3, 2000.

[110] G. Sun, E. Bonaccurso, V. Franz, and H-J. Butt. Confined liquid: simultaneous observation of a molecularly layered structure and hydrodynamic slip. *The Journal of Chemical Physics*, 117(22):10311–10314, 2002.

[111] O. I. Vinogradova. Drainage of a thin liquid film confined between hydrophobic surfaces. *Langmuir*, 11(6):2213–2220, 1995.

[112] Y. Zhu and S. Granick. Rate-dependent slip of newtonian liquid at smooth surfaces. *Physical Review Letters*, 87(9):096105, 2001.

[113] Y. Zhu and S. Granick. Apparent slip of newtonian fluids past adsorbed polymer layers. *Macromolecules*, 35(12):4658–4663, 2002.

[114] H. Brenner. The slow motion of a sphere through a viscous fluid towards a plane surface. *Chemical Engineering Science*, 16(3-4):242–251, 1961.

[115] D. Y. C. Chan and R. G. Horn. The drainage of thin liquid films between solid surfaces. *Journal of Chemical Physics*, 83(10):5311–5324, 1985.

[116] Gerd Binnig and Heinrich Rohrer. Scanning tunneling microscopy. *IBM Journal of Research and Development*, 44(1-2):279–293, 2000.

[117] G. Binnig, C. F. Quate, and Ch. Gerber. Atomic force microscope. *Physical Review Letters*, 56(9):930, 1986.

[118] GS. Blackmail, L. Lin, and RR. Matheson. Micro-and Nano-Wear of Polymeric Materials. 2000.

[119] ML. Bloo, H. Haitjema, and W. Pril. Deformation and wear of pyramidal, silicon-nitride afm tips scanning micrometre-size features in contact mode. *Measurement*, 25(3):203–211, 1999.

[120] R. García and R. Perez. Dynamic atomic force microscopy methods. *Surface Science Reports*, 47(6):197–301, 2002.

[121] Y. Martin, C. C. Williams, and H. K. Wickramasinghe. Atomic force microscope–force mapping and profiling on a sub 100-å scale. *Journal of Applied Physics*, 61(10):4723–4729, 1987.

[122] W. A. Ducker, T. J. Senden, and R. M. Pashley. Direct measurement of colloidal forces using an atomic force microscope. *Nature*, 353(6341):239–241, 1991.

[123] W. A. Ducker, T. J. Senden, and R. M. Pashley. Measurement of forces in liquids using a force microscope. *Langmuir*, 8(7):1831–1836, 1992.

[124] H. J. Butt. Measuring electrostatic, van der waals, and hydration forces in electrolyte solutions with an atomic force microscope. *Biophysical Journal*, 60(6):1438–1444, 1991.

[125] M. Kappl and H-J. Butt. The colloidal probe technique and its application to adhesion force measurements. *Particle & Particle Systems Characterization*, 19(3):129–143, 2002.

[126] D. M. Schaefer, M. Carpenter, B. Gady, R. Reifenberger, L. P. Demejo, and D. S. Rimai. Surface roughness and its influence on particle adhesion using atomic force techniques. *Journal of Adhesion Science and Technology*, 9(8):1049–1062, 1995.

[127] J. L. Hutter and J. Bechhoefer. Calibration of atomic-force microscope tips. *Review of Scientific Instruments*, 64(7):1868–1873, 1993.

[128] J. L. Hutter. Comment on tilt of atomic force microscope cantilevers: effect on spring constant and adhesion measurements. *Langmuir*, 21(6):2630–2632, 2005.

[129] B. Ohler. Cantilever spring constant calibration using laser doppler vibrometry. *Review of Scientific Instruments*, 78(6):063701, 2007.

[130] M.J. Stefan. Versuche über die scheinbare ädhasion. *Annalen der Physik*, 230(2):316–318, 1875.

[131] A. M. Smith. The role of suction in the adhesion of limpets. *Journal of Experimental Biology*, 161:151–169, 1991.

[132] O. Reynolds. On the theory of lubrication and its application to mr. beauchamp tower's experiments, including an experimental determination of the viscosity of olive oil. *Physical Review Letters*, 87(9):096105, 2001.

[133] H. A. Lorentz. Abhandlungen über theoretische physik, 1907.

[134] F. Altrichter. Lustig, experimentalle untersuchung über den einflußdes gefäßbodens auf die fallbewegung von kugeln in zähen flüssigkeiten. *Physikalische Zeitschrift*, 38:786–794, 1937.

[135] R. G. Cox. The motion of suspended particles almost in contact. *International Journal of Multiphase Flow*, 1(2):343–371, 1974.

[136] J. Happel and H. Brenner. Low reynolds number hydrodynamics. page 553, 1983.

[137] R. G. Cox and H. Brenner. The slow motion of a sphere through a viscous fluid towards a plane surface. *Chemical Engineering Science*, 22(12):1753, 1967.

[138] V. D. Hoper and A. M. Grant. The influence of a horizontal wall on the motion of a falling oil drop. *Australian Journal of Chemistry*, 1(1):28–40, 1948.

[139] G.D.M. MacKay, M. Suzuki, and S.G. Mason. Approach of a solid sphere to a rigid plane interface. part 2. *Journal of Colloid Science*, 18(1):103–104, 1963.

[140] O. I. Vinogradova, H. J. Butt, G. E. Yakubov, and F. Feuillebois. Dynamic effects on force measurements. I. viscous drag on the atomic force microscope cantilever. *Review of Scientific Instruments*, 72(5):2330–2339, 2001.

[141] C. D. F. Honig and W. A. Ducker. No-slip hydrodynamic boundary condition for hydrophilic particles. *Physical Review Letters*, 98(2):028305, 2007.

[142] L. Zhu, P. Attard, and C. Neto. Reconciling slip measurements in symmetric and asymmetric systems. *Langmuir*, 28(20):7768–7774, 2012.

[143] R. F. Tabor, F. Grieser, R. R. Dagastine, and D. Y. C. Chan. Measurement and analysis of forces in bubble and droplet systems using afm. *Journal of Colloid and Interface Science*, 371(1):1–14, 2012.

[144] D. Y. C. Chan, E. Klaseboer, and R. Manica. Film drainage and coalescence between deformable drops and bubbles. *Soft Matter*, 7(6):2235–2264, 2011.

[145] R. R. Dagastine, R. Manica, S. L. Carnie, D. Y. C. Chan, G. W. Stevens, and F. Grieser. Dynamic forces between two deformable oil droplets in water. *Science*, 313(5784):210–213, 2006.

[146] T. H. Fan and A. G. Fedorov. Analysis of hydrodynamic interactions during afm imaging of biological membranes. *Langmuir*, 19(4):1347–1356, 2003.

[147] S. Leroy and E. Charlaix. Hydrodynamic interactions for the measurement of thin film elastic properties. *Journal of Fluid Mechanics*, 674:389–407, 2011.

[148] A. Maali, Y. Pan, B. Bhushan, and E. Charlaix. Hydrodynamic drag-force measurement and slip length on microstructured surfaces. *Physical Review E*, 85(6), 2012.

[149] D. W. Pilat, P. Papadopoulos, D. Schäffel, D. Vollmer, R. Berger, and H. J. Butt. Dynamic measurement of the force required to move a liquid drop on a solid surface. *Langmuir*, 28(49):16812–16820, 2012.

[150] R. Stark, E. Bonaccurso, M. Kappl, and H. J. Butt. Quasi-static and hydrodynamic interaction between solid surfaces in polyisoprene studied by atomic force microscopy. *Polymer*, 47(20):7259–7270, 2006.

[151] L. Léger and C. Creton. Adhesion mechanisms at soft polymer interfaces. *Philos. T. R. Soc. A*, 366:1425, 2008.

[152] M. Deruelle, L. Leger, and M. Tirrell. Adhesion at the solid-elastomer interface: Influence of the interfacial chains. *Macromolecules*, 28(22):7419–7428, 1995.

[153] E. Frétigny and C. Barthel. Adhesive contact of elastomers: Effective adhesion energy and creep function. *Journal of Physics D: Applied Physics*, 42(19), 2009.

[154] J. A. Greenwood and K. L. Johnson. The mechanics of adhesion of viscoelastic solids. *Philosophical Magazine A*, 43(3):697–711, 1981.

[155] N. A. Lange and J. A. Dean. Lange's handbook of chemistry. *Polymer Science U.S.S.R.*, (5):1133–1140, 1973.

[156] C. P. Green, H. Lioe, J. P. Cleveland, R. Proksch, P. Mulvaney, and J. E. Sader. Normal and torsional spring constants of atomic force microscope cantilevers. *Review of scientific instruments*, 75(6):1988–1996, 2004.

[157] X. Ling, H. J. Butt, and M. Kappl. Quantitative measurement of friction between single microspheres by friction force microscopy. *Langmuir*, 23(16):8392–8399, 2007.

[158] S. Ecke, R. Raiteri, E. Bonaccurso, C. Reiner, H. J. Deiseroth, and H. J. Butt. Measuring normal and friction forces acting on individual fine particles. *Review of Scientific Instruments*, 72(11):4164–4170, 2001.

Glossary

AFM	atomic force microscope/microscopy
ca	circa
DHM	Digital Hologram Microscope
DMT	Derjaguin, Muller and Toporov
e.g.	exempli gratia, for example
etc.	et cetera
FEA	finite element analysis
FIB	focused ion beam
i.e.	id est, that is
JKR	Johnson, Kendall and Roberts
PDMS	Polydimethylsiloxane
rms	root mean square
SEM	scanning electron microscope/microscopy
SFA	surface forces apparatus
SPM	Scanning Probe Microscope
STM	Scanning Tunneling Microscope
vdW	Van der Waals
vs.	versus

List of Figures

Curriculum Vitae

[In der elektronischen Fassung aus Datenschutzgründen entfernt]